Distribution Agreement

In presenting this thesis or dissertation as a partial fulfillment of the requirements for an advanced degree from Emory University, I hereby grant to Emory University and its agents the non-exclusive license to archive, make accessible, and display my thesis or dissertation in whole or in part in all forms of media, now or hereafter known, including display on the world wide web. I understand that I may select some access restrictions as part of the online submission of this thesis or dissertation. I retain all ownership rights to the copyright of the thesis or dissertation. I also retain the right to use in future works (such as articles or books) all or part of this thesis or dissertation.

_____ _____

Joshua H. Bartlett Date

Electronic and Photoionization Spectroscopy of Heavy Metal-Containing Diatomic Molecules

By

Joshua H. Bartlett
Doctor of Philosophy

Department of Chemistry

_____
Michael C. Heaven
Advisor

_____
James T. Kindt
Committee Member

_____
Susanna Widicus Weaver
Committee Member

Accepted:

_____
Lisa A. Tedesco, Ph.D.
Dean of the James T. Laney School of Graduate Studies

_____
Date

Electronic and Photoionization Spectroscopy of Heavy Metal-Containing Diatomic Molecules

By

Joshua H. Bartlett
B.S., Youngstown State University, 2011

Advisor: Michael C. Heaven, Ph.D.

An abstract of
A dissertation submitted to the Faculty of the
James T. Laney School of Graduate Studies of Emory University
in partial fulfillment of the requirements for the degree of
Doctor of Philosophy
in Chemistry
2016

ABSTRACT

Electronic and Photoionization Spectroscopy of Heavy Metal-Containing Diatomic Molecules

By Joshua H. Bartlett

Gas phase molecules ThS, ThCl, SmO, BaO, and BaCl have been investigated using laser-induced fluorescence (LIF), dispersed fluorescence (DF), resonant multi-photon ionization (REMPI), two-color photoionization efficiency (PIE), and two-color pulsed field ionization zero kinetic energy photoelectron (PFI-ZEKE) spectroscopy. ThS and ThCl have been studied out of interest in the behavior of the actinide (Ac) – 3p compounds. In previous experiments, the Ac – 2p compounds ThN, ThO, and ThF have been studied. Extension of these studies to ThS and ThCl is an important foundational step for unraveling the structure of more complex actinide molecules. These molecules are also difficult to address with computational methods, and the spectroscopic data are used to evaluate performance of various levels of electronic structure theory. Ground state constants, excited state term energies, and excited state constants are found using the above techniques and reported for both the neutral molecule and its cation.

SmO^+ was predicted to form spontaneously in oxygen-rich environments when Sm vapor oxidizes, accompanied by electron emission. A high-altitude atmospheric release of Sm did not succeed in detecting an increase in electron density. The predictions were based on thermochemical data which were subsequently reevaluated. Photoionization experiments revealed that the ionization energy of SmO was underestimated by about 3%. The low electron density is partially explained by this result.

BaO and BaCl are molecular species that can be formed from ultracold atomic ions in magneto-optical traps. Ultracold molecules are a unique platform that can be useful for many unique experiments, such as measurement of fundamental physical constants, but manipulation of the ultracold molecules cannot proceed without measurement of the ion molecular constants and excited state term energies. Ionization energy, vibration frequency, and excited state term energies are investigated and reported for both molecules.

Electronic and Photoionization Spectroscopy of Heavy Metal-Containing Diatomic Molecules

By

Joshua H. Bartlett
B.S., Youngstown State University, 2011

Advisor: Michael C. Heaven, Ph.D.

A dissertation submitted to the Faculty of the
James T. Laney School of Graduate Studies of Emory University
in partial fulfillment of the requirements for the degree of
Doctor of Philosophy
in Chemistry
2016

ACKNOWLEDGMENTS

The following work would not exist if it not for the support of certain people. I would like to highlight, first and foremost, my advisor, Dr. Michael Heaven. He is possibly the most brilliant scientist I have ever met, and his patience, support, and instruction are the primary reasons I was able to make it to this point. All of the studies reported relied very heavily on his involvement and encouragement in times of need.

I also would like to recognize the other members of my committee, Dr. Susanna Widicus Weaver and Dr. James Kindt. Their thoughtful responses to my annual reports not only indicated to me their dedication, but also helped to develop my ability to write, present data, and answer questions in a way that would not have been possible otherwise.

All three of the above, and additionally Dr. Tim Lian, should also be thanked for their cumulative exams. These exams more than anything else were what taught me the skills of reading scientific papers. The effort that these four individuals put into creating and grading their cumulative exams became an essential part of my experience and deserves special recognition.

I was not the only one who worked on these experiments; Dr. Ivan Antonov preceded me, and began my process of learning to do the experiments, while Robert VanGundy will succeed me, and began my process of learning to teach. I am grateful for the hard work that both of them have done in their years at Emory University.

My apparatus did not exist by itself; the whole of the Heaven lab group members, past and present, also deserve to be mentioned. In addition, I would like to specifically acknowledge Michael Sullivan, Dr. Kyle Mascaritolo, Dr. Jacob Stewart, Dr. Adrian

Gardner, and Dr. Jiande Han for their feedback and assistance as needed.

I also want to recognize Steve Krebs, who on countless occasions put in orders for the various odds and ends needed by the experiment, and Ann Dasher, who graciously navigated the registration process for me every semester, as well as helped me get the forms I needed when I needed them.

There are many more people I met at Emory who have helped me – some in very noticeable ways, such as helping to repair equipment, and others in much smaller but no less important ways, such as a simple smile and greeting each day – and I must express my gratitude. If I were to name each person and how their interactions have helped me, I think that the acknowledgments might never end.

From my time at Youngstown State University, I would like to recognize Dr. Howard Mettee, whose physical chemistry courses were what first inspired me to veer in that direction. Dr. Peter Norris is also someone to whom I owe my gratitude, who first put the name, Emory, into my plans. His organic chemistry courses were delightfully engaging, and I am also thankful for his willingness to entertain my company during office hours. Dr. Ron Shaklee and Dr. Amy Cossentino were the directors of the University Scholars program during the years spent getting my undergraduate degree, and I would also like to recognize both of them for their devotion and support for all of the scholars.

Outside of academia, I would like to highlight all of the members of First Alliance Church of Atlanta, who have been a family like no other to me. Throughout the years, all of you were supportive of me in many different ways, and most importantly demonstrated the love of God to me.

To my parents, Randy and Susan Bartlett, I think it is fair to say that you have been supporting me the longest out of anyone. You were there to encourage me when things were tough, and to celebrate with me when things were going well. I love you both very much. And as for my brother, Sam, I am grateful, because you always motivated me to better myself. To my parents-in-law, Gary and Anabella Stalnaker, I want to recognize you for welcoming me into your family as if I were a true son. Thank you for having Stephanie.

To my lovely wife Stephanie, I do not think I could ever express enough how important you have been to me throughout the process of getting my degree. You have been continuously supportive and loving to me, even when things were difficult. I am so grateful to have you in my life, and thank you for always laughing at my jokes. I love you.

"So whether you eat or drink, or whatever you do, do it all for the glory of God."
– 1 Corinthians 10:31

Table of Contents

List of Tables

List of Figures

Figure 6.2. The highest energy occupied molecular orbitals for BaCl and $BaCl^+$. 153

Chapter 1

Introduction

Spectroscopy is a field dating back to 1646, with Athanasius Kirchner publishing his studies of the solar spectrum.[1] 370 years later, the advances over dispersing sunlight through a prism are staggering. Modern visible spectroscopy owes its success to two developments: the shortly-thereafter discovery of flame emission depending on with atomic and molecular components,[2] and the 1959 technique of light amplification by stimulated emission of radiation, better known as the laser.[3] Lasers have the characteristics of being collimated, monochromatic sources of light, which are desirable properties from the standpoint of experimental design. A collimated light source is easily manipulated with standard optical elements, and has the advantage over a diffuse light source of the ability to originate at some distance from the object of study. Monochromatic light is ideal for determining the energy of the photons involved in molecular excitation. Further developments of the laser allowed for tunable visible light to be produced by using laser light to illuminate a secondary medium which has a broadband response to the incident light, and then using additional manipulation to emit a single wavelength. The advent of the laser should be considered the beginning of modern

visible and ultraviolet spectroscopy. Yet even in the half-century lifespan of the field today, there exists no shortage of demand for spectroscopic studies.

The experiments described herein are gas phase spectroscopy studies on heavy metal-containing diatomic molecules. To begin with, it is best to explain the benefits such studies have to offer. Of the 4 phases of matter, being solid, liquid, gas, and plasma, gas phase spectroscopy provides spectral data that are the least complicated. Condensed phase molecules encounter solvation cages or lattice behavior that allows for relaxation of selection rules; as a result, the spectra recorded are much broader than the gas phase, and therefore offer less precise information. Spectroscopy of plasmas, on the other hand, is similar to gas phase spectroscopy in terms of the linewidths obtainable, but is limited by the complexity of the plasma, which contain a potentially large variety of radical and charged species and can therefore be difficult to interpret. In order to obtain the most precise data of excited state energies and molecular constants, it is preferable to study molecules in the gas phase.

Heavy metals, loosely categorized as atomic number $Z \geq 50$, are difficult to produce in the gas phase, as all except mercury exist in the solid phase. The heavy metals and their compounds are less amenable to study than their lighter counterparts, or even nonmetallic species, due to the melting points, the likelihood to form polyatomic species and clusters, and the toxicity of metal accumulation in soft tissues, which the human body has no mechanism to remove. There are many studies that have been performed using furnaces to vaporize metal compound samples and subsequently interrogate the gas with lasers, but this type of production is problematic. The molecules carry enough thermal

energy to populate a number of rotational, vibrational, and even electronic excited states, and the sheer density of lines obtained prove difficult to interpret. An alternative method of producing gas phase metal species was pioneered by Dietz *et al.*,[4] using a focused laser to ablate some amount of atoms from the surface of a metal target and entraining these in a supersonically-expanding jet. The jet expansion rotationally cools the molecules within, and so the only prerequisite is that the metal-containing molecule of interest can be produced within the jet. This is often accomplished by seeding the carrier gas (which is usually Ar or He) with a reactive chemical at low percentage. In this way, cold spectra that are much more readily interpretable can be obtained.

The laser spectroscopy techniques we employ, namely laser-induced fluorescence, fluorescence dispersion, resonant multi-photon ionization, and two-photon zero kinetic energy photoelectron spectroscopy, enable us to obtain an appreciable amount of molecular information. An explanation of these techniques is described in the following chapters. The precision of these techniques in our apparatus ranges from tens to tenths of wavenumbers, cm^{-1}. With laser-induced fluorescence, the molecule's ground state electronic configuration and rotation constant can be determined, as well as selected excited state term energies, electronic configurations, rotation and vibration constants. By fluorescence dispersion, ground state vibration constants and the lowest excited state term energies and vibration constants can be determined. Using the photoionization/photoelectron spectroscopy techniques, the ionization energy of the molecule, its ionic ground state electronic configuration, rotation and vibration constants, and excited state term energies as well as their rotation and vibration constants can be

determined. As diatomic molecules are the simplest type of molecule, however, it is not unusual that a candidate for study has already been examined in the past. In fact, the molecules that have been studied in the following chapters are all examples of molecules that have been studied in the gas phase at some point previously. For reasons specific to each molecule, however, the limitations of the previous experiments merited further study.

Chapters 2 and 3 discuss experiments on ThS and ThCl, respectively. The prior experimental studies were based on mass spectrometry techniques,[5,6] which were limited to reports of ionization and dissociation energies, and could say nothing about the excited states or molecular constants. In addition, the ionization energies reported were reported with uncertainties several orders of magnitude higher than those associated with the photoionization techniques performed on our apparatus. ThS and ThCl belong to the category of actinide compounds. Theoretical treatment of the actinides is difficult, and relies on having reliable experimental data for the molecular constants and excited state energies in order to evaluate the methods used in their calculations. Comparing theory and experiment was one of the motivations for studying these compounds.

Chapter 4 describes the work on SmO^+. The interest in this molecule comes from the chemi-ionization reaction of samarium oxidation,

$$Sm + O \rightarrow SmO^+ + e^- \qquad (1)$$

which, based on literature values, was expected to proceed almost entirely in the forward direction under normal atmospheric conditions. It was proposed that samarium vapor could be used to generate artificially enriched regions of electron density in the

atmosphere. The Air Force Research Laboratory performed tests involving the release of samarium at high altitude,[7] but did not observe any such increase in electron density as would be expected for reaction (1). This called into question the previous studies' results. To begin to explain the results of Ref. 7, the exothermicity of Sm + O was tested by a collaborating group, and the ionization energy of SmO was measured in our apparatus.

Chapters 5 and 6 describe our exploration of the ionization energy and excited states of BaO^+ and $BaCl^+$, respectively, which can be produced by simple reactions of alkaline earth ions. Alkaline earth ions are commonly used in ultracold matter experiments, where magneto-optical trapping (MOT) techniques confine the atomic ions to a well-ordered translationally-cold gas-phase lattice within a potential well of the MOT, achieving temperatures of μK. This is a developing field, but one of the advancements has been towards ultracold molecular ion production by flowing a reactive gas such as O_2 into the MOT, but without knowledge of the ions' excited state energies and molecular constants, complete quantum population control over the trapped molecules is not possible, which is a limitation to the field as a whole. Previous studies have characterized the ground and excited states of BaO and BaCl,[8,9] and the ionization energies[10,11] have been measured (but not to the precision that we can achieve), but no exploration of the ion excited states had been done before. The ion measurements performed in our apparatus enable greater flexibility in ultracold experimental design.

REFERENCES

(1) T. Burns, (1987). "Aspects of the development of colorimetric analysis and quantitative molecular spectroscopy in the ultraviolet-visible region". In C. Burgess and K. D. Mielenz, *Advances in Standards and Methodology in Spectrophotometry*.

(2) J. C. D. Brand, (1995). *Lines of Light: The Sources of Dispersive Spectroscopy, 1800 – 1930*.

(3) R. G. Gould, (1959). "The LASER, Light Amplification by Stimulated Emission of Radiation". In Franken, P.A.; Sands R.H. (Eds.). *The Ann Arbor Conference on Optical Pumping, the University of Michigan, 15 June through 18 June 1959*. p.128.

(4) T. G. Dietz, M. A. Duncan, D. E. Powers, and R. E. Smalley, *J. Chem. Phys.* **74**, 6511 (1981).

(5) C. C. L. Pereira, C. J. Marsden, J. Marcalo, J., and J. K. Gibson, *Phys. Chem. Chem. Phys.* **13,** 12940−12958 (2011).

(6) K. H. Lau and D. L. Hildenbrand, *J. Chem. Phys.* **92**, 6124-6130 (1990).

(7) K. M. Groves, R. G. Caton, T. R. Pederson, R. T. Paris, Y. Su, P. S. Cannon, N. K. Jackson-Booth, M. J. Angling, and J. M. Retterer, in American Geophysical Union, Fall Meeting, 2013.

(8) R. A. Gottscho, P. S. Weiss, R. W. Field, and J. G. Pruett, *J. Mol. Spectrosc.* **82,** 283 (1980).

(9) P. Pages, A. Pereira, P. Royen, *Phys. Scr.,* **31,** 281-285 (1985).

(10) J. M. Dyke, M. Feher, B. W. J. Gravenor, and A. Morris, *J. Phys. Chem.* **91,** 4476

(1987).

(11) L.A. Kaledin, M.C. Heaven, R.W. Field, *J. Mol. Spectrosc.,* **193,** 285-292 (1999).

Chapter 2

Spectroscopic and Theoretical Investigations of ThS and ThS^+

2.1. INTRODUCTION

Spectroscopic and theoretical studies of diatomic actinide sulfides (AnS) can provide insights concerning the bonding in materials that involve actinide−sulfur bonds. In addition to being a matter of fundamental interest, actinide−sulfur interactions are of importance for nuclear fuels and the design of chelating ligands used in separation processes.[1,2] Differences between the interactions of actinides with hard and soft donor ligands can be explored through comparisons of oxides and sulfides.

There have been relatively few studies of isolated AnS species. The most notable work is that of Pereira *et al*.,[3] who investigated the reactivities of a series of AnS and AnS^+ species in the gas phase using mass spectrometry. Ionization and bond dissociation energies were evaluated through studies of the reactions with COS, CO_2, CH_2O, and NO. As part of this effort, they carried out systematic theoretical studies of the AnS/AnS^+ and AnO/AnO^+ series using density functional theory (DFT) methods. This was done, in part,

to assess the accuracy of DFT methods when applied to actinides. Comparisons to the experimental results for AnO/AnO^+ suggested that DFT predictions were reasonably reliable but that the assessment of the sulfide predictions was limited due to the lack of data. In the present work, we have initiated gas phase spectroscopic studies of AnS species by examining the electronic excitation and photoionization of ThS. This choice is an extension of our recent spectroscopic studies of the related molecular pairs ThO/ThO^+ (refs 4−6), HfO/HfO^+ (refs 7 and 8), and HfS/HfS^+ (ref 9), permitting direct comparisons between the properties of these valence isoelectronic molecules and cations. There are no previous reports of gas phase spectroscopic data for ThS or ThS^+. However, the neutral molecule was observed in the matrix isolation study reported by Liang and Andrews.[10] They obtained a ground state vibrational frequency of 474.7 cm^{-1} for $Th^{32}S$ isolated in solid Ar at a temperature of 7 K. $^{32}S/^{34}S$ isotopic substitution and DFT calculations were used to confirm the species assignment. The latter predicted a $^1\Sigma^+$ ground state with a low-lying $^3\Delta$ state (as has been observed for ThO, HfO, and HfS).

Here, we report on the characterization of ThS using laser excitation and dispersed fluorescence spectroscopy. Two-color photoionization techniques have been used to obtain an accurate ionization energy (IE) and vibrationally resolved data for the first two electronic states of the ThS^+ cation. High-level ab initio calculations that include the effects of spin−orbit coupling have been carried out for comparison with the spectroscopic data.

2.2. EXPERIMENTAL METHODS

The apparatus used in this study has been described previously,[11−13] so only a brief description is given here. ThS was produced using a laser ablation source. The 1064 nm output of a pulsed Nd/YAG laser (~20 mJ, pulse duration 6 ns, Continuum Minilite II) was focused onto a Th metal disk that was continuously rotated and translated to expose a fresh surface for each laser shot. A pulsed solenoid valve, located behind the Th foil, produced a gas pulse that entrained the ablated material in a carrier gas consisting of He + 0.2% H_2S. The mixture was subjected to a supersonic expansion, thereby cooling the ablation products. The backing pressure and gas pulse duration were typically 2.7−3.1 bar and 300 μs.

Laser induced fluorescence (LIF) spectra were recorded with the excitation laser positioned approximately 5 cm downstream from the expansion nozzle orifice. The output from a Coherent ScanMate Pro dye laser/Nd:YAG laser system was propagated perpendicularly to the direction of the gas expansion. Baffle arms were installed on the windows of the source chamber to reduce the amount of scattered laser light. Fluorescence was collected along an axis that was perpendicular to both the laser beam and gas expansion axes. Low resolution spectra (0.15 cm^{-1} fwhm) were obtained using just the diffraction grating as the tunable element in the ScanMate Pro. Higher resolution spectra were recorded by using an intracavity etalon to reduce line width to approximately 0.06 cm^{-1} . Fluorescence was detected by a Photonis XP2020 photomultiplier tube. Dispersed florescence spectra were collected using a 0.25 m Ebert

monochromator (Jarrell-Ash model 82−410, 1180 line/mm grating, 0.5 mm slit width).

Downstream of the LIF detection region, the core of the jet expansion entered a second differentially pumped chamber via a conical skimmer with a 5 mm orifice. This chamber housed a time-of-flight mass-spectrometer (TOFMS) operating with a 250 V/cm field between the repeller and extractor plates. In the TOFMS, the molecular beam was crossed by two counter-propagating beams from tunable dye lasers (Continuum ND6000 and a Coherent ScanMate Pro). Two-color two-photon (1 + 1′) resonantly enhanced multiphoton ionization (REMPI) spectra were recorded by scanning the Coherent ScanMate Pro dye laser to search for resonant intermediate excited states, ionizing the excited molecules with the ND6000 dye laser and recording the resulting mass spectrum. The laser beams were temporally overlapped and synchronized with the pulsed molecular beam using digital delay generators.

Photoionization efficiency (PIE) spectra were recorded to determine the ionization energy of ThS using the same experimental arrangement as that for REMPI. The only difference being that the pump laser wavelength was fixed on a known transition of neutral ThS, and the ionization laser was scanned until the onset of the ThS^+ ion signal was observed in the mass spectrometer.

Pulsed field ionization−zero electron kinetic energy (PFI−ZEKE) spectra [11,14] were recorded for the ThS^+ molecular ion using two-color excitation. For these measurements, the repeller and the extractor electrodes were held at −3.5 V to give field free conditions during photoexcitation. After a 1.7 μs time delay, a voltage pulse was applied to the extractor electrode to give an electric field of 1.43 V/cm, causing ionization of the

remaining molecules in long-lived high-*n* Rydberg states, and accelerating the electrons toward the MCP detector located 10 cm below the repeller electrode. Transitions in the PFI−ZEKE spectra were confirmed to belong to ThS by detuning the pump laser from resonance with the intermediate state.

The LIF and REMPI spectra typically displayed a resolution of about 0.10−0.15 cm^{-1} , while rotationally resolved PFI−ZEKE spectra displayed a resolution of about 1.5 cm^{-1} . LIF and REMPI spectra were calibrated using the observed atomic Th lines.[15]

2.2.1. Notation

In the following, we use standard spectroscopic term symbols for the lower energy states of ThS and ThS^+ (i.e., those lying below 10000 cm^{-1}). The higher energy excited states of ThS are labeled using $\{v_0/10^3\}|\Omega|$ where v_0 is the band origin in wavenumbers and Ω is the projection of the electronic angular momentum along the diatomic axis.[16] The notation is modified to $[v_0/10^3]|\Omega|$ (the curly brackets are replaced by square brackets) when it is established that the $v = 0$ level for the state is being observed.

2.2.2. Electronic Structure Calculations

Calculations were carried out at the CASSCF/MRCI+Q level (complete active space self-consistent field multireference configuration interaction with the Davison size extensive correction) of theory as implemented in the MOLPRO 2010.2 suite of

programs.[17] Ground state potential energy curves for both ThS and ThS^+ were also examined using the RCCSD(T) method. Our calculations employed the aug-cc-pVTZ basis set of Woon *et al*.[18] for the sulfur atom, as taken from the MOLRPO 2010.2 basis set library. The basis set used for Th consisted of a 60-electron effective core potential with the atomic natural orbital basis for the valence electrons (ECP60MWB_ANO).[19,20] It included parameters for calculating the spin−orbit interaction energy and was optimized to recover scalar relativistic effects. The active space used for the calculations consisted of the S 3s and 3p orbitals with Th 7s, 7p, and 6d (13 orbitals with 10 (ThS) or 9 (ThS^+) electrons). The Th 6s and 6p orbitals were optimized, while being held fully occupied. To limit the size of the calculations the active space was restricted to configurations that had 7 or 8 electrons in the S 3s and 3p orbital subspace.

Spin−orbit coupling energies were determined using the Breit−Pauli operator evaluated in the basis of MCSCF wave functions (CASSCF/MRCI+Q/SO). Potential energy curves (PEC) were calculated up to about 10000 cm^{-1} above the minimum for each electronic state. To derive spectroscopic constants, the nuclear Schrödinger equation was solved variationally for each PEC of interest using the program LEVEL 8.0.[21] Predictions of the electronic states and excitation energies for ThS calculations that included the spin−orbit interaction are listed in Table 2.1. The ground state was found to be $X^1\Sigma^+$, as it is for the valence isoelectronic species ThO, HfO, and HfS. Molecular constants of ω_e = 477.2 cm^{-1}, $\omega_e x_e$ = 0.92 cm^{-1}, B_0 = 0.1074 cm^{-1}, and R_e = 2.363 Å were derived from the PEC. The permanent electric dipole moment at the equilibrium distance was predicted to be 4.1 D.

Examination of the wave function at the equilibrium distance indicated that this state has appreciable multireference character. The leading contributions were 56% $Th^{2+}(7s^2)S^{2-}(3s^23p^6)$ and 17% $Th^{+}(7s\sigma^26d\pi)S^{-}(3s^23p\sigma^23p\pi^3)$. CCSD(T) calculations yielded molecular constants (also listed in Table 2.1) that were in good agreement with the CASSCF/MRCI+Q/SO results, but the value of the T_1 diagnostic (0.025 near the equilibrium distance) clearly signaled that the multireference character was potentially problematic.

The lowest energy excited states of ThS are the $|\Omega| = 1$, 2, and 3 components of a $^3\Delta$ state. Calculations without spin−orbit coupling yield a multireference wave function for the $^3\Delta$ state, with a leading contribution of 74% $Th^{2+}(7s5d\delta)S^{2-}(3s^23p^6)$. The molecular constants derived from the spin−orbit coupled calculations show that promotion of an electron from 7s to the less polarizable 6d orbital causes a slight lengthening of the bond and decrease of the vibrational frequency. A single-point spin−orbit energy calculation, carried out with the inclusion of both singlet and triplet configurations, yielded a vertical excitation energy of 11504 cm^{-1} for the $Th^{2+}(7s5d\delta)S^{2-}(3s^23p^6)$ $^1\Delta_2$ state at the ground state equilibrium distance.

Theoretical predictions for ThS^+ are presented in Table 2.2. Following the behavior of the neutral molecule, the low-lying states arise from configurations that are predominantly $Th^{3+}(7s)S^{2-}(3s^23p^6)$ $X^2\Sigma^+$ and $Th^{3+}(6d)S^{2-}(3s^23p^6)$ ($^2\Delta$, $^2\Pi$, $^2\Sigma^+$). These states all show significant configurational mixing, but to a lesser degree than the corresponding states of the neutral molecule. For example, the leading contribution to the $X^2\Sigma^+$ eigenvector was 70% $Th^{3+}(7s)S^{2-}(3s^23p^6)$. Ground state molecular constants of $R_e = 2.318$

Å, ω_e = 508.0, and $\omega_e x_e$ = 0.99 cm^{-1} were obtained.

RCCSD(T) calculations for $ThS^+(X)$ yielded constants that were comparable to those obtained from the multireference calculations, but again the T_1 diagnostic was significant (0.026). Molecular constants for the $^2\Delta$ and $^2\Pi$ states exhibited the characteristic reduction in ω_e and increase in R_e (relative to the ground state) resulting from the lower polarizability of the 6d orbital (cf., Table 2.2).

Adiabatic ionization energies, obtained using CASSCF/MRCI+Q (53709 cm^{-1}), CCSD(T) (53928 cm^{-1}), and DFT/B3LYP (5.33×10^5 cm^{-1}) [3] methods were in good agreement. In Tables 2.1 and 2.2, we have also listed results from the density functional theory (DFT) calculations of Pereira *et al*. 3 and Liang and Andrews.[10] Pereira *et al*.[3] used the B3LYP and MPW1PW91 functionals in their investigation. There were differences between the results for the two functionals, but neither emerged as being systematically superior. In the following, we quote the results for the more commonly used B3LYP functional. Where comparisons could be made, the DFT results were in good agreement with the predictions of the present study. Note that the RCCSD(T) and DFT calculations for the ThS $^3\Delta$ state, which did not include spin−orbit coupling, are compared with the experimental and spin−orbit computed values for the $^3\Delta_2$ component. This choice was based on the expectation that the leading diagonal contribution from the spin−orbit operator will be given by $A\Lambda\Sigma$, where A is the spin−orbit coupling constant, Λ is the body-fixed projection of the electronic orbital angular momentum, and Σ is the projection of the spin. For this Hund′s case (a) approximation, Σ=0 for $^3\Delta_2$, making this component the least influenced by the spin−orbit interaction. This assumption was supported by the

CASSCF/MRCI+Q/SO calculations.

2.3. EXPERIMENTAL RESULTS

Low resolution survey spectra were recorded over the range 17500−24000 cm^{-1} using both LIF and (1 + 1′) REMPI detection. The LIF spectrum showed prominent features that were readily assigned to Th, ThO, and ThS. A section of this spectrum is shown in Figure 2.1. The bands of ThO and ThS could be distinguished on the basis of their characteristic band contours. Data taken using mass-resolved REMPI detection were used to confirm the attribution of specific LIF bands to ThS.

Nine vibronic features of ThS were found that were sufficiently free from overlapping transitions to be good candidates for studies of the rotational structures. The higher resolution spectra were recorded using the LIF detection, as this yielded narrower linewidths (mostly because robust fluorescence signals could be obtained using laser intensities that were low enough to avoid significant power broadening, while the higher intensity needed for REMPI caused some broadening). Figure 2.2 shows a typically example of the rotational structures observed.

This band has the characteristic features of a $^1\Pi-^1\Sigma$ transition, consistent with the theoretical prediction of a $X^1\Sigma^+$ ground state. The downward-going trace in Figure 2.2 shows a spectral simulation carried out using the program PGOPHER, 22 with the $\hat{N}^2$ representation of the Hamiltonian and the assumption of a rotational temperature of 28 K. The rotational structure was fitted by varying the band origin (ν_0), the upper and lower

state rotational constants (B' and B''), and the upper state lambda doubling parameter (q'). The line shape was represented by a Lorentzian function with a width (fwhm) of 0.06 cm^{-1}. Tests showed that the centrifugal distortion constants could not be determined with statistical significance, and they were subsequently set to zero. In fact, all of the bands that were rotationally resolved exhibited $^1\Pi-X^1\Sigma^+$ structures. The molecular constants obtained using PGOPHER fits to the rotational structures are listed in Table 2.3. Note that it is convenient for simulations to represent the upper electronic states as being $^1\Pi$, but it is likely that these states have mixed character. Hence, in the following, the higher excited states are labeled as being $|\Omega| = 1$.

Figure 2.3 shows a dispersed fluorescence spectrum that was recorded using excitation of the Q-branch band head of the $[22.12]1-X^1\Sigma^+$ transition. The structure on the low energy side of this spectrum is a short progression in the ground state vibration, while the two bands at higher energies may be ascribed to electronically excited states (see below). The ground state vibrational intervals defined an approximate value for the harmonic vibrational constant of $\omega_e = 479(1)$ cm^{-1}.

As a preliminary for PFI−ZEKE studies of the ion, two-color photoionization efficiency measurements were used to locate the ionization threshold. The advantage of this low-resolution survey technique is that it provides the fastest way to locate the lowest energy ionization feature. In this experiment, that first laser was set to excite the Q-branch band head of the $\{18.53\}1-X^1\Sigma^+$ transition. Figure 2.4 shows the photoionization efficiency curve recorded by scanning the wavelength of the second dye laser, with detection of the ThS^+ and Th^+ ion currents using the TOFMS. The atomic ion signal,

resulting from one-color two-photon ionization, provided wavelength calibration points. The trace for ThS^+ yielded a reasonably well-defined threshold energy. After correction for the effect of the electric field in the mass spectrometer (F) using the approximation $\Delta E(cm^{-1}) = 6(F(Vcm^{-1}))^{1/2}$, this measurement provided an ionization energy of 54415(20) cm^{-1}.

A PFI−ZEKE survey scan for ThS is shown in Figure 2.5. This trace was recorded with the first laser set to excite the Q-branch band head of the $\{23.59\}1-X^1\Sigma^+$ transition. Two vibrational progressions are evident in this trace, along with broad interference features centered near 56200 and 57500 cm^{-1} that were not part of the ThS^+ spectrum. The interfering features were still present when the first laser was tuned away from the ThS resonant excitation. Other than verifying that they did not originate from ThS^+, we did not attempt to identify the source of these signals. Higher resolution spectra, recorded with initial excitation of the $\{23.59\}1-X^1\Sigma^+$ band head, yielded unstructured vibronic features that were approximately 6 cm^{-1} wide (fwhm). The width was primarily determined by the simultaneous excitation of multiple rotational states. Attempts were made to improve the resolution by using the first laser to excite individual P-branch lines of the neutral molecule transition. However, the signal-to-noise ratio for these measurements was low, and we were unable to resolve the rotational states of the ThS^+ ion. The blue edge of the PFI−ZEKE origin band was used to obtain a refined value for the IE of 54425(3) cm^{-1}. Band edges from the two vibrational progressions are listed in Table 2.4.

Vibrational constants were determined by fitting the band edges to the standard

anharmonic oscillator expression,

$$T_v = T_e + \omega_e\left(v+\frac{1}{2}\right) - \omega_e x_e\left(v+\frac{1}{2}\right)^2 \quad (1)$$

This procedure yielded vibrational constants of ω_e =517(2) and $\omega_e x_e$ =1.2(3) cm^{-1} for the ground state and ω_e = 489(4) cm^{-1} for the excited state (the data did not yield a statistically significant value for $\omega_e x_e$).

2.4. DISCUSSION

The theoretical predictions for the ground state of ThS were found to be in reasonably good agreement with the spectroscopic data. The expected singlet multiplicity and $X^1\Sigma^+$ symmetry was confirmed. The measured rotational constant was larger than the calculated values, indicating that the equilibrium bond lengths were slightly overestimated. Because of the limited resolution of the dispersed fluorescence spectrum (Figure 2.3), the ground state vibrational constant of 479 cm^{-1} was determined with an error band of ±1 cm^{-1}. While the CASSCF/MRCI +Q/SO and CCSD(T) results were in good agreement with this value, DFT predictions were further outside of this error range. The gas phase measurement is also in good agreement with the ground state vibrational interval of $\Delta G_{1/2}$ = 474.7 cm^{-1} determined by matrix isolation spectroscopy,[10] considering the shift expected for the perturbing effect of the Ar host.

Note that the intensity pattern of the ground state progression in the dispersed fluorescence spectrum was consistent with emission from the zero-point vibrational level of the electronically excited state. The pattern indicates a slight shift between the upper

and lower state equilibrium distances. This is confirmed by the difference between the rotational constants, which show that the bond length is greater for the excited state. The dispersed fluorescence spectrum also shows transitions that terminate on two low-lying electronically excited states. Only the origin bands are detected for these transitions, indicating that the equilibrium bond lengths for the lower states are close to that of the emitting state. This pattern is consistent with the assignment of the lower states as $^3\Delta_1$ and $^3\Delta_2$. As can be seen in Table 2.1, these states are predicted to have a larger equilibrium distance, relative to that of the ground state. Note also that the emitting state was $|\Omega| = 1$. Hence, the $\Delta\Omega = 0, \pm1$ selection rule explains why a transition to the $^3\Delta_3$ component was not observed. Measured term energies for the $^3\Delta_1$ and $^3\Delta_2$ states were 3623(4) and 4534(4) cm^{-1}, respectively. The values predicted by the CASSCF/MRCI+Q/SO calculations (3940 and 4856 cm^{-1}) were in respectable agreement with both the absolute term energies and the spin−orbit interval. As noted previously, the first-order effects of spin−orbit coupling are minimal for the $^3\Delta_2$ component, and we found that a CCSD(T) calculation for the energy of this state without spin−orbit coupling was also close to the observed value.

For ThS^+, we have observed the ground state and the first electronically excited state at the level of vibrational resolution. The vibrational constants are consistent with the ground state being $Th^{3+}(7s)S^{2-}$ $X^2\Sigma^+$ and the excited state $Th^{3+}(6d\delta)S^{2-}$ $^2\Delta_{3/2}$. As has been noted previously in discussions of ThO^+ (ref 5), HfO^+ (ref 8), and HfS^+ (ref 9), the vibrational frequency is lowered by $(n-1)$d ← ns excitation because the less polarizable $(n-1)$d orbital is more strongly destabilized by the electrostatic interaction with the ligand.[16] The state ordering, term energy for $^2\Delta_{3/2}$ and the vibrational frequencies from the

calculations reported in Table 2.2 are in good agreement with the experimental data. As in the two-color PFI−ZEKE spectra recorded for ThO^+, HfO^+, and HfS^+, the long vibrational progressions observed for ThS^+ do no follow the Franck−Condon factors for the second excitation step.[5,8,9] This appears to be a common trait for di- and triatomic molecules that contain Th, U, or Hf (refs 5, 8, 9, and 23−27).

Overall, the findings of the present study are in good agreement with those of Pereira *et al*.[3] Our DFT and CCSD(T) calculations yielded comparable results, and the CASSCF/MRCI+Q/SO calculations show that the trends deduced from the spin-free calculations are not changed significantly by the inclusion of spin−orbit coupling. The ThS IE recommended by Pereira *et al*.[3] (6.7(2) eV) has an error range that encompasses our measured value of 6.7466(25) eV, and the IEs obtained from the calculations of the present study were also in respectable agreement with the experimental value (cf., Table 2.1). On the basis of both their calculations and comparisons of reactivities, Pereira *et al*.[3] concluded that the IE of ThS would be approximately 0.2 eV higher than that of ThO. This prediction was confirmed by the present measurement and our previous[5] IE for ThO of 6.60267(3) eV.

The energies of low-lying states of the valence isoelectronic molecules HfS/ThS/ThO and their cations are collected for comparison in Table 2.5. Here, it can be seen that the $^3\Delta_2$–$^3\Delta_1$ spin−orbit intervals of the neutral molecules are similar, falling in the range of 811−965 cm^{-1}. Similarly, the $^2\Delta_{5/2}$–$^2\Delta_{3/2}$ intervals of the ions fall in the range 2231−2881 cm^{-1}. When the effects of the second-order interactions between the $^1\Delta_2$, $^3\Pi_2$, and $^3\Delta_2$ states are taken into account for the neutrals,[28] the intervals for both the neutrals

and cations are consistent with the atomic ion (n−1)d spin−orbit coupling constants (the second and higher order interactions were calculated by MOLPRO via diagonalization of the matrix for the spin−orbit operator). In this respect, it seems that the low-lying states of these molecules can be rationalized using a ligand field model for the electronic structure. The fact that the $^3\Delta/^2\Delta$ states of ThS/ThS^+ are at a lower energy than the corresponding states of ThO/ThO^+ reflects the stronger destabilization of the 6d orbital by oxygen. This can be traced to the shorter bond length and greater charge separation of ThO/ThO^+.

Experimental and theoretical studies of ThX/ThX^+ and HfX/HfX^+ (X = O, S, F) diatomics show that the bond lengths contract and that the vibrational frequencies increase on ionization.[5,8,9,24,26] Paradoxically, the bond dissociation energies decrease slightly. The DFT calculations of Pereira *et al*.[3] indicate that this bevavior will be exhibited by all of the diatomic actinide sulfides. For nearly all of the Th and Hf species studied, the vibrational and rotational constants of the low-lying states provide clear indications of the electronic configuration of the metal atom. In Tables 2.1, 2.2, and 2.4, the change in the vibrational frequency that accompanies 6d ← 7s promotion is an example of this effect. However, there is one notable exception in this group of molecules. The lowest energy $^1\Sigma^+$ and $^3\Delta_1$ states of ThF^+ were found to have closely similar vibration constants, such that high-level theoretical calculations were unable to resolve the question of the energetic ordering of these states.[24] It is likely that interactions between multiple low-lying configurations are responsible for the deviation of ThF^+ from the simple molecular constant/electronic configuration mapping observed for the other

ThX and HfX species.

One of the motivations for the study of AnS/AnS^+ species by Pereira *et al*.[3] was the question of whether computationally inexpensive DFT models could be used to reliably predict the physical and chemical characteristics of An−S bonds. For ThX/ThX^+ (X = S, O) the experimental data validate the DFT results, and the higher level calculations preformed in the present study indicate that the Th atom relativistic pseudopotential of Cao *et al*.[19,20] yields reliable quantitative predictions in spin−orbit coupled calculations.

REFERENCES

(1) Dam, H. H.; Reinhoudt, D. N.; Verboom, W. Multicoordinate Ligands for Actinide/Lanthanide Separations. *Chem. Soc. Rev.* **36,** 367−377 (2007).

(2) Sato, N.; Kirishima, A. Sulfurization Behavior of Thorium Dioxide with Carbon Disulfide. *J. Nucl. Mater.* **414,** 324−327 (2011).

(3) Pereira, C. C. L.; Marsden, C. J.; Marcalo, J.; Gibson, J. K. Actinide Sulfides in the Gas Phase: Experimental and Theoretical Studies of the Thermochemistry of AnS (An = Ac, Th, Pa, U, Np, Pu, Am and Cm). *Phys. Chem. Chem. Phys.* **13,** 12940−12958 (2011).

(4) Wang, F.; Le, A.; Steimle, T. C.; Heaven, M. C. Communication: The Permanent Electric Dipole Moment of Thorium Monoxide, ThO. *J. Chem. Phys.* **134,** 031102/1−031102/3 (2011).

(5) Goncharov, V.; Heaven, M. C. Spectroscopy of the Ground and Low-Lying Excited States of ThO^+ . *J. Chem. Phys.* **124,** 064312/1−064312/7 (2006).

(6) Goncharov, V.; Han, J.; Kaledin, L. A.; Heaven, M. C. Ionization Energy Measurements and Electronic Spectra for ThO. *J. Chem. Phys.* **122,** 204311/1−204311/6 (2005).

(7) Stoll, H.; Peterson, K. A.; Merritt, J. M.; Heaven, M. C. On the Ionization Energy of HfO. *J. Phys. Chem. A* **113,** 12353−12355 (2009).

(8) Merritt, J. M.; Bondybey, V. E.; Heaven, M. C. Ionization Energy Measurements and Spectroscopy of HfO and HfO^+ . *J. Chem. Phys.* **130,** 144503/1−144503/9 (2009).

(9) Barker, B. J.; Antonov, I. O.; Heaven, M. C. Low-Lying States of HfS^+ and the Ionization Energy of HfS. *J. Mol. Spectrosc.* **275,** 35−40 (2012).

(10) Liang, B.; Andrews, L. Matrix Infrared Spectra and Quasirelativistic DFT Studies of ThS and ThS_2. *J. Phys. Chem. A* **106,** 4038−4041 (2002).

(11) Heaven, M. C. Probing Actinide Electronic Structure using Fluorescence and Multi-Photon Ionization Spectroscopy. *Phys. Chem. Chem. Phys.* **8,** 4497−4509 (2006).

(12) Merritt, J. M.; Kaledin, A. L.; Bondybey, V. E.; Heaven, M. C. The Ionization Energy of Be_2, and Spectroscopic Characterization of the $(1)^3\Sigma_u^+$, $(2)^3\Pi_g$ and $(3)^3\Pi_g$ States. *Phys. Chem. Chem. Phys.* **10,** 4006−4013 (2008).

(13) Merritt, J. M.; Bondybey, V. E.; Heaven, M. C. Experimental and Theoretical Study of the Electronic Spectrum of BeAl. *Phys. Chem. Chem. Phys.* **10,** 5403−5411 (2008).

(14) Muller-Dethlefs, K.; Schlag, E. W. High-Resolution Zero Kinetic Energy (ZEKE) Photoelectron Spectroscopy of Molecular Systems. *Annu. Rev. Phys. Chem.* **42,** 109−136 (1991).

(15) Palmer, B. A.; Engleman, R., Jr. *Atlas of the Thorium Spectrum*; Lawrence Livermore Natl. Lab.: Livermore, CA, 1983; p 335.

(16) Field, R. W. Diatomic Molecular Electronic Structure Beyond Simple Molecular Constants. *Ber. Bunsenges. Phys. Chem.* **86,** 771−779 (1982).

(17) Werner, H.-J.; Knowles, P. J.; Lindh, R.; Manby, F. R.; M. Schütz; et al. *MOLPRO, version 2010.2, a package of ab initio programs*; Cardiff University: Cardiff, U.K., 2010.

(18) Woon, D. E.; Dunning, T. H., Jr. Gaussian Basis Sets for Use in Correlated Molecular Calculations. III. The Atoms Aluminum Through Argon. *J. Chem. Phys.* **98,** 1358−1371 (1993).

(19) Cao, X.; Dolg, M. Segmented Contraction Scheme for Small-Core Actinide Pseudopotential Basis Sets. *THEOCHEM* **673,** 203−209 (2004).

(20) Cao, X.; Dolg, M.; Stoll, H. Valence Basis Sets for Relativistic Energy-Consistent Small-Core Actinide Pseudopotentials. *J. Chem. Phys.* **118,** 487−496 (2003).

(21) LeRoy, R. J. *LEVEL 8.0: A Computer Program for Solving the Radial Schrödinger Equation for Bound and Quasibound Levels*; University of Waterloo Chemical Physics: Waterloo, Canada, 2007;
Research Report CP-663; see http://leroy.uwaterloo.ca/programs/.

(22) Western, C. M.; *PGOPHER, A Program for Simulating Rotational Structure*; University of Bristol: Bristol, U.K., 2007.

(23) Antonov, I. O.; Heaven, M. C. Spectroscopic and Theoretical Investigations of UF and UF^+. *J.Phys. Chem. A* DOI: 10.1021/jp312362e (2013).

(24) Barker, B. J.; Antonov, I. O.; Heaven, M. C.; Peterson, K. A. Spectroscopic Investigations of ThF and ThF^+. *J. Chem. Phys.* **136,** 104305/1−104305/9 (2012).

(25) Merritt, J. M.; Han, J.; Heaven, M. C. Spectroscopy of the UO_2^+ Cation and the Delayed Ionization of UO_2. *J. Chem. Phys.* **128,** 084304/1−104304/8 (2008).

(26) Barker, B. J.; Antonov, I. O.; Bondybey, V. E.; Heaven, M. C. Communication: Spectroscopic Measurements for HfF^+ of Relevance to the Investigation of Fundamental Constants. *J. Chem. Phys.* **134,** 201102/1−201102/4 (2011).

(27) Goncharov, V.; Kaledin, L. A.; Heaven, M. C. Probing the Electronic Structure of UO^+ With High-Resolution Photoelectron Spectroscopy. *J. Chem. Phys.* **125,** 133202/1−133202/8 (2006).

(28) Launila, O.; Jonsson, J.; Edvinsson, G.; Taklif, A. G. Spectroscopy of HfS: Rotational Analysis of the $b^3\Pi-a^3\Delta$ Band System in the 1.7 mm Region. *J. Mol. Spectrosc.* **177,** 221−231 (1996).

(29) Edvinsson, G.; Lagerqvist, A. A Low-Lying $\Omega = 2$ State in the Thorium Monoxide (ThO) Molecule. *J. Mol. Spectrosc.* **113,** 93−104 (1985).

TABLE 2.1. Calculated Molecular Constants for ThS

State	T_e (cm^{-1})	ω_e (cm^{-1})	B_e (cm^{-1})	R_e (Å)	Method
$X^1\Sigma^+$	0	477	0.1074	2.363	*a*
	0	479	0.1079	2.358	*b*
	0	489	0.1089	2.347	*c*
	0	481	0.1087	2.349	*d*
$^3\Delta_1$	3940	454	0.1047	2.394	*a*
$^3\Delta_2$	4856	453	0.1048	2.393	*a*
	4923	457	0.1052	2.388	*b,e*
	3220	450	0.1050	2.390	*d*
$^3\Delta_3$	5811	455	0.1050	2.391	*a*

[a] CASSCF/MRCI/SO calculations. See text for details.

[b] CCSD(T)

[c] Density functional theory without spin-orbit coupling. B3LYP/ECP/pVTZ results from Ref. 3.

[d] Density functional theory without spin-orbit coupling.

[e] Obtained from a RCCSD(T) calculation for the lowest energy triplet state of a_2 symmetry (C_{2v})

TABLE 2.2. Calculated Molecular Constants for ThS^+

State	T_e^+ (cm^{-1})	ω_e^+ (cm^{-1})	B_e^+ (cm^{-1})	R_e^+ (Å)	Method
$X^2\Sigma^+$	0	502	0.1114	2.321	*a*
	0	508	0.1115	2.318	*b*
	0	514	0.1123	2.311	*c*
$^2\Delta_{3/2}$	2499	479	0.1084	2.353	*a*
$^2\Delta_{5/2}$	4730	487	0.1087	2.350	*a*
$^2\Pi_{1/2}$	8803	475	0.1063	2.375	*a*
$^2\Pi_{3/2}$	10313	472	0.1063	2.375	*a*

[a] CASSCF/MRCI/SO calculations. See text for details.

[b] RCCSD(T)

[c] Density functional theory without spin-orbit coupling. B3LYP/ECP/pVTZ results from Ref. 3.

TABLE 2.3. Molecular Constants Derived from the LIF Spectra for ThS

State[a]	Origin (cm^{-1})	B (cm^{-1})	q (cm^{-1})
$X^1\Sigma^+$	0.0	0.111(2)	0
{18.26}1	18259.0(3)	0.104(2)	0
{18.53}1	18529.4(3)	0.106(2)	$1.6(1)\times10^{-3}$
{18.69}1	18689.5(3)	0.104(2)	$1.9(2)\times10^{-3}$
{21.54}1	21542.0(3)	0.103(2)	$2.1(3)\times10^{-4}$
{21.94}1	21938.8(3)	0.103(2)	$8(3)\times10^{-4}$
{22.02}1	22024.8(3)	*b*	
[22.12]1	22117.5(3)	0.105(2)	$1.6(7)\times10^{-4}$
{23.15}1	23148.7(3)	*b*	
{23.59}1	23585.9(3)	0.105(2)	$8(4)\times10^{-4}$

[a] The values given in curly brackets are vibronic band origins, in units of 10^3 cm^{-1}. Values given in square brackets are for the electronic origin, in units of 10^3 cm^{-1}.

[b] Rotationally resolved spectra were not obtained due to problems with the etalon scanning system.

TABLE 2.4. Measured Vibronic Energies for ThS^{+} [a]

v	$X^2\Sigma^+$	$^2\Delta_{3/2}$
0	0	2136
1	523	2627
2	1030	3115
3	1537	3603
4	2048	
5	2554	
6	3059	
7	3556	

[a] Energies are in cm^{-1} with uncertainties of ± 3 cm^{-1}

TABLE 2.5. Comparison of Energies for the Low-Lying States of HfS/ThS/ThO and $HfS^+/ThS^+/ThO^+$

Molecule	$^3\Delta_1$	$^3\Delta_2$	ΔE_{SO}	Ref
HfS	6631.3	7596.6	965.3	28
ThS	3623(4)	4534(4)	911(6)	this work
ThO	5316.6	6127.9	811.3	29
	$^2\Delta_{3/2}$	$^2\Delta_{5/2}$		
HfS^+	5187(3)	7986(3)	2799	9
ThS^+	2136(3)	[4730][b]	[2231][b]	this work
ThO^+	2933.7	5814.4	2880.7	5

Except where indicated, energies are experimental T_0 values, in cm^{-1}.

[a] Ionization energies (cm^{-1}): IE_{ThS} = 54425(3); IE_{ThO} = 53253.8(2); IE_{Th} = 50868.71(8); IE_{HfS} = 61933(3); IE_{Hf} = 55047.9(3)

[b] CASSCF/MRCI/SO

FIGURE 2.1.

Section of a low-resolution LIF spectrum showing bands of ThS that are indicated by the vertical dotted lines. The bands marked with asterisks are from ThO, while the remaining features are Th atomic lines.

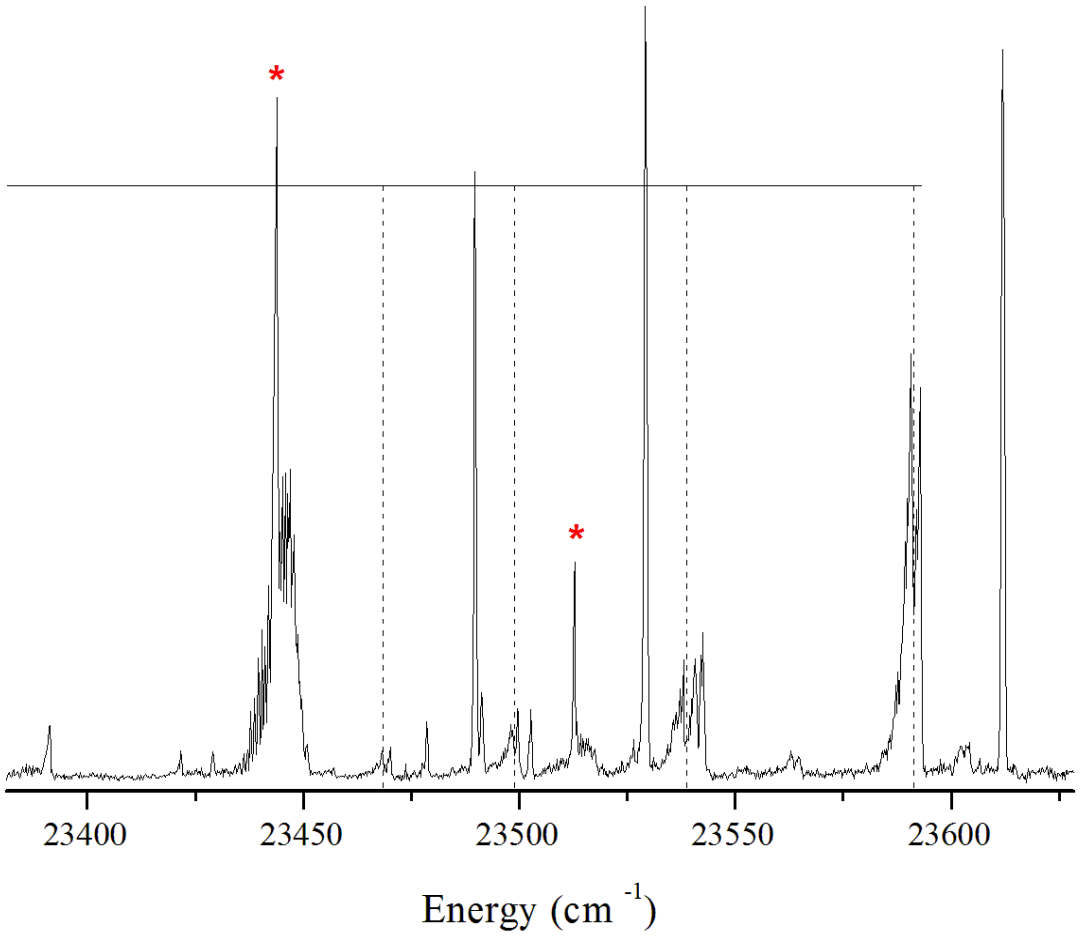

FIGURE 2.2.

Rotationally-resolved LIF spectrom of the ThS [22.12]1-$X^1\Sigma^+$ band. The upward going trace is the experimental data, and the inverted trace is a simulation with an assumed rotational temperature of 28 K. See text for details.

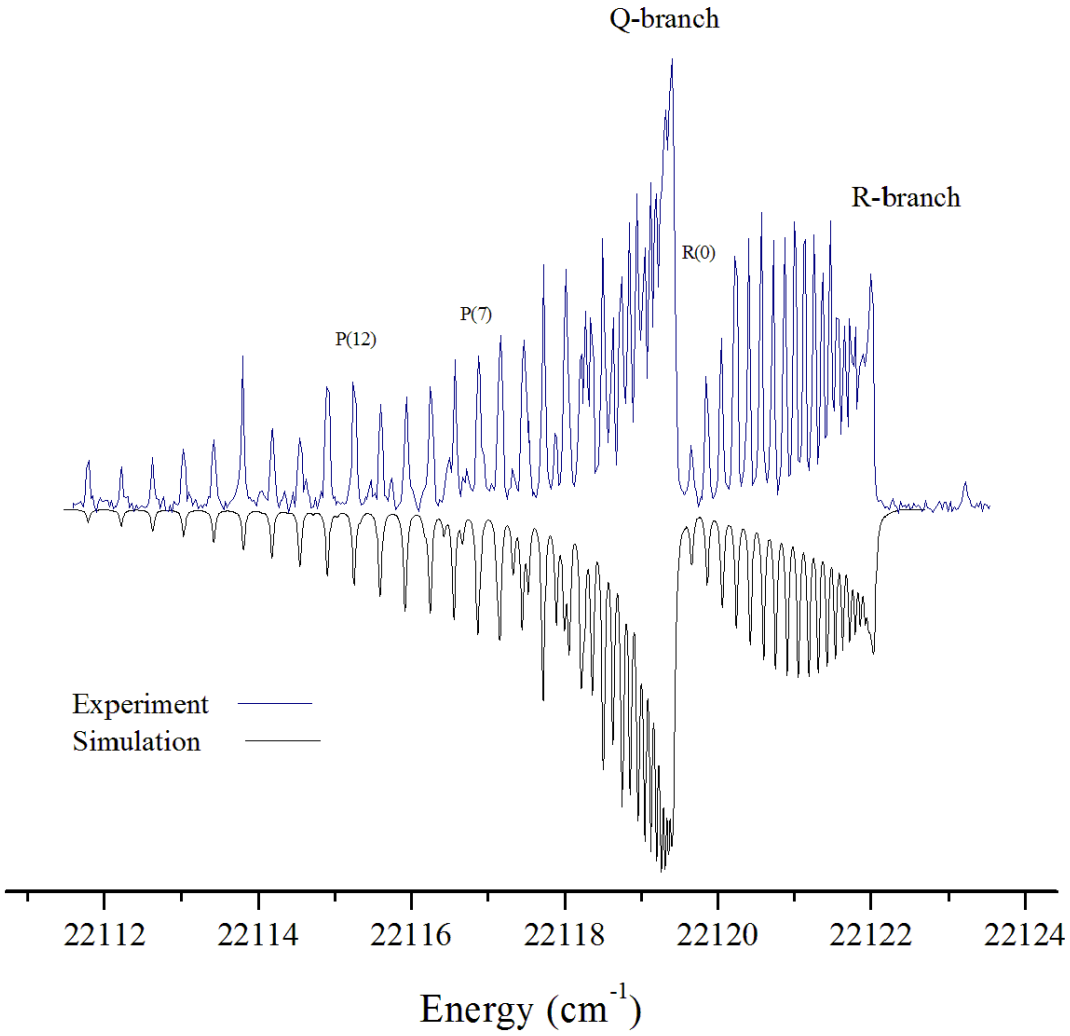

FIGURE 2.3.

Dispersed fluorescence spectrum for ThS recorded using excitation of the [22.12]1-$X^1\Sigma^+$ band.

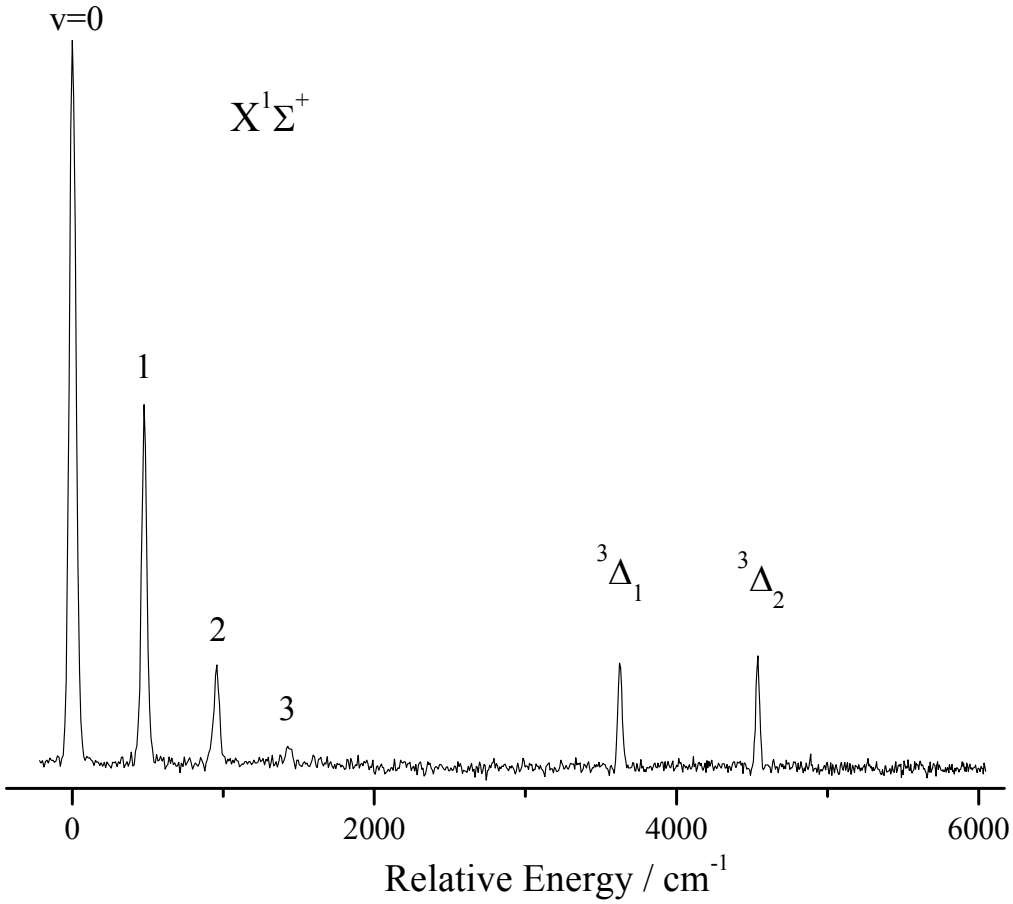

FIGURE 2.4.

Two-color PIE spectrum recorded with the first laser set to excite the {18.53}1−$X^1\Sigma^+$ transition. The lower trace shows the spectrum obtained by monitoring the Th^+ ion channel. This calibration signal was produced by one-color, two-photon ionization.

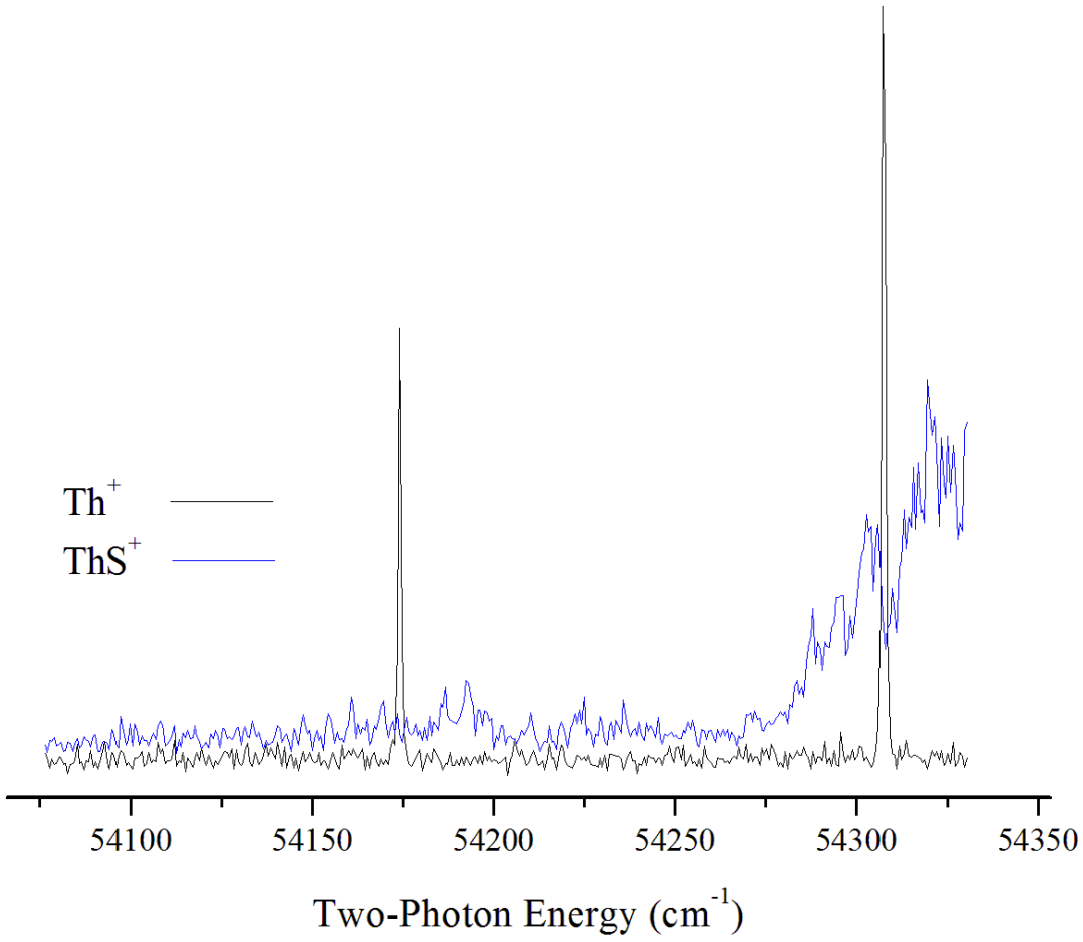

FIGURE 2.5.

PFI−ZEKE scan of ThS. This trace was recorded with the first photon tuned to excite the {23.59}1−$X^1\Sigma^+$ band. This spectrum comprises several dye ranges for the ionizing laser. The baseline noise at 57500 cm^{-1} is due to background electrons in the apparatus generated from multiphoton processes. A functional fit to the dye laser power curve has been subtracted from the data in the range 57250−58250 cm^{-1} .

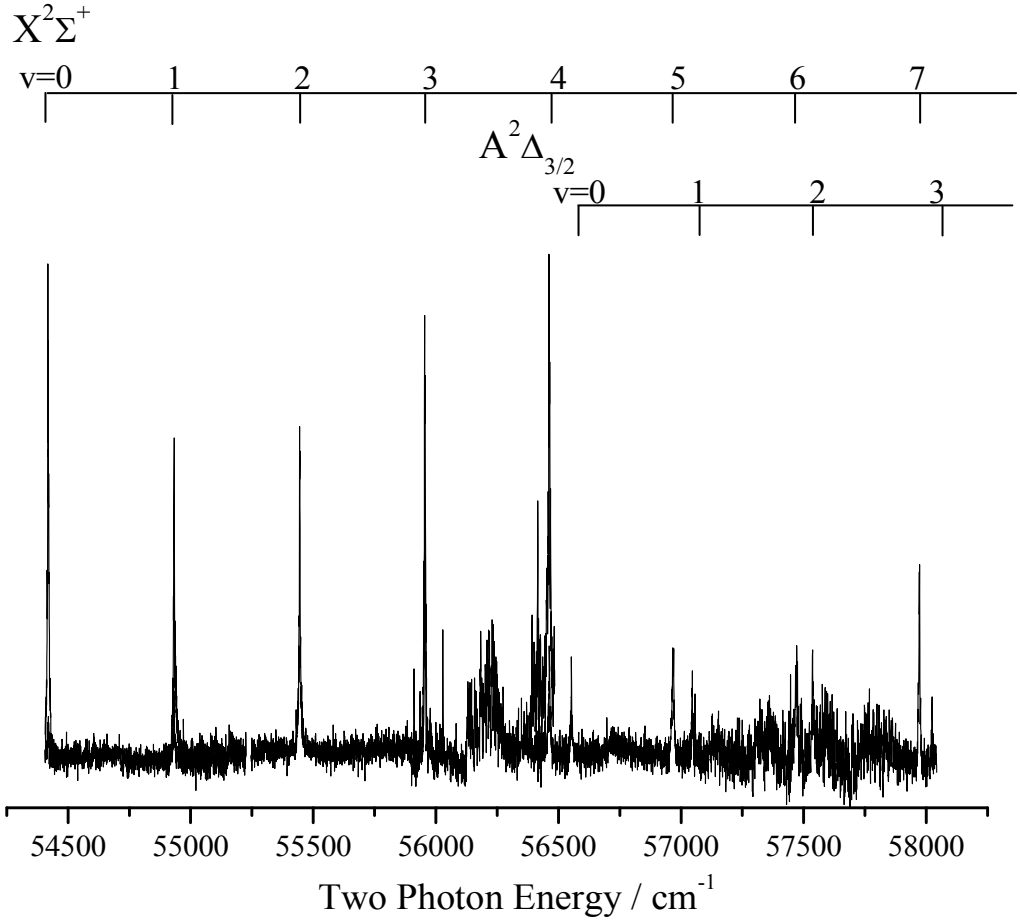

Chapter 3

Spectroscopic and Theoretical Measurements of the Low-Lying States of ThCl and $ThCl^+$

3.1. INTRODUCTION

Actinide compounds are a generally under-studied class of molecules. When considering the importance understanding these molecules poses to applications such as nuclear waste processing schemes, the absence of experimental data is a hindrance. In particular, rational ligand design for efficient actinide/lanthanide (Ac/La) separation is vital for improving these waste recycling schemes. Nuclear by-products are chemically complex, where the lanthanides exist as radioactive decay products *in situ* with unused actinide fuel, and both the 4f and 5f metals can adopt the same oxidation states.[1] Selective Ac/La ligand synthesis is currently driven by trial-and-error approaches.[2] A great deal of cost could be reduced, therefore, if the Ac/La selectivity for a proposed ligand could be predicted accurately prior to synthesis, i.e., via computational approaches. In recent years there has been considerable effort in this area,[2-4] but the consistent shortcoming is that the accuracy of theoretical treatment of the heavy metals is

always in question. When dealing with large atoms, the number of electrons, the number of orbitals, and the number of protons in the nucleus involved all lead to a complicated problem for which approximations must be made. In such cases, it is vital to benchmark theoretical results; for actinide molecules, this becomes difficult due to the scarcity of data. In order to evaluate the perfomance of the computational methods, gas-phase spectra recorded on small molecules are helpful. The molecular constants and quantum state energies extracted from spectra are directly relatable to the theoretical results.

In previous studies,[5-8] we have examined several diatomic molecules and cations containing thorium. Thorium is a particularly appealing candidate for these studies because its electronic structure is relatively simple, arising from a $[Rn]6d^27s^2$ configuration, and assigning its spectra has proven straightforward. Having performed gas-phase spectroscopy for ThN, ThO, ThF, ThS, and the respective cations, the next step in this experimental series is to address ThCl. ThCl is valence isoelectronic to ThF, and given the results discussed in Ref. 8 for ThO and ThS, it is reasonable to expect similar electronic structure patterns between the two. In particular, ThF and ThF^+ are known to have ground state electronic configurations $^2\Delta_{3/2}$ and $^3\Delta_1$, respectively.[7,9] For ThF^+, the spin-orbit energies between Ω = 1,2, and 3 components of this Δ state are 1052 cm^{-1} and 2097 cm^{-1}, respectively. The asymmetry of the spin-orbit energy is due to the high number of low-lying states interacting, which in turn insists that the spin-orbit energy be treated explicity by calculations. This invalidates an approximation sometimes made when comparing spin-free results to spin-explicit results; i.e., that the spin-orbit splitting is symmetrical. The vibration and rotation constants for ThF also shift upon ionization,[7]

following the trend observed for ThO and ThS,[6,8] and so we anticipate a similar behavior with ThCl. The changes in rotation and vibration constants for these three molecule/ion pairs are outlined in Table 3.1.

Almost no literature electronic data exists for gas phase ThCl, although a fair number of studies have been performed on gas phase $ThCl_4$. Consequently, theoretical studies to date have also been performed almost exclusively for $ThCl_4$. A mass spectrometry study of torsion-effusion vaporized $ThCl_4$ recorded the thermochemical properties of $ThCl_n$ (n=1,2,3,4) and also reported the ionization potential of ThCl to be 6.2(3) eV at 2000 K.[10] This experiment did not directly determine vibrational frequency for ThCl, but report that ω_e = 290 cm^{-1} or 370 cm^{-1},[11,12] both of which were estimated from thermal functions in previous mass spectrometry studies. The 290 cm^{-1} value is adopted without further explanation. The authors of this study also note that the dissociation energies for the reaction,

$$ThCl_n \rightarrow ThCl_{n-1} + Cl \qquad (1)$$

follow a qualitatively identical pattern to those of a similar study undertaken for ThF_n. However, the dissociation energy trends the authors observed for UF_n and UCl_n were found to be quite distinct. This may suggest a greater propensity for 5f electrons on U (valence configuration $[Rn]5f^36d7s^2$) to interact with Cl than F. The 5f effects would be greatly diminished for Th, whose 5f orbitals, while energetically accessible, are unoccupied. The following experiments on ThCl thus have the added value of fulfilling a prototypical role when considering experimental design and spectal analysis for the potentially more interesting imminent UCl molecular study with our appraratus.

Theoretical predictions have already been performed to this end for UCl.[13]

3.1.1. Notation

The electronic configurations of the ground and low-lying states of the actinide diatomic molecules are labeled using conventional spectroscopic notation, i.e., using ΛΣ coupling schemes. However, for molecules where the spin-orbit coupling is stronger than the orbital and spin coupling to the intramolecular bond axis, Λ and Σ are compromised, and only their sum, Ω, is a valid quantum number. This is Hund's case c., and is generally the correct way to label the states of the actinide diatomic molecules. Hereafter, electronic state labeling for low-energy states will use ascending numerical ordering within a given Ω value, e.g., rather than the conventional label $A^2\Delta_{5/2}$ for the first excited state of ThF, notation here will be (1)2.5, since this is the first $\Omega = 2.5$ state. For higher-energy states, where an unknown number of states lie at lower energies, states are labeled as $\{T_0/10^3\}\Omega$, where T_0 is the band origin in wavenumbers. Where a band can be identified as a part of a vibrational progression, the curly brackets are replaced with square brackets and the origin of the progression is listed, with the vibration quantum number noted explicitly, i.e., $[T_0/10^3]\Omega\ v = n$.

3.2. EXPERIMENTAL

The equipment used for the following experiments has been described previously.[7]

In order to produce gas phase ThCl, a thorium rod was ablated by a focused pulse from a Nd:YAG laser (Continuum Minilite II, 1064 nm, 10 ns duration) in sequence with the opening of a solenoid pulsed valve (Parker General Series 9) so that the ablated material was entrained in the gas pulse as it expanded into a differentially-pumped vacuum chamber with an ultimate pressure of 10^{-6} torr. The gas admitted by the pulsed valve was helium seeded with a reactive amount of chlorine (0.5-1.5% Cl_2, natural isotopic abundance). The free-jet expansion rotationally cooled its contents (T_{rot} ~10 K), and at a distance ~0.25 m from the nozzle, passed through a skimmer into a second vacuum chamber (10^{-8} torr) which produced a well-collimated molecular beam. This beam enters a series of ion optics which could be configured to deflect cations into a time-of-flight mass spectrometer (TOFMS) or to detach weakly-bound electrons with a voltage pulse towards a detector, depending on the desired experiment.

As there have been no previous spectroscopic studies of ThCl, laser-induced fluorescence (LIF) spectroscopy was performed over the energy ranges 18900 – 20300 cm^{-1}, 21200 – 22000 cm^{-1}, and 23400 – 23550 cm^{-1} using the output of a Nd:YAG-pumped tunable dye laser (ScanMate Pro, linewidth 0.15 cm^{-1}), a section of which is shown in Fig. 3.1. In order to confirm assignment of ThCl features, resonant multi-photon ionization (REMPI) was performed on the molecular beam by counter-propagating a second Nd:YAG-pumped tunable dye laser (Continuum ND6000 series, linewidth 0.08 cm^{-1}) with the first. The second laser output was frequency-doubled, and precise timing of the lasers was achieved using digital delay generators (Stanford Research Systems, Inc., Model DG535) so that the laser pulses intersected the molecular

beam, with the second laser arriving 10-50 ns after the first laser. The first laser could be tuned through resonances believed to belong to ThCl, and the $ThCl^+$ signal recorded by the TOFMS would then be examined for replicated band contours between the LIF and REMPI experiments. Calibration of the Nd:YAG-pumped dye lasers was performed by a wavelength meter (Bristol Instruments, 821 Series, ±0.02 cm^{-1}); for the ScanMate Pro, calibration points were recorded simultaneously with recording a fluorescence spectrum, but only for ThCl features of interest, while for the ND6000, the wavelength of the fundamental output was continuously monitored.

Within the energy range examined by LIF, only one ThCl band was observed – at 21977.60(15) cm^{-1} – for which there was no interference when assigning rotational lines. This interference usually came from overlapping ThO bands and ThCl bands belonging to the $Th^{37}Cl$ isotopomer; due to its abundance, $Th^{35}Cl$ was chosen as the primary focus for this study. An intracavity etalon was installed in order to improve the linewidth to 0.06 cm^{-1} which was sufficient to record a rotationally-resolved LIF spectrum, see Fig. 3.2. The energy of this feature proved suitable for two-color ionization experiments, i.e., was less than half of the ionization energy. Another band that was partially overlapped by high-*J* ThO features, at 23514.35(15) cm^{-1}, was pumped in fluorescence dispersion experiment, using a monochromator (Jarrell-Ash model 82−410, 1180 line/mm grating, 0.5 mm slit width) to disperse the emitted photon wavelengths. The monochromator was scanned in order to record a spectrum of the low-lying states of ThCl. This dispersed fluorescence spectrum recorded from this state is shown in Fig. 3.3.

To obtain an initial estimate of the ionization potential (IP), a two-color

photionization experiment was performed in which the band-head of the 21977.60(15) cm^{-1} feature was pumped by the first laser while the ionizing laser was tuned to successively lower energy. This procedure yielded a photoionization efficiency spectrum (PIE), Fig. 3.4. The ionization potential was estimated by the energy at which depletion of the $Th^{35}Cl^{+}$ signal was observed, as monitored by the TOFMS. Due to the energies of the photons involved in the process, some features in the PIE spectrum result from absorption of two ultraviolet photons to ionize ThCl, as opposed to a single visible photon followed by a single ultraviolet photon. To some extent, the one color, two-photon ionization could be reduced by attenuation of the ultraviolet laser power, but the overall signal-to-noise ratio suffered as a result.

After recording the PIE spectrum, the IP was then refined by two-color pulsed-field ionization zero kinetic energy photoelectron spectroscopy (PFI-ZEKE). PFI-ZEKE is a theshold ionization technique in which the two-photon ionization sequence is used to excite the molecule to a series of Rydberg states converging on the ionization limit, wherein the electron is just below the energy required for ionization. As Rydberg states are long-lived, an electron in these levels can be temporally separated from any electrons produced by non-resonant ionization processes (which promptly leave the ion), and a small voltage pulse supplied after some delay (typically 0.5 V cm^{-1} pulse, 2 μs delay) is sufficient to ionize and deflect the Rydberg electron to the detector. This technique has the advantage of discriminating against the one color, two-photon ionization processes, and yields the rovibronic levels of the ion as populated by the two-color threshold ionization process. PFI-ZEKE has been used to determine the ionization potential and

rovibronic states of the associated cation in a number of studies using this apparatus.[5-8] Beyond the observation of the first feature of $ThCl^+$with PFI-ZEKE, a number of higher energy states have been observed with this technique. The bands are shown in Fig. 3.5 while their energies relative to the lowest-energy feature are listed in Table 3.5. The PFI-ZEKE experiments are ongoing.

3.2.1. Computational Treatment of Ground and Low-Lying Excited States

Kirk Peterson and Sam Battey at Washington State University have calculated the low-lying states of ThCl and $ThCl^+$ in support of the experimental efforts. Their methods and results are described here. The MOLPRO[14] *ab initio* computational suite was used to carry out all calculations unless stated otherwise. The basis sets utilized in this work were cc-pV*n*Z-PP (*n*=D,T,Q) for Th[15] and aug-cc-pV(*n*+d)Z for Cl.[16] The relativistic pseudopotential used on Th in this study corresponded to the small core (60 electron) energy consistent potential of Dolg and Cao,[17] which was adjusted to multiconfiguational Dirac-Hartree-Fock reference data (with Breit contributions). Below, these basis sets will be denoted as V*n*Z-PP and V*n*Z. Two separate extrapolation schemes were used to reach the complete basis set (CBS) limit. The Karton and Martin formula[18] was used to extrapolate the complete active space self-consistent field (CASSCF) or Hartree-Fock (HF) energies using TZ and QZ basis sets,

$$E_n^{HF} = E_{CBS}^{HF} + A(n+1)e^{-6.57\sqrt{n}} \qquad (2)$$

Where *n* corresponds to the cardinal number of the basis set (3 for TZ and 4 for QZ)

rather than the ℓ_{max}. The correlation energy was extrapolated using TZ and QZ energies according to[19]

$$E_n^{corr} = E_{CBS}^{corr} + \frac{B}{\left(n+\frac{1}{2}\right)^4} \quad (3)$$

Probing the low-lying ΛS excited states of ThCl and $ThCl^+$ was done using the CASSCF method using a V*n*Z-PP basis. The expectation value of L_z^2 was calculated to ensure that both degenerate states of each Λ state were included. The active space in this work included 3 electrons in 9 orbitals for ThCl and 2 electrons in 9 orbitals for $ThCl^+$. These orbitals were dominated by Th 7s, 6d and 7p character. All lower energy orbitals (including the outer core of Th and both the core and valance shells of Cl) were constrained to be doubly occupied. The 5f subshell of thorium did not show significant occupation and was thus excluded from study. The CASSCF calculations were followed by second-order perturbation theory calculations, CASPT2,[20] and used the same active space as in the preceding section. Intruder states were considered and accounted for by using a minimal IPEA level shift[21] of 0.25 for all included states at each bond length.

The state interacting method as implemented in MOLPRO was used to calculate the molecular spin-orbit *Ω* states. In this method, the spin-orbit eigenstates are obtained by diagonalizing $H_{el} + H_{SO}$ in a basis of H_{el} eigenstates. The SO matrix elements were calculated at the CASSCF level of theory while the diagonal terms used the CASPT2 energies. The off-diagonal matrix elements were calculated with the VQZ basis sets and the diagonal terms utilized CASPT2 energies extrapolated to the CBS limit.

In chosing the number and identity of ΛS states to include in the state-interacting

approach, the assumption was made that each molecule could be represented as a closed shell Cl^- atom interacting with a Th^+ or Th^{2+} ion. This gives rise to 10 ΛS electronic states in ThCl, 4 of which result from the ^2D ($7s^26d^1$) state of Th^+ and 6 from the ^4F ($7s^16d^2$) configuration. The term energies and molecular constants of the lowest-energy states are reported in Table 3.2. For $ThCl^+$, this gives rise to 4 ΛS states: a single state from the ^1S ($7s^26d^0$) term and 3 from the ^3D ($7s^16d^1$) term. The term energies and molecular constants of these states are reported in Table 3.3. This strategy has been previously used to obtain accurate spectroscopic properties for UF, UF^+, UCl, and UCl^+.[22,23]

Diatomic potential energy curves were obtained by calculating energies at 7 bond lengths distributed around r_e ($r-r_e$=-0.3, -0.2, -0.1, 0.0, +0.1, +0.3, +0.5 bohr). After fitting the energies to polynomials in simple displacement coordinates, vibrational energy levels were obtained using the LEVEL 8.2 package.[24] The harmonic frequencies and anharmonic constants were obtained by fitting the 5 lowest vibrational energy levels to the usual expression:

$$E_v = \omega_e\left(v+\frac{1}{2}\right) - \omega_e\chi_e\left(v+\frac{1}{2}\right)^2 \qquad (4)$$

3.2.2. Ab Initio Composite Treatment for the IP of ThCl

The Feller-Peterson-Dixon (FPD) composite thermochemistry method[25] was used to accurately determine the ionization potential (IP) of ThCl. The contributions included in the IP calculation corresponded to,

$$E_{IP} = E_{VQZ} + \Delta E_{CBS} + \Delta E_{CV} + \Delta E_{SO} + \Delta E_{QED} + \Delta E_{ZPE} \qquad (5)$$

which has been used previously[7] for the thermochemistry of several actinide-containing molecules. Except for the spin-orbit contribution (ΔE_{SO}), calculations were carried out at the singles and doubles coupled cluster with perturbative triples level of theory, CCSD(T)[26-28] with the 3rd-order Douglas-Kroll-Hess scalar relativistic Hamiltonian.[29] These calculations were carried out using cc-pV*n*Z-DK3 and aug-cc-pV(*n*+d)Z-DK for Th and Cl, respectively (*n*=T, Q).[30] The same extrapolation methods as described above were used to estimate the CBS limits. The contribution to the IP for outer-core correlation, ΔE_{CV}, was obtained as the difference in two calculations on each diatomic, one at the frozen-core level and one with the outer-core (5s5p5d for Th and 2s2p for Cl) correlated, both in the same basis sets, cc-pwCV*n*Z-DK3 for Th and aug-cc-pwCV*n*Z-DK for Cl. [31] The contribution was then extrapolated to the CBS limit. The spin-orbit contribution utilized the all electron exact 2-component (X2C) Hamiltonian[32] in the DIRAC[33] software package. Electron correlation effects were recovered using the intermediate Hamiltonian Fock-Space coupled cluster method, IH-FSCCSD[34] with an uncontracted VDZ-DK basis set. The intermediate Hamiltonian method was required due to heavy interference from intruder states. The active space was defined by orbital energies between –2.5 and 15 E_h, which consistently includes the same frozen core approximation as in MOLPRO (but with truncation of the virtual orbital space in the former). A correction from the leading term of quantum electrodynamics (ΔE_{QED}), the Lamb shift, was obtained by using a local potential on Th for both the vacuum polarization and self-energy contributions as first described by Pyykko and Zhao[35] (see Ref. 14 for the current implementation). These calculations used were carried out at the

CCSD(T)/wCVDZ-DK level with the DKH3 Hamiltonian. Finally, the zero-point energy contribution to the IP was calculated using harmonic frequencies obtained at the CCSD(T)/VTZ-PP level of theory.

3.3. RESULTS AND DISCUSSION

Fig. 3.2. shows the rotationally-resolved visible feature of $Th^{35}Cl$ at 21977.60 cm^{-1}. The downward-going trace is a simulation obtained using the program PGOPHER,[36] which was used to analyze the spectrum by least-squares fitting, assuming a rotational temperature of 8 K. This procedure determined rotation constants for the ground and excited states, $B'' = 0.0891(2)$ cm^{-1} and $B' = 0.0823(2)$ cm^{-1}. The first rotation lines in the P and R branches are P(2.5) and R(1.5), which indicates that the lowest J values in both the ground and excited states are $J = 1.5$, and so this transition is initially labeled {21.98}1.5 – X(1)1.5. This experimental confirmation that the ground state $\Omega = 1.5$ is consistent with ThF electronic structure, and is also supported by the CASPT2 results.

The dispersed fluorescence spectrum obtained by pumping the state at 23514.63 cm^{-1} reveals some of the low-lying states of ThCl, shown in Fig. 3.3, and was assigned using the CASPT2 predictions with an assumption of $\Omega' = 0.5$. Without a rotationally-resolved spectrum, this Ω assignment is not definitive. The {23.5}0.5 – X(1)1.5 transition is partially overlapped by a ThO feature, and so rotational analysis of this band was hindered. Under the $\Delta\Omega = 0, \pm 1$ selection rules, this choice excludes state (1)2.5

from the analysis, which does not appear in the spectrum. However, emission to (1)0.5 and (4)1.5 are allowed transitions, but neither state is observed in the spectrum. Nonetheless, assumption of $\Omega' = 1.5$ or 2.5 produced less agreeable assignments. For the electronic states that are identified in the spectrum, there is a small, somewhat consistent offset (~180 cm^{-1}) to the calculated term energies. To obtain experimental vibration constants, the progressions were then fit to the expression,

$$T_e = T_0 + \omega_e\left(v+\frac{1}{2}\right) - \omega_e x_e\left(v+\frac{1}{2}\right)^2 \qquad (6)$$

although only the first-order terms of this expression were used for the excited states of ThCl. The resulting vibration constants are listed in Table 3.4 and compared with predictions. For the ground state, the vibration and anharmonicity constants obtained from equation (6) were ω_e = 339(1) cm^{-1} and $\omega_e x_e$ = 1(1) cm^{-1}. This value for ω_e falls between the two previous thermochemical estimations (ω_e = 290 cm^{-1} or 370 cm^{-1}),[11,12] but is in excellent agreement with the CASPT2 calculations.

Both the {21.98}1.5 and {23.5}0.5 features were confirmed to belong to $Th^{35}Cl$ using REMPI. The $Th^{35}Cl^+$ current produced a rotation contour matching that of the LIF spectrum, and the R band-head of the corresponding $Th^{37}Cl$ band was also observed to the red of the P branch of the $Th^{35}Cl$ band. Rotationally-resolved REMPI spectra could not be obtained, as laser power needed for the two-photon ionization process broadened the spectra features; therefore, only transitions to a vibrationally-excited upper state, for which the isotopologue features are well separated in energy, could be used for initial rotational assignments. Using the harmonic oscillator description of the vibration constant,

$$\omega_e = \hbar\sqrt{\frac{k}{\mu}} \qquad (7)$$

the ground state vibration constant for the heavier isotopologue can be approximated from that of $Th^{35}Cl$ as 330(1) cm^{-1}. Since the $Th^{37}Cl$ band belonging to the same $Th^{35}Cl$ {21.98}1.5 feature is ~8 cm^{-1} lower in energy, substitution of the vibrational interval for the observed excited state into equation (7), under the assumption that this transition originates from $v = 0$ level of the ground state, allows one to back out the vibrational quantum number of the excited state from equation (6) that would produce this isotopic shift. By this procedure, we determine $v' = 1$. Therefore, this state is tentatively identified as [21.7]1.5 $v = 1$.

The PIE spectrum obtained as described in section 3.2 is shown in Fig. 3.4. The intersection of linear regression to the baseline and to the onset feature in the PIE spectrum provided an IP estimate of 51720(10) cm^{-1}. When PFI-ZEKE spectra were recorded, however, the corresponding feature was located at 51744(3) cm^{-1}. The discrepancy between the two methods of determining the IP is ascribed to one-color ionization features as described above convoluting the PIE analysis. There is some suggestion from recent experiments that the IP value recommended by this PIE/PFI-ZEKE process may not belong to the ionic origin band. This value is within the experimental error of the previously-determined[9] IP of ThCl, but could just as easily correspond to PFI-ZEKE observation of a vibrationally-excited level of $v^+ \leq 10$ (using the vibration constants predicted by CASPT2 for $Th^{35}Cl^+$) and still satisfy these criteria. Therefore, we report this value as an upper limit to the IP until it is confirmed to our satisfaction to be the lowest-energy state observed. This number is in poor agreement

with the initial estimate from CASPT2 adiabatic detachment energy, but agrees reasonably well with the CCSD(T) value. 51744(3) cm^{-1} is higher than IP_{ThF} = 51581(3) cm^{-1}. Likewise, the IP_{ThS} exceeds the IP_{ThO} (see Table 3.1), although this is by no means quantitatively consistent: the difference between the 2nd and 3rd row thorium chalcogen IPs is 1172 cm^{-1} as opposed to the 163 cm^{-1} difference between the 2nd and 3rd row thorium halide IPs, at the current best estimate (which is a maximum value).

For the higher-lying states observed by PFI-ZEKE, no attempt has been made to fit to equation (6), due to the high number of electronic states observed so far and incomplete status of the PFI-ZEKE experiments. The first excited feature of the PFI-ZEKE spectrum appears at 77(3) cm^{-1}, which is inconsistent with the CASPT2 calculated appearance of the first excited state (595.95 cm^{-1}), but until a more complete survey of PFI-ZEKE features is complete, it is unclear whether this is a shortcoming of the calculations, or evidence that the PFI-ZEKE spectra do not contain the $X^+(1)1$ $v^+ = 0$ level. Furthermore, the signal-to-noise ratio of the PFI-ZEKE spectra so far have proven to be insufficient to determine rotation constants of the ion. Therefore, only the energies of the center positions of the observed bands are reported, as T_e, in Table 3.5.

The predictions for the rotation and vibration constants of $Th^{35}Cl^+$ are completely consistent with the trend established by ThO^+ and ThS^+,[6,9] when considering ThF^+ as well.[7] It has been previously noted[5-8] that ionization results in a decrease in bond length and an increase in vibration frequency for the molecule. While we cannot yet report an experimental vibration frequency for $Th^{35}Cl^+$, the vibration frequency trend is supported by the calculations, resulting in predictions of ω_e = 346.58 cm^{-1} versus $\omega_e{}^+$ = 405.58 cm^{-1}.

Likewise, the rotation constants are predicted to fit the established pattern, with predicted B_0 = 0.0888 cm^{-1}, and B_0^+ = 0.0939 cm^{-1}. To further establish the accuracy of the calculations for $ThCl^+$, we can take into account the spin-orbit interval for the Ω =1 and Ω = 2 states. For the same states of ThO and ThS, which are valence isoelectronic to ThF^+ and $ThCl^+$, these intervals were 811.3(3) cm^{-1} and 911(6) cm^{-1}.[6,8] For ThF^+, this interval is 1052.5(5) cm^{-1},[7] and the first Ω = 2 state of $ThCl^+$ is predicted at 1503.72 cm^{-1} by CASPT2. This is a consistent ~10^3 cm^{-1} energy split, taking into account that the neutral term energies were overestimated by up to 200 cm^{-1}, and in both cases the 3p ligand is predicted to have the higher interval than the 2p ligand. Therefore, this prediction also suggests that the calculations are reliable. Any further assessment must attend more experimental results.

3.4. SUMMARY

Electronic spectra of $Th^{35}Cl$ have been recorded for the first time, identifying the rotation and vibration constants for the neutral molecule. CASPT2 and CCSD(T) calculations using the reliable[7,8] 60-electron-in-core relativistic pseudopotential[17] for Th have been used to assist in state assignments. For the ground state of the neutral molecule, the calculations are in excellent agreement with experiment. Term energies of the excited states are somewhat overestimated, as are the vibration constants. We currently recommend an ionization energy for ThCl of 6.4152(3) eV, in agreement with and more precise than the previous value of 6.2(3) eV. The appearance potential of the

ion is drastically overestimated by CASPT2 calculations, and slightly underestimated by the CCSD(T) calculations. The CASPT2 calculations also predict both an increase in vibration frequency and bond length contraction upon ionization, which is consistent with previous trends when considering the thorium-containing diatomic molecules.

Ultimately, as the electronic structure patterns of ThCl have not been observed to deviate from the established trends in previously-observed molecules, we can conclude that the 5f orbitals do not have any increasing influence on the low-lying states of ThX or ThX^+ when considering X = F, Cl.

REFERENCES

(1) H. H. Dam, D. N. Reinhoudt, and W. Verboom, *Chem. Soc. Rev.* **36**, 367-377 (2007).

(2) V. S. Bryantsev and B. P. Hay, *Dalton Trans.* **44**, 7935 (2015).

(3) H. Wu, Q.-Y. Wu, C.-Z. Wang, J.-H. Lan, Z.-R. Liu, Z.-F. Chai, and W.-Q. Shi, *Dalton Trans.* **44**, 16737-16745 (2015).

(4) A. Sengupta, Sk. M. Ali, and K. T. Shenroy, *Polyhedron* **117**, 612-622 (2016).

(5) V. Goncharov, J. Han, L. A. Kaledin, and M. C. Heaven, *J. Chem. Phys.* **122**, 204311 (2005).

(6) V. Goncharov and M. C. Heaven, *J. Chem. Phys.* **124**, 064312 (2006).

(7) B. J. Barker, I. O. Antonov, M. C. Heaven, and K. A. Peterson, *J. Chem. Phys.* **136**, 104305 (2012).

(8) J. H. Bartlett, I. O. Antonov, and M. C. Heaven, *J. Phys. Chem. A* 117, 12042-12048 (2013).

(9) D. N. Gresh, K. C. Cossel, Y. Zhou, J. Ye, and E. A. Cornell, *J. Mol. Spec.* **319**, 1-9 (2016).

(10) K. H. Lau and D. L. Hildenbrand, *J. Chem. Phys.* **92**, 6124-6130 (1990).

(11) O. Knacke, F. Mueller, and E. van Rensen, *Z. Phys. Chem.* **80**, 82 (1972).

(12) D. D. Wagman, R. H. Shumm, and V. B. Parker, Natl. Bur. Stand. Rept. No. NBSIR-77-1300, 1977.

(13) D. H. Bross and K. A. Peterson, *J. Chem. Phys.* **143**, 184313 (2015).

(14) H.-J. Werner, P. J. Knowles, G. Knizia, F. R. Manby, M. Schütz *et al.*, MOLPRO, version 2012.1, a package of *ab initio* programs, 2012, see **http://www.molpro.net**.

(15) K. A. Peterson, *J. Chem. Phys.* **142**, 074105 (2015). http://dx.doi.org/10.1063/1.4907596

(16) T. H. Dunning, Jr., K. A. Peterson, and A. K. Wilson, J. Chem. Phys. **114**, 9244 (2001).; D. E. Woon and T. H. Dunning, Jr., J. Chem. Phys. **98**, 1358 (1993).

(17) M. Dolg and X. Cao, *J. Phys. Chem. A* **113**, 12573 (2009). http://dx.doi.org/10.1021/jp9044594

(18) A. Karton and J. M. L. Martin, *Theor. Chem. Acc.* **115**, 330 (2006). http://dx.doi.org/10.1007/s00214-005-0028-6

(19) D. Feller, K. A. Peterson, and J. G. Hill, *J. Chem. Phys.* **135**, 044102 (2011). http://dx.doi.org/10.1063/1.3613639

(20) P. Celani and H.-J. Werner, *J. Chem. Phys.* **112**, 5546 (2000). http://dx.doi.org/10.1063/1.481132

(21) G. Ghigo, B. O. Roos, and P.-Å Malmqvist, *Chem. Phys. Lett.* **396**, 142 (2004). http://dx.doi.org/10.1016/j.cplett.2004.08.032

(22) I. O. Antonov and M. C. Heaven, *J. Phys. Chem. A* **117**, 9684 (2013). http://dx.doi.org/10.1021/jp312362e

(23) D. H. Bross and K. A. Peterson, *J. Chem. Phys.* **143**, 184313 (2015). http://dx.doi.org/10.1063/1.4935492

(24) R. J. LeRoy, *LEVEL 8.2: A Computer Program for Solving the Radial Schrodinger Equation for Bound and Quasibound Levels, Chemical Physics Research*

Report CP-663 University of Waterloo, 2007, see**http://leroy.uwaterloo.ca/programs/**.

(25) D. Feller, K.A. Peterson, D.A. Dixon, *J. Chem. Phys.* **129**, 204105 (2008). http://dx.doi.org/10.1063/1.3008061

(26) P. J. Knowles, C. Hampel, and H.-J. Werner, *J. Chem. Phys.* **99**, 5219 (1993). http://dx.doi.org/10.1063/1.465990

(27) G. E. Scuseria, *Chem. Phys. Lett.* **176**, 27 (1991). http://dx.doi.org/10.1016/0009-2614(91)90005-T

(28) J. D. Watts, J. Gauss, and R. J. Bartlett, *J. Chem. Phys.* **98**, 8718 (1993). http://dx.doi.org/10.1063/1.464480

(29) D. Peng and K. Hirao, J. Chem. Phys. **130**, 044102 (2009); D. Peng and M. Reiher, *Theor. Chem. Acc.* **131**, 1081 (2012).

(30) W. A. de Jong, R. J. Harrison, and D. A. Dixon, *J. Chem. Phys.* **114**, 48 (2001).

(31) K. A. Peterson and T. H. Dunning, Jr., *J. Chem. Phys.* **117**, 10548 (2002).

(32) M. Iliaš, M. and T. Saue, *J. Chem. Phys.* **126**, 4102 (2007).

(33) DIRAC, a relativistic *ab initio*electronic structure program, Release DIRAC14, 2014, written by T. Saue, L. Visscher, H. J. Aa. Jensen, and R. Bast, with contributions from V. Bakken, K. G. Dyall, S. Dubillard, U. Ekström, E. Eliav, T. Enevoldsen, E. Faßhauer, T. Fleig, O. Fossgaard, A. S. P. Gomes, T. Helgaker, J. Henriksson, M. Iliaš, Ch. R. Jacob, S. Knecht, S. Komorovský, O. Kullie, C. V. Larsen, J. K. Lærdahl, Y. S. Lee, H. S. Nataraj, P. Norman, G. Olejniczak, J. Olsen, Y. C. Park, J. K. Pedersen, M. Pernpointner, R. di Remigio, K. Ruud, P. Sa^{3}ek, B. Schimmelpfennig, J. Sikkema, A. J. Thorvaldsen, J. Thyssen, J. van Stralen, S. Villaume, O. Visser, T. Winther, and S.

Yamamoto, see **http://www.diracprogram.org**.

(34) A. Landau, E. Eliav, U. Kaldor, *Chem. Phys. Lett.* **313**, 399 (1999). http://dx.doi.org/10.1016/S0009-2614(99)01067-2

(35) P. Pyykko and L. Zhao, *J. Phys. B*. **36**, (2003).

(36) C. M. Western; *PGOPHER, A Program for Simulating Rotational Structure*; University of Bristol: Bristol, U.K., 2007.

(37) S. D. Gabelnick, G. T. Reedy, and M. G. Chasanov, *J. Chem. Phys.* **60**, 1167 (1974).

TABLE 3.1. Change in Molecular Constants for ThO, ThF, and ThS upon Ionization[a]

Molecule	IP	ω_e	B_0
ThO →	53253.8(2)[b]	895.77[e]	0.332644[e]
ThO^+		954.97(6)[b]	0.3450(6)[b]
ThS →	54425(3)[c]	479(1)[c]	0.1074[g]
ThS^+		517(2)[c]	0.1114[g]
ThF →	51581(3)[d]	605(15)[d]	0.237(5)[d]
ThF^+		656.96(1)[f]	0.24264(3)[f]

[a] All energies are in cm^{-1}.

[b] Ref. 6

[c] Ref. 8

[d] Ref. 9

[e] Ref. 37

[f] Ref. 8. Calculated by CASSCF/MRCI/SO. An experimental B_0 exists in agreement with the calculation for ThS, but could not be determined for the ion.

TABLE 3.2. Calculated Low-Lying States of ThCl[a]

State[b]	T_e	R_e / Å	ω_e	$\omega_e x_e$	ΛS Comp.
X(1)1.5	0	2.499	346.58	0.91	92% $^2\Delta$ + 7% $^2\Pi$
(1)0.5	1820.625	2.544	332.67	0.89	81% $^2\Pi$ + 10% $^2\Sigma$ + 4% $^4\Pi$ + 3% $^4\Sigma$
(1)2.5	3015.948	2.491	350.06	0.99	99% $^2\Delta$
(2)1.5	3641.356	2.724	329.48	1.47	92% $^4\Phi$ + 4% $^4\Delta$
(2)0.5	4107.448	2.539	327.83	0.83	75% $^4\Sigma$ + 14% $^4\Pi$ + 9% $^2\Pi$ + 2% $^2\Sigma$
(3)1.5	4288.045	2.541	335.23	0.88	62% $^2\Pi$ + 20% $^4\Sigma$ + 9% $^4\Pi$ + 5% $^2\Delta$ + 3% $^4\Phi$
(4)1.5	4796.337	2.526	337.15	0.53	70% $^4\Sigma$ + 26% $^2\Pi$ + 2% $^4\Pi$ + 2% $^2\Delta$
(2)2.5	5198.502	2.567	326.60	0.63	92% $^4\Phi$ + 6% $^4\Delta$
(1)3.5	6924.394	2.570	323.64	0.85	95% $^4\Phi$ + 5% $^4\Delta$
(3)0.5	6943.863	2.572	318.61	0.89	64% $^4\Pi$ + 22% $^2\Sigma$ + 14% $^4\Delta$
(4)0.5	7765.017	2.637	325.84	0.92	60% $^4\Pi$ + 34% $^2\Sigma$ + 3% $^2\Pi$
(5)1.5	7827.201	2.562	326.94	0.89	69% $^4\Pi$ + 16% $^4\Delta$ + 8% $^4\Sigma$ + 5% $^2\Pi$ + 2% $^4\Phi$
(3)2.5	7928.653	2.566	323.47	0.86	88% $^4\Pi$ + 8% $^4\Delta$ + 3% $^4\Phi$
(5)0.5	8136.028	2.552	329.22	0.94	33% $^4\Pi$ + 31% $^2\Sigma$ + 19% $^4\Sigma$ + 10% $^4\Delta$ + 7% $^2\Pi$
(1)4.5	8901.009	2.571	324.31	0.84	100% $^4\Phi$
(6)0.5	10073.500	2.579	316.44	0.75	74% $^4\Delta$ + 25% $^4\Pi$
(6)1.5	11197.680	2.580	313.40	0.82	79% $^4\Delta$ + 18% $^4\Pi$ + 2% $^4\Phi$
(4)2.5	11991.510	2.582	311.33	0.85	85% $^4\Delta$ + 10% $^4\Pi$ + 4% $^4\Phi$

[a] All values in cm^{-1} except where noted. CASPT2 calculations. See text for details.

[b] States are labeled in ascending numerical order, grouped by Ω

TABLE 3.3. Calculated Low-Lying States of $ThCl^{+}$[a]

State[b]	T_e	R_e / Å	ω_e	$\omega_e x_e$	ΛS Comp.
X(1)1	0	2.429	405.58	0.81	95% $^3\Delta$ + 3% $^3\Pi$ + 3% $^1\Pi$
(1)0	595.95	2.418	400.70	0.86	91% $^1\Sigma$ + 6% $^3\Pi$ + 3% $^3\Sigma$
(1)2	1503.72	2.426	408.00	0.81	92% $^3\Delta$ + 4% $^3\Pi$ + 3% $^1\Delta$
(1)3	3678.13	2.422	408.90	0.82	99% $^3\Delta$
(2)0	5944.01	2.459	396.85	0.82	100% $^3\Pi$
(2)1	6292.00	2.456	396.25	0.80	91% $^3\Pi$ + 7% $^1\Sigma$
(3)0	6270.16	2.452	404.10	0.82	47% $^3\Pi$ + 46% $^1\Pi$ + 7% $^3\Sigma$
(2)2	6472.56	2.496	378.17	0.89	95% $^3\Phi$ + 3% $^1\Delta$ + 2% $^3\Pi$
(3)1	7711.92	2.464	389.18	0.87	51% $^1\Pi$ + 43% $^3\Pi$ + 5% $^3\Delta$ + 2% $^3\Sigma$
(3)2	8037.68	2.455	398.97	0.72	90% $^3\Pi$ + 6% $^3\Delta$ + 3% $^3\Phi$ + 2% $^1\Delta$
(4)1	8237.91	2.456	394.72	0.71	92% $^3\Sigma$ + 7% $^3\Pi$
(4)0	8353.99	2.455	392.99	0.77	96% $^3\Sigma$ + 2% $^3\Pi$ + 2% $^1\Sigma$
(2)3	9258.70	2.493	381.81	0.76	99% $^3\Phi$
(4)2	10883.79	2.431	400.60	0.84	92% $^1\Delta$ + 4% $^3\Pi$ + 2% $^3\Delta$ + 2% $^3\Phi$
(1)4	11848.83	2.494	380.32	0.79	100% $^3\Phi$

[a] All energies in cm^{-1} except where noted.

[b] States are labeled in ascending numerical order, grouped by Ω

TABLE 3.4. Ground and Excited State Contants of $Th^{35}Cl$

State	T_e	B_e	ω_e	$\omega_e x_e$
X(1)1.5	0	0.0891(2)	339(1)	1(1)
	0	*0.0888*	*346.58*	*0.91*
(1)0.5				
	1820.625	*0.0856*	*332.67*	*0.89*
(1)2.5				
	3015.948	*0.0893*	*350.06*	*0.99*
(2)1.5	3466(5)		321(5)	
	3641.356	*0.0747*	*329.48*	*1.47*
(2)0.5	3974(5)		358(5)	
	4107.448	*0.0860*	*327.83*	*0.83*
(3)1.5	4049(5)		351(5)	
	4288.045	*0.0859*	*335.23*	*0.88*
(4)1.5				
	4796.337	*0.0869*	*337.15*	*0.53*

[a] Regular numbers are experimental values, where observed. Italicized numbers are CASPT2 values. See text for details. All values are in cm^{-1}.

TABLE 3.5. PFI-ZEKE Band Energies Relative to the Ionization Potential

Band	T_e / cm^{-1} [a]
1	0
2	77
3	176
4	199
5	372
6	394
7	703

IP / cm^{-1}	Method
51744(3)	Expt.[b]
54651	CASPT2
51054	CCSD(T)

[a] T_e is the energy of the highest-intensity feature of the band, relative to the IP, with uncertainty ±3 cm^{-1}

[b] See text for discussion of tentative IP assignment.

FIGURE 3.1.

Section of a low-resolution ($\Delta\upsilon$ = 0.15 cm^{-1}) LIF survey spectrum taken on the free jet expansion produced as described above. Predominant features are Th, ThO, and ThCl signals. Feature (*a*) at 21921 cm^{-1} is an example of a ThCl band that is overlapped by P lines from the nearby ThO band at 21928 cm^{-1}. The feature marked (*b*), is the $Th^{35}Cl$ [21.7]1.5 $v = 1 - X(1)1.5\ v = 0$ transition, while (*c*) is the $Th^{37}Cl$ band belonging to this same feature.

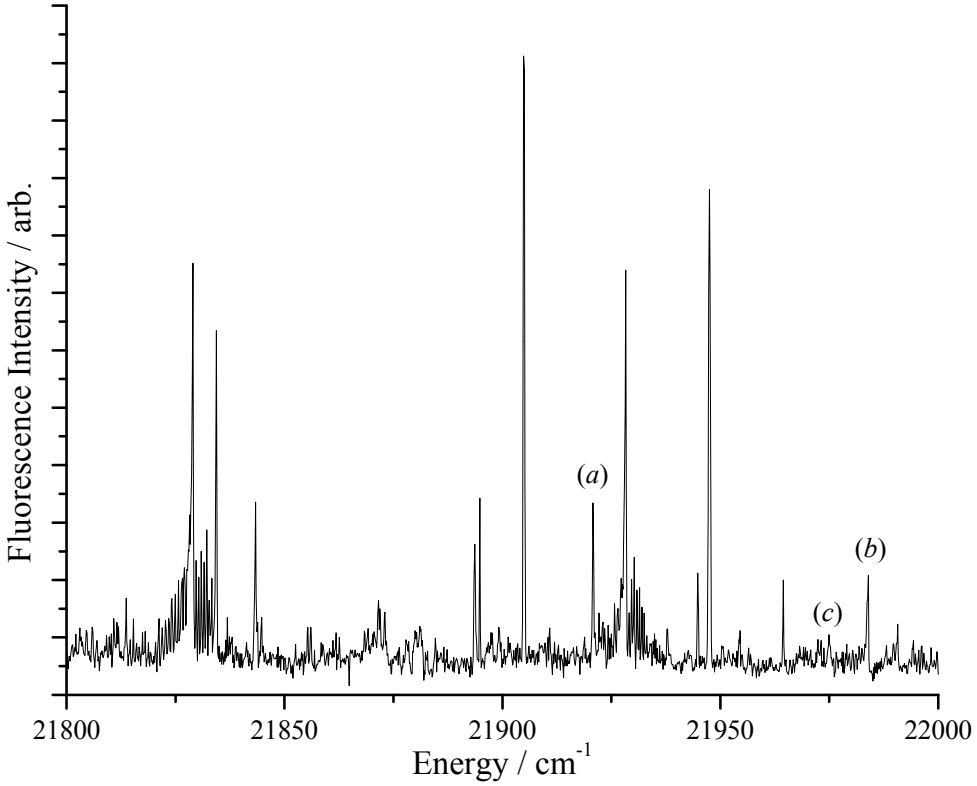

FIGURE 3.2.

Rotationally-resolved LIF spectrum of the [21.7]1.5 $v = 1$ $Th^{35}Cl$ feature obtained after insertion of an intracavity etalon to improve the laser linewidth to 0.06 cm^{-1}. The upward-going trace is experimental, the downward-going trace is a simulation with a rotational temperature of 8 K. The P, Q, and R branches are indicated, as well as the lowest P and R lines. The CASPT2 prediction for the ground state rotation constant is in good agreement with the constant extracted from the simulation fit to experiment.

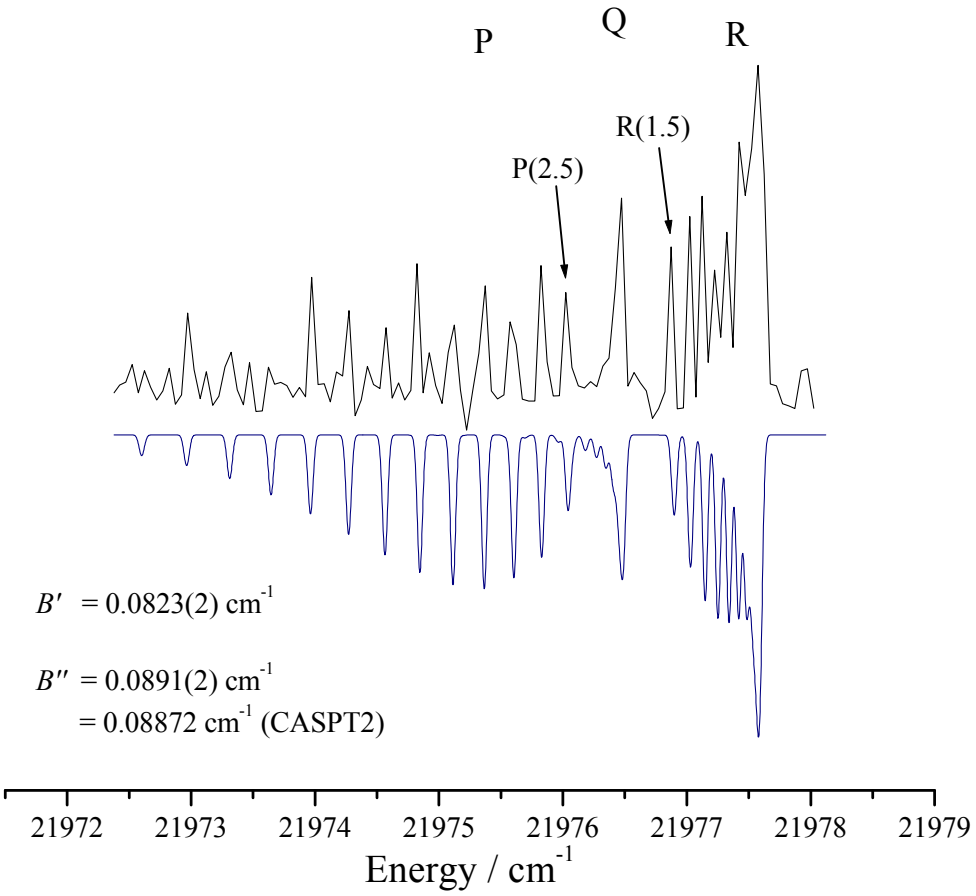

FIGURE 3.3.

Dispersed fluorescence spectrum recorded from the R band-head of the {23.5}0.5 – X(1)1.5 transition. There are some features, marked by an asterisk, from partial overlap of a nearby ThO band. A ground state vibrational progression up to $v = 11$ is observed, with three excited states labeled according to the CASPT2 predictions.

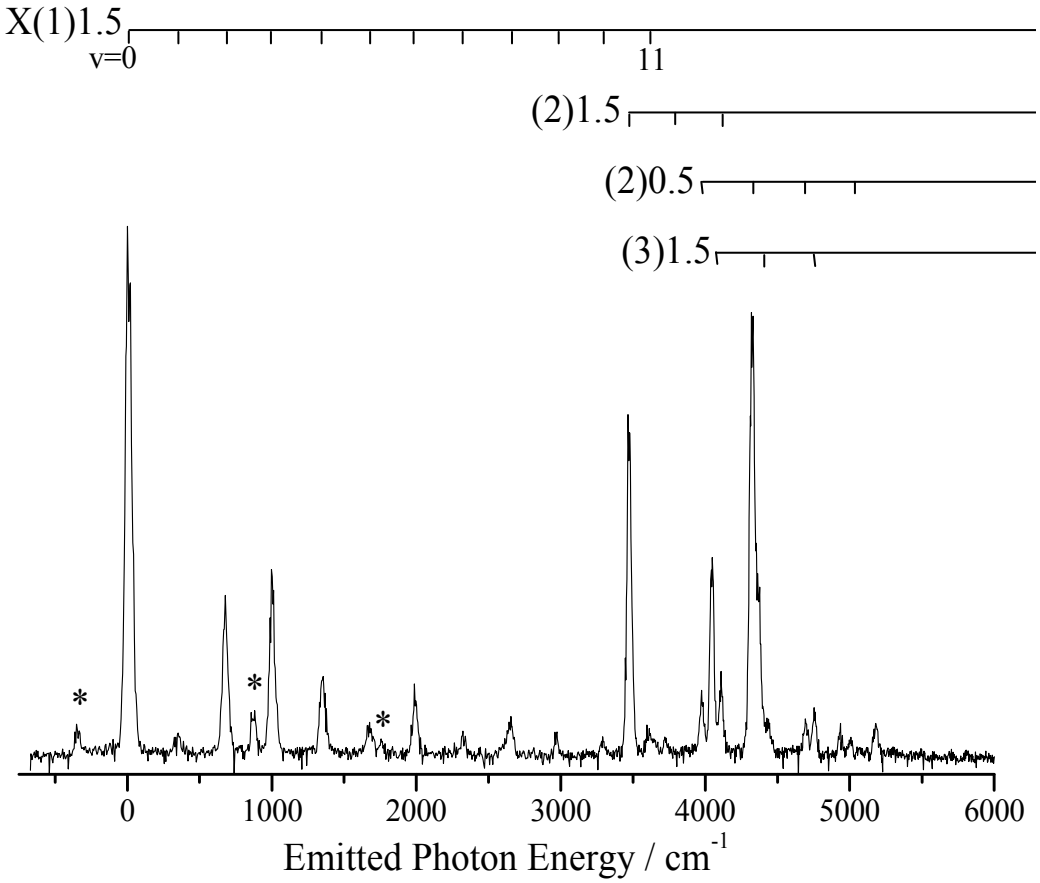

FIGURE 3.4.

Photoionization efficiency spectrum obtained by tuning the ionization laser to lower energies while the first laser pumped the R band-head of the [21.7]1.5 $v = 1$ – X(1)1.5 $v = 0$ transition. Dashed lines indicate the linear fits to the baseline portion of the spectrum and to the slope of the ionization onset feature, with the intersection chosen as the initial estimate of the IP, 51718.2(100) cm^{-1}. The total energy has been adjusted to account for the electric field between the repeller and extractor plates of the TOFMS.

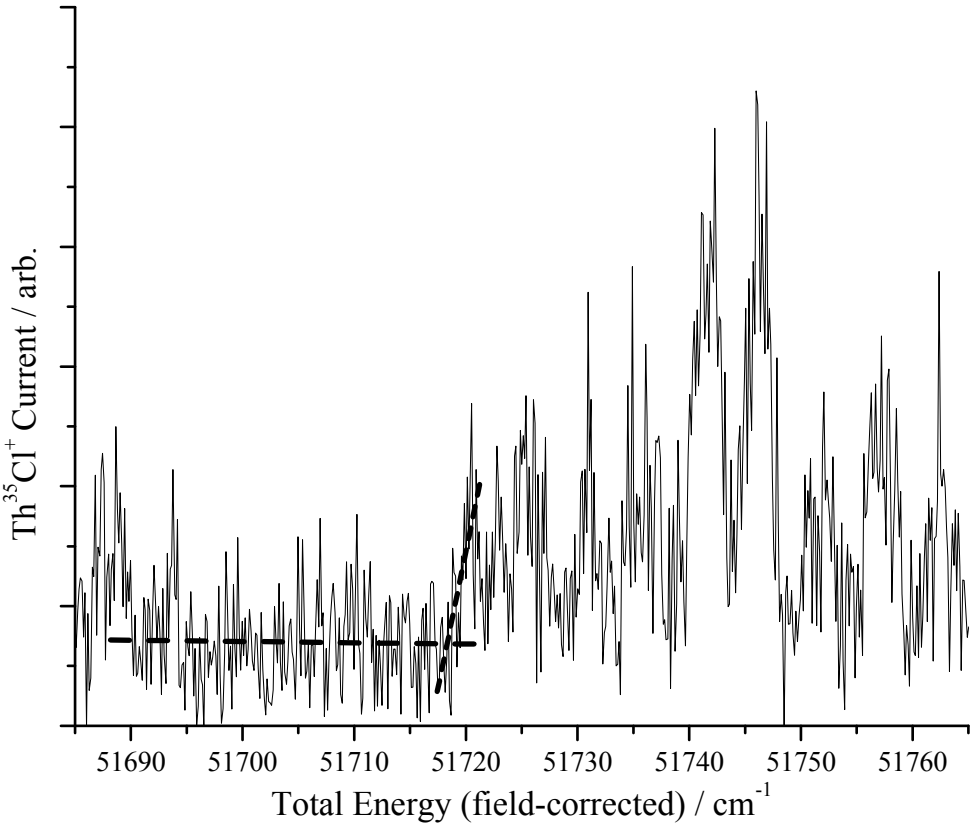

FIGURE 3.5.

$Th^{35}Cl^{+}$ bands observed via PFI-ZEKE up to 1000 cm^{-1} above the lowest energy feature. The IP_{ThCl} = 51744(3) cm^{-1} (shown as 0 cm^{-1} in the spectrum) is tentative; the term energies of the subsequent bands are set relative to that feature. See Table 3.5 for band energies and text for details.

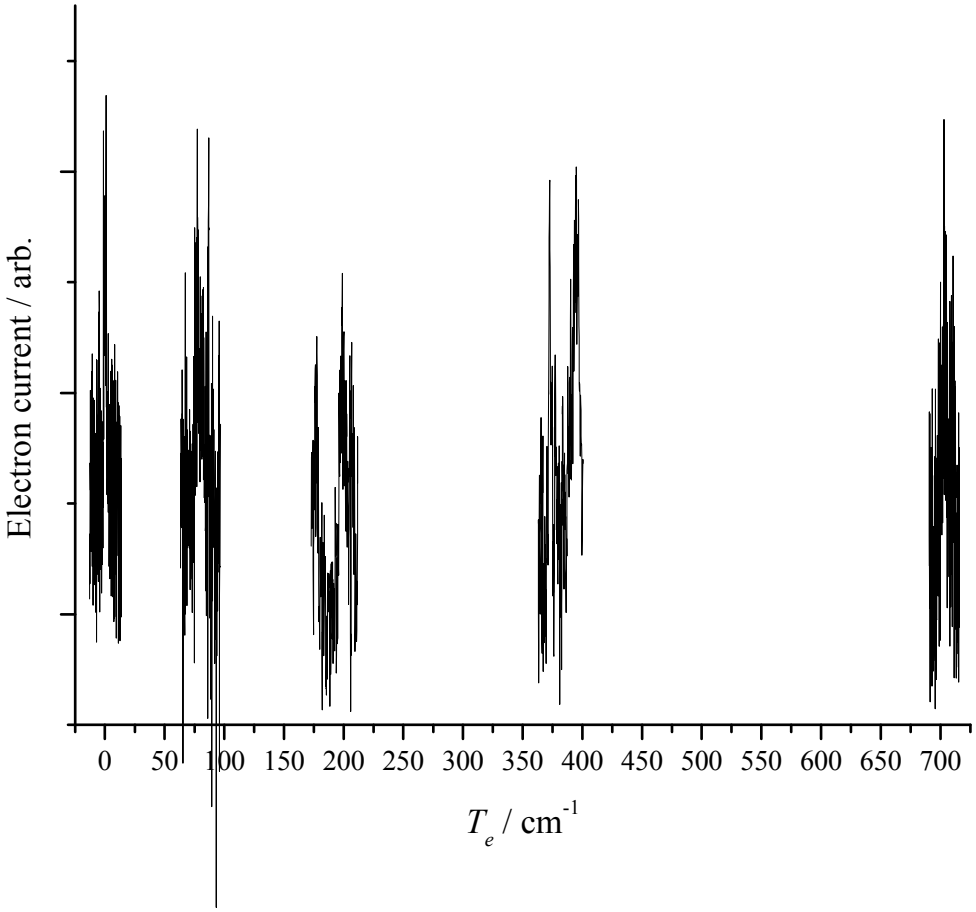

Chapter 4

Evaluation of the Exothermicity of the Chemi-ionization Reaction Sm + O → $SmO^+ + e^-$

4.1. INTRODUCTION

There has long been an interest in small scale chemical releases to alter the electron density in local regions of the atmosphere.[1] Recently, the Air Force Research Laboratory (AFRL) has conducted two releases of samarium from sounding rockets intended to artificially generate local electron density and conductivity enhancements in order to provide regional suppression of naturally occurring ionospheric scintillation. The chemistry involved starts with the reaction of the released Sm and ambient atomic oxygen to create ionization,

$$Sm + O \rightarrow SmO^+ + e^- \quad (1)$$

The experiments took place at the Reagan Test Site, Kwajalein Atoll in May 2013. Two sounding rockets were launched that reached altitudes of 170 km and 180 km.[2,3] Each rocket had canisters with 5 kg of samarium vapor released by heating with a thermite

explosion as developed by General Sciences Inc. Creation of the cloud was confirmed by observations from a host of ground-based sensors from five locations on four separate atolls in the Republic of the Marshall Islands. Models based on laboratory data of the chemi-ionization, or associative ionization, reaction (1) and subsequent processes predicted a higher level of ionization than was observed. The present work aims to help understand these unexpected results by reexamining the thermochemistry of reaction (1).

A small number of elements, primarily a subset of the lanthanides and actinides, form monoxides having ionization energies (IE) smaller than their bond dissociation enthalpies (BDEs).[4] This property dictates that reactions analogous to (1) are exothermic and may proceed efficiently at thermal energies. In turn, this places those monoxide cations into the exclusive group of polyatomic cations that are stable to dissociative recombination, i.e., the reverse of reaction (1). Any of the species in this group are potentially effective at producing elevated electron densities at altitudes above ~100 km, where atomic oxygen is a dominant atmospheric species.

With interest in the atmospheric effects of chemistry of this type, several experiments were undertaken in the 1970s to evaluate both the kinetics and the thermochemistry of these systems. Fite *et al.* measured cross-sections of chemi-ionization processes by crossing beams of several atomic metals with beams of neutral O, O_2, and O_3 and monitoring the ionized products using a quadrupole mass spectrometer.[5-9] These results, summarized in a technical report[10] to the Air Force Geophysics Laboratory (now AFRL), indicated cross sections for reactions analogous to (1) of between ~10^{-17} and 10^{-15} cm^2, equivalent to room temperature rate constants of ~10^{-12} to 10^{-10} cm^3 s^{-1}.

Although the reported kinetics of Sm + O were slow, lying towards the lower end of those ranges, Sm was chosen for chemical release experiments because of its relatively high vapor pressure and the subsequently expected ease of vaporizing the metal during the release. Interestingly, the magnitude of the reported rate constants for these chemi-ionization reactions is highly correlated with the exothermicity of the reactions.

Thermochemical cycles demand that the exothermicity of reaction (1) is equal to either of two differences: (1) as stated above, the IE and the BDE of SmO and (2) the BDE of SmO^+ and the IE of Sm. This is illustrated in Figure 4.1, which shows a schematic representation of these energy levels. Of these four quantities, the IE of Sm is by far the most well-determined, evaluated as IE(Sm)=5.6437 ± 0.0006 eV.[11,12] The ionization energy of SmO has been reported as IE(SmO) = 5.55 ± 0.1 eV, derived from linear extrapolation of the ionization efficiency curve of SmO^+ produced by electron impact of SmO at 2300 K.[13] This value is in agreement with a coarse determination made from the appearance energy of SmO^+ (here, the value cited of 5.5 eV also equaled the value measured for atomic Sm, indicating it is likely too low).[14] The earliest work concerning the 0 K BDE of SmO was reported by Amesetal., [15] who found a value of 5.94 ± 0.04 eV from the vaporization of Sm_2O_3 and a third-law determination of 6.31 eV from an equilibrium of Sm-YO. Brewer and Rosenblatt later reevaluated these data reporting BDEs of 5.72 and 5.81 eV, respectively, assigning 5.77 ± 0.35 eV as the recommended value,[16] a value also adopted by Ackermann, Rauh, and Thorn.[13] Subsequently, Hildenbrand reported the SmO BDE as D_0(Sm-O) = 5.90 ± 0.09 eV, derived from measured equilibrium constants of the exchange reactions of Sm with several metal

oxides (i.e., the third-law method).[14] (Specific values obtained were 5.86 ± 0.12 eV with AlO, 5.91 ± 0.13 eV with TiO, and 5.94 ± 0.15 eV with EuO.) This value is quite close to a lower limit of 5.88 ± 0.03 eV established by measurement of the chemiluminescent spectrum of the reaction of Sm with NO_2.[17] In a subsequent review utilizing updated thermochemistry, Pedley and Marshall suggested a value of D_0(Sm-O) = 5.88 ± 0.17 eV [18] on the basis of data from Hildenbrand,[14] Ames *et al*.,[15] and Dickson and Zare.[17] In another review, Chandrasekharaiah and Gingerich[19] adopted the value of Hildenbrand and adjusted the uncertainty, 5.90 ± 0.10 eV, a value later cited by Gibson.[20] The GIANT (Gas-phase Ion And Neutral Thermochemistry) tables' compilation adopts the 298 K heat of formation for SmO suggested by Pedley and Marshall but adjusts the heat of formation to 0 K differently such that D_0(Sm-O) = 6.04 ± 0.13 eV is calculated from the 0 K heats of formation provided.[21] More recently, Konings *et al*. relied primarily on the Sm-AlO equilibrium values from Hildenbrand[14] (ignoring the Sm-TiO and Sm-EuO equilibria for reasons left unstated) and assigned the SmO BDE as D_0(Sm-O) = 5.76 ± 0.08 eV.[22] Adopting the more inclusive and conservative value from Pedley and Marshall,[18] the difference between the SmO IE and BDE yields $\Delta_r H^o_0$ for reaction (1) of −0.33 ± 0.20 eV.

For the cationic species, a value of $D_0(Sm^+\text{-O})$ = 5.97 ± 0.20 eV may be derived from the adopted literature values above. This is essentially equivalent to the value cited by Murad and Hildenbrand, 5.98 ± 0.13 eV, who used an earlier spectroscopic value for IE(Sm) = 5.63 eV. 23 Ackermann *et al*.[13] cited 5.80 ± 0.10 eV using their IE values for both Sm (5.58 eV) and SmO along with the Brewer and Rosenblatt neutral BDE. Chandrasekharaiah and Gingerich[19] (whose value is also adopted by Gibson)[20] reported

$D_0(Sm^+\text{-}O) = 5.86 \pm 0.16$ eV, but the 0 K heats of formation for Sm, Sm^+, SmO, and SmO^+ provided in this reference indicate IE(Sm) = 3.49 eV and IE(SmO) = 3.55 eV, which are clearly incorrect. (Neither the specific IE values used nor their origins are provided in this work.) Finally, heats of formation given in the GIANT tables suggest $D_0(Sm^+\text{-}O) = 6.14 \pm 0.16$ eV.[12] This literature thermochemistry is largely supported by complete active space self consistent field (CASSCF) *ab initio* calculations, differing significantly only in that the calculations produce a lower BDE for SmO^+ of 5.74 eV.[24] These calculations also indicate $D_0(Sm\text{-}O) = 5.92$ eV, IE(SmO) = 5.58 eV, and IE(Sm) = 5.69 eV. However, the authors do not address the discrepancy that the sum of the theoretically calculated IE(SmO) and BDE of SmO^+ is 0.29 eV less than the sum of the calculated SmO BDE and IE(Sm) (see Fig. 1).

The lower than expected electron density observed in the Sm release experiments raises questions about the seemingly established thermochemistry of the reaction. That the chemi-ionization reaction involving Sm was observed in the experiment by Fite *et al*.[10] strongly suggests that the reaction is exothermic. Later efforts by Cockett *et al*.[25] report an upper bound to the reaction exothermicity of reaction (1) as 0.27 ± 0.08 eV (on the basis of the maximum electron kinetic energy observed) that is in good agreement with the accepted literature value reported above. However, this reported exothermicity may be influenced by excited states as Sm samples were vaporized at 800 K. A population analysis indicates that at 800 K Sm has an average internal electronic energy of 0.07 eV with significant populations at the $^7F_2$ (25%), $^7F_3$ (10%), and $^7F_4$ (3%) levels that have energies lying 0.10, 0.18, and 0.28 eV, respectively, above the ground $^7F_0$

level.[26] As discussed below, the magnitude of the exothermicity could have large effects on the efficiency of the chemical release efforts. Here, the exothermicity of the title reaction is re-evaluated through two independent determinations: measurement of $D_0(Sm^+\text{-}O)$ and measurement of IE(SmO). Additionally, the thermal reactivity of Sm^+ and SmO^+ with a number of species is investigated.

4.2. EXPERIMENTAL AND THEORETICAL METHODS

4.2.1. SIFT Apparatus

The Air Force Research Laboratory's variable temperature selected ion flow tube instrument (VT-SIFT) has been described in detail elsewhere,[27] and for these experiments was used by Sean G. Ard, Joshua J. Melko, Nicholas S. Shuman, and Albert A. Viggiano. Sm^+ and SmO^+ ions are created in a newly implemented electrospray ion source[28]. An approximately 1mM solution of samarium iodide in methanol flows at 150 μL h^{-1} through a fused silica capillary biased to approximately 4000 V in open atmosphere. The spray enters vacuum through a dielectric capillary heated to 100 °C for increased desolvation. The ions formed are focused by an ion funnel and lenses, then transported by a rectilinear ion guide and ion bender to a quadrupole mass filter where either the Sm^+ or SmO^+ ions are isolated. The ions are focused before introduction to a laminar flow tube via a Venturi inlet, where 10^4 to 10^5 collisions with a He buffer gas act to thermalize the ions and carry them downstream. Operating pressures of 0.4 Torr of He are typical, however the

pressure in the flow tube was varied up to 0.8 Torr for several of the termolecular reactions observed. The neutral reagent (O_2, N_2O, NO_2, NO, CO_2, SO_2) is added 59 cm upstream of the end of the flow tube, with typical reaction times on the order of 4 ms, dependent upon flow tube pressure and temperature. After traveling the length of the flow tube, the core of the flow is sampled through a truncated nosecone with a 2 mm aperture. The remainder of the flow is pumped away by a roots pump through a throttled gate valve that acts to maintain the desired pressure within the flow tube. After the nosecone, the primary ions and product ions are guided by a lens stack to a quadrupole mass filter for analysis, and are subsequently detected using an electron multiplier operated in counting mode. Rate constants are derived by monitoring the decay of the primary ion as a function of the neutral reagent flow. Measurements were made from approximately 300 K to 650 K and temperature dependences of the rate coefficients were determined. Errors in the rate coefficients are estimated to be ±25% absolute and ±15% relative to each other.[27]

4.2.2. Guided Ion Beam Tandem Mass Spectrometer

The guided ion beam tandem mass spectrometer (GIBMS) at the University of Utah used in these studies has been described previously,[29] and was used by Richard M. Cox, Jungsoo Kim, and Peter Armentrout for the following experiments. Briefly, Sm^+ and SmO^+ ions are created in a direct current discharge flow tube (DC/FT) source described in detail elsewhere.[30] Sm^+ ions are created when Ar ionized by a dc electric

field (1.2 – 1.4 kV) collides with a cathode holding the samarium foil sample. Ions typically thermalize under ~10^5 collisions with the He/Ar carrier gasses in a 9:1 mixture in a 1 m flow tube held at a total pressure of 0.5 Torr. To further ensure thermalization, O_2 or SO_2 gas is introduced to the flow tube 15 cm downstream from the ion source to quench any excited state ions. SmO^+ ions are created by introducing O_2 gas through the same inlet. Previous work in our laboratory has indicated that the DC/FT source produces ions with an internal electronic energy of 300 – 1100 K.[31-35] At 300 K, 67.8% of Sm^+ ions are found in the $^8F_{1/2}$ ground level. At 1100 K, 21.1% of ions are found in the $^8F_{1/2}$ ground level. Conservatively we estimate that the average internal temperature of the Sm^+ ions is 700 ± 400 K, for an average internal energy of 0.06 ± 0.05 eV that is incorporated in all reported BDEs. The internal energies of SmO^+ ions are presumed to be at 300 K.

Ions are extracted from the source, focused through a magnetic momentum analyzer where the reactant ion is mass selected. To ensure efficient mass separation between the several abundant isotopes of Sm, the second most abundant and heaviest isotope, ^{154}Sm (22.7% abundance), was chosen because it is separated from the next closest isotope by 2 amu. These ions are subsequently decelerated to a well-defined kinetic energy and passed into a radiofrequency (rf) octopole ion beam guide[36-38] where the ions are trapped radially. The octopole passes through a static gas cell that contains the neutral reactant gas at pressures of 0.10 - 0.40 mTorr. Pressures are low to ensure that the probability of more than one collision occurring between the reactants is small, and it was verified that the measured cross sections reported below do not vary with neutral reactant pressure. After the collision cell, remaining reactant and product ions drift to the

end of the octopole, are focused through a quadrupole mass filter for mass analysis, and counted using a Daly detector.[39] Reaction cross sections are calculated, as described previously, from product ion intensities relative to reactant ion intensities after correcting for ion intensities with the neutral gas no longer directed to the gas cell. Uncertainties in the measured absolute cross sections are estimated to be ±20 %, with relative uncertainties of ±5%.

Laboratory ion energies (lab) are converted to the center-of-mass frame (CM) using the relationship $E_{CM} = E_{lab}\, m/(m + M)$ where m and M are the masses of the neutral and ionic reactants, respectively. The absolute zero of energy and the full width at half-maximum (FWHM) of the ion beam are determined by using the octopole guide as a retarding potential analyzer.[37] Typical FWHMs of the energy distribution for these experiments were 0.4 - 0.6 eV (lab). Uncertainties in the absolute energy scale are 0.1 eV (lab). All energies reported below are in the CM frame.

4.2.3. GIBMS Data Analysis

The kinetic energy dependence of endothermic reactions observed using the GIBMS is modeled using Eq. (2),[38,40,41]

$$\sigma(E) = \sigma_0 \sum g_i \frac{(E + E_i - E_0)^n}{E} \qquad (2)$$

where σ_0 is an energy-independent scaling factor, E is the relative kinetic energy of the reactants, E_i is the internal energy of the reactants' electronic, vibrational, and rotational states having populations g_i ($\Sigma g_i = 1$), n is an adjustable parameter, and E_0 is the 0 K

reaction threshold. Before comparison to the data, Eq. (2) is convoluted over the kinetic energy distributions of the reactants.[37,42,43] The σ_0, n, and E_0 parameters are then optimized using a nonlinear least-squares method to best reproduce the experimental cross section. Uncertainties in E_0 are calculated from the threshold values for several independent data sets over a range of n values combined with the absolute uncertainties in the kinetic energy scale and internal energies of reactant ions. Calculated thresholds are then used to determine bond dissociation energies (BDEs), $D_0(Sm^+\text{-}R)$, using the relationship:

$$D_0(Sm^+ - R) = D_0(L - R) - E_0 \qquad (3)$$

This equation assumes that there are no barriers in excess of the endothermicity of the reaction. When evidence of a barrier exists, Eq. (3) provides a lower limit to the true BDE. Neutral BDEs, D_0(L-R), were taken from thermochemistry found in the NIST webBook.[44]

4.2.4. REMPI and PFI-ZEKE

The ionization energy (IE) of SmO was determined by means of resonantly enhanced two-photon ionization measurements. The experiments were performed at Emory University using an apparatus that has been described in previous publications[45]. Gas phase SmO was produced using pulsed laser vaporization (1064 nm) of a pure Sm rod (ESPI Metals, natural isotopic composition). The metal vapor was entrained in a pulse of He that contained 1% O_2. The products from the ablation source were cooled by supersonic expansion. The vacuum chamber that housed the ablation source was

equipped for interrogation of the products using laser induced fluorescence (LIF). A pulsed tunable dye laser (Lambda Physik, Scan-Mate Pro, 0.15 cm^{-1} linewidth, 10 ns pulse duration) was used as the excitation source. The absolute wavenumber calibration of this laser was established by recording previously characterized bands of SmO.[46,47]

For photo-ionization measurements, the core of the supersonic expansion was sampled, via a conical skimmer, into a second vacuum chamber. This was equipped with a Wiley-McClaren time-of-flight mass spectrometer and a separate set of microchannel plates for photoelectron detection.[33] The Scan-Mate Pro dye laser was used for the first excitation step. Ionization was achieved using pulses from a second Nd:YAG pumped dye laser (Continuum ND6000, 0.1 cm^{-1} linewidth, 10 ns pulse duration). Wavelengths in the 300-330 nm range were generated by frequency doubling, and the absolute wavenumber calibration for the ND6000 was obtained by using the fundamental to record the B-X spectrum of I_2.[48]

Photo-ionization efficiency (PIE) curves were recorded with the first laser tuned to an established electronic transition of SmO, and the wavelength of the second laser was swept to locate the ionization threshold. For these scans, the mass spectrometer was used to monitor the signals resulting from the most abundant isotopologues ($^{152}SmO^+$ and $^{154}SmO^+$). The threshold energy was then refined by means of pulsed-field ionization zero kinetic energy (PFI-ZEKE) photoelectron spectroscopy. An ionizing field of 0.36 V/cm was used, and this was applied 2 ms after the second laser pulse.

4.3. EXPERIMENTAL RESULTS

4.3.1. SIFT

The reactions of Sm^+ with several common oxygen donating molecules are shown in Table 4.1. The LO bond energy is also shown as a guide to the expected reaction exothermicity, which is simply the difference between the BDEs of LO and SmO^+. The room temperature rate constants for the reactions with N_2O, O_2, and NO_2 agree very well with those in the literature.[49-51] The previously reported formation of SmO^+ from reaction with NO was not observed, which is consistent with similar differences in NO reactivity that have been reported previously for other metals.[52-55] Table 4.1 shows that the efficiencies of these reactions show no clear correlation with the LO bond energy, and therefore the reaction exothermicity. The temperature dependences are typical for exothermic reactions such as these. The reaction with SO_2 serves to provide a rigorous lower limit to the bond strength of SmO^+ of 5.661 ± 0.014 eV, whereas the null reaction with NO serves as a tentative upper limit of 6.500 eV. This limit is tentative because kinetic barriers may be present in the reaction path. Indeed, such barriers seem likely in the null reaction observed for CO_2,[56,57] which has a lower LO bond energy than SO_2 such that the $Sm^+ + CO_2 \rightarrow SmO^+ + CO$ reaction must be exothermic. GIBMS experiments verify the presence of these kinetic barriers in both cases.[57]

The lower limit of 5.661 ± 0.014 eV for $D_0(SmO^+)$ combined with IE(Sm) indicates that reaction (1) is exothermic by at least 0.017 ± 0.014 eV, and therefore that the reverse dissociative recombination reaction is endothermic. Given this conclusion, we considered the possibility of continued oxidation of the SmO^+ cation. Reactions of SmO^+ with each of the oxygen donating neutrals, other than NO, were then studied and are shown in Table 4.2. In all cases, these reactions led to only cluster formation, with no bimolecular reactions observed. Termolecular rate constants are derived from measured effective two-body rate constants over pressure ranges of 0.4 – 2 Torr; however, the likely small bond energies of these clusters suggest thermal or electric field excitation may result in cluster dissociation prior to detection, resulting in potentially large error. As expected, clustering to each of the triatomic species was significantly faster than for O_2, which was too slow for a rate to be established. Clustering with SO_2 and NO_2 was an order of magnitude faster than for N_2O and CO_2 implying larger bond energies for these species.

In regards to the lower than expected electron density observed by the recent chemical release, the SIFT work has several important findings. The reaction of Sm^+ with SO_2 firmly establishes that reaction (1) is exothermic. A more precise magnitude of this exothermicity is pursued using the GIBMS and REMPI studies reported below. The reaction of Sm^+ with O_2 shows that any Sm^+ formed by either thermal- or photo-ionization will quickly react to form SmO^+, as opposed to species where dissociative recombination may play a larger role in limiting the electron density. Furthermore, it was found that SmO^+ will not further oxidize, which would result in electron sinks via

dissociative recombination of the larger product ions. The only observed reactions with SmO^+, clustering, will have little to no impact for these results given the low atmospheric densities at these altitudes.

4.3.2. GIBMS

4.3.2.1. $Sm^+ + LO$ (L = O, SO, C)

A key feature of the GIBMS is the ability to study the kinetic energy dependence of a reaction over a large range of energies. This feature allows for the direct determination of a BDE from an endothermic process. Given the scope of this project, reactions of Sm^+ with N_2O and NO_2 were not studied using GIBMS because the BDE of these O donors are much smaller than the expected SmO^+ BDE (Table 4.1), and therefore, is not expected to yield much additional information beyond the SIFT experiments. Reactions of Sm^+ with CO_2 and NO were studied using GIBMS, and the failure of both reactions to yield SmO^+ at thermal energies found in the SIFT studies was confirmed (Table 4.1). In both cases, these reactions have interesting kinetic features that are beyond the scope of this text and will be published elsewhere.[57]

The kinetic energy dependent cross sections from the reaction of Sm^+ and O_2 are found in Figure 4.2. In this reaction, two products were observed according to reactions:

$$Sm^+ + O_2 \rightarrow SmO^+ + O \quad (4)$$

$$Sm^+ + 2O_2 \rightarrow SmO_2^+ + 2O \quad (5)$$

The cross section of SmO^+ from reaction (4) is consistent with an exothermic and barrierless process as the cross section declines with increasing energy. Reaction (4) is observed to react with unit efficiency, $k/k_{col} = 1.0 \pm 0.2$, where k_{col} is defined as the Su-Chesnavich semi-classical trajectory rate constant.[58] The cross section of reaction (5) is observed to be dependent on the pressure of the O_2 reactant partner, indicating that it is the product of sequential reactions, i.e., $SmO^+ + O_2$. The observation that this reaction exhibits a substantial barrier is consistent with the failure of the SIFT studies to observe this reaction at thermal energies.

The efficiency of reaction (4) observed using GIBMS is significantly larger than that observed in SIFT experiments, where the present work observes an efficiency of $k/k_{col} = 0.49 \pm 0.15$ and previous work by Koyanagi and Bohme[50] observed an efficiency of $k/k_{col} = 0.48 \pm 0.14$. To ensure that the efficiency of reaction (4) observed using GIBMS is not a result of excited state ions, the reaction was repeated while leaking O_2 into the source flow tube region. This approach selectively removes ions with excessive internal energy; however, no effect on the overall efficiency of reaction (4) was observed. We therefore have no explanation for this discrepancy, the cause of which may be interesting, but fortunately is of no consequence to the primary purpose of this paper, i.e., the thermodynamics of reaction (1).

The kinetic energy dependent cross sections from the reaction of Sm^+ and SO_2 is found in Figure 4.3 and are in accord with the SIFT results. At all energies, the dominant product is SmO^+ formed according to reaction:

$$Sm^+ + SO_2 \rightarrow SmO^+ + SO \qquad (6)$$

The SmO^+ cross section declines with an energy dependence similar to the Su-Chesnavich cross section until ~ 1 eV where the cross section levels off. A secondary feature with an apparent threshold near 1.5 eV and a peak at 5.5 eV is also observed. The energy of the peak corresponds nicely to D_0(OS-O) = 5.66 eV, indicating that the SmO^+ cross section declines because the $Sm^+ + O + SO$ channel becomes available at this energy. The efficiency of reaction (6) is $k/k_{col} = 0.22 \pm 0.04$, which is similar to the 0.29 ± 0.09 observed in the SIFT experiments here.

Samarium ions react with SO_2 to form additional products according to reactions:

$$Sm^+ + SO_2 \rightarrow SmO_2^+ \quad (7)$$

$$\rightarrow SmSO^+ + O \quad (8)$$

$$\rightarrow SmO_2^+ + S \quad (9)$$

Reaction (7) is observed at the lowest energies with a cross section that is consistent with an exothermic, barrierless reaction. Furthermore, no pressure dependence for the cross section was observed, indicating that this species is not collisionally stabilized. The observation of the $SmSO_2^+$ adduct as a long lived intermediate is likely a result of the large dipole moment (1.63 D)[44] and polarizability (3.22 $Å^3$)[44] of the SO_2 gas. The threshold of reaction (8) has an apparent onset near 3.5 eV and peaks at ~5.7 eV, again corresponding to D_0(OS-O). Reaction (9) has an apparent threshold of ~4.5 eV and peaks near ~6 eV. A secondary feature with an apparent onset near 8 eV is also observed. The cross section from reaction (9) is identified as SmO_2^+ (rather than the isobaric $^{154}Sm^{32}S^+$) because no reaction product with a mass consistent with $^{154}Sm^{34}S^+$ was observed. In addition, the SmO_2^+ cross section showed no discernable pressure dependence indicating

that this product is formed in a single ion-molecule interaction rather than a sequential reaction such as reaction (5). Finally, the apparent threshold is similar to the expected threshold for reaction (9) given the thermochemistry reported below.

The kinetic energy dependent cross sections from the reaction of Sm^+ and CO are found in Figure 4.4. SmO^+ and SmC^+ were observed according to reactions:

$$Sm^+ + CO \rightarrow SmO^+ + C \quad (10)$$

$$Sm^+ + CO \rightarrow SmC^+ + O \quad (11)$$

The cross section for reaction (10) has an apparent threshold of ~5.5 eV and rises with increasing energy. The cross section peaks near the BDE of CO, 11.109 ± 0.005 eV,[44] where enough energy is available for SmO^+ to dissociate to Sm^+ and O. Reaction (11) has an apparent threshold near 8.5 eV and rises with increasing energy until peaking again near $D_0(CO)$. Note that the apparent threshold is consistent with a BDE for SmO^+ in the vicinity of 5.6 eV, close to that expected from the literature thermochemistry. A precise determination of this threshold and the resultant $D_0(SmO^+)$ is discussed below.

4.3.2.2. $SmO^+ + Xe/O_2$

Reactions of SmO^+ with Xe and O_2 were also performed. The cross section from the collision-induced dissociation (CID) reaction,

$$SmO^+ + Xe \rightarrow Sm^+ + O + Xe \quad (12)$$

is found in Figure 4.5. This reaction has an apparent threshold of ~ 6 eV, again roughly consistent with the literature thermochemistry. Although not obvious from the

logarithmic scale of Figure 4.5, the CID cross section rises rather slowly and reaches a relatively small magnitude of only 0.15×10^{-16} cm^2 at 15 eV, consistent with the need to break a relatively strong diatomic bond.

The kinetic energy dependent cross sections for the reaction of SmO^+ and O_2 are found in Figure 4.6. Products are observed according to reactions:

$$SmO^+ + O_2 \rightarrow SmO_2^+ + O \quad (13)$$

$$SmO^+ + O_2 \rightarrow Sm^+ + O_2 + O \quad (14)$$

Reaction (13) has an apparent threshold of 3.5 eV and rises in intensity until ~ 6 eV where it begins to decline. Reaction (14) has an apparent threshold similar to that observed for reaction (12) substantiating the CID mechanism listed in reaction (14), as opposed to concomitant formation of ozone, discussed further below. Notably, this CID cross section rises more rapidly than that of reaction (12), which suggests that determination of the threshold energy from this reaction will be more reliable.

4.3.3. REMPI and PFI-ZEKE

LIF spectra for SmO were recorded to locate a suitable transition for the first excitation step and to characterize the internal temperature of the jet-cooled ablation products. The origin band of the [16.6]1-X0$^-$ transition proved to be suitable for this purpose. Because of the large number of Sm isotopes, the spectrum was not rotationally resolved. However, the P/Q/R branch structure was easily recognizable, as can be seen in Fig. 4.7. The lower trace in Fig. 4.7 is a simulation of the rotational band contour,

performed using the molecular constants for ^{152}SmO and ^{154}SmO from Bujin and Linton[37] the program PGOPHER,[59] and a rotational temperature of about 10 K. Note that the difference between the simulation and the LIF spectrum in the region between the P- and Q-branch contours is a result of neglecting the less abundant isotopes of Sm, for which spectroscopic constants were not reported (^{152}Sm and ^{154}Sm have natural abundances of 26.75% and 22.75%, respectively) At a rotational temperature of 10 K, the Q-branch was heavily overlapped, and by far the most intense part of the band contour. Consequently, the photo-ionization measurement was carried out with the first laser tuned to the maximum of the Q-branch (16 585.5 cm^{-1}).

The ablation products were further characterized by recording the mass spectrum. To probe the widest range of species, one color non-resonant two-photon excitation at 310 nm was employed. The resulting mass spectrum contained only the Sm^+ and SmO^+ signals, with relative Sm isotopic peak intensities that were consistent with the natural abundances. Larger molecular species did not appear to be formed under the jet expansion conditions used.

A two-color PIE scan is presented in Fig. 4.8. Here, it can be seen that the threshold for SmO^+ ion production was located at a two-photon energy of 46 226 ± 10 cm^{-1}. This trace was recorded with the ionization lasers positioned between the repeller plate and the draw-out grid of the mass spectrometer, where the local field was F = 250 V cm $^{-1}$. This field depresses the IE by an energy of $\Delta E(cm^{-1}) = 6.12\sqrt{(F(V\ cm^{-1}))}$, which is 97 cm^{-1} in this instance. Correcting for this effect yields an initial estimate for the IE of SmO of 46 323 ± 10 cm^{-1}. Care was needed to ensure that the threshold observed was a

two-color resonance, as features arising from two-photon excitation by the second laser alone were commonly encountered. The density of electronically excited states of SmO in the near uv spectral range is high, which is easily appreciated given that the ground state has the electronic configuration $Sm^{2+}(4f^{5}6s)O^{2-}$. The signal-to-noise ratios of the PIE trace in Fig. 4.8 and the PFI-ZEKE scan shown in Fig. 4.9 (see below) were low because the laser intensities were attenuated to suppress one-color multi-photon processes.

A PFI-ZEKE spectrum was recorded with the first laser tuned to the Q-branch feature noted above. The most populated rotational level within this feature was J=3; so, levels of the intermediate state with J=1-4 were significantly populated. Fig. 4.9 shows the PFI-ZEKE spectrum. The PFI-ZEKE measurement relies on the fact that the high-n Rydberg states that are just below the ionization threshold are long-lived. SmO was excited to the Rydberg states under field-free conditions. After a delay of 2 ms, a 0.36 V cm^{-1} field was applied to remove electrons from the Rydberg states and accelerate them to the microchannel plate detector. The time delay is used to suppress the signal from any process that causes direct ionization. Hence, the blue-edge of the PFI-ZEKE feature corresponds to the convergence limit of the Rydberg series and thereby defines the IE. It is helpful to contrast the fact that the PFI-ZEKE scan shows the energy levels immediately below the ionization threshold, whereas the PIE curve shows the continuum and auto-ionizing states above the threshold. After local field corrections, it is expected that the red threshold of the PIE curve and the blue-edge of the PFI-ZEKE spectrum will coincide with the IE. The data shown in Fig. 4.9 yielded an IE of 46 318 ± 5 cm^{-1} (5.7427

± 0.0006 eV), in good agreement with the less accurate value from the PIE scan.

Tests were conducted to ensure that the observed PFI-ZEKE threshold corresponded to the intended sequential excitation process that passed through the [16.6]1,v′=0 state. The peak in Fig. 4.9 was only observed when the first laser was tuned to the more intense regions of the [16.6]1-X0$^-$ rotational contour.

4.4. THERMOCHEMICAL RESULTS

4.4.1. SmO^+

In SIFT-MS experiments, SmO^+ was observed in reactions with N_2O, NO_2, O_2 and SO_2, but was not observed in reactions with CO_2 and NO. The results of all these reactions with exception of CO_2 are consistent with the literature BDE for SmO^+ of 5.97 ± 0.20 eV. Previous SIFT-MS experiments observed the formation of $Sm^+(CO_2)_{1-3}$ indicating that the anomalous results from the CO_2 reaction can be attributed to a barrier to the reaction in excess of thermal energies.[56] In GIBMS experiments that will be reported elsewhere, we confirm the presence of this barrier.[57] The results of the SIFT-MS experiments indicate that $D_0(Sm^+\text{-}O) \geq D_0(OS\text{-}O) = 5.661 \pm 0.014$ eV and probably that $D_0(Sm^+\text{-}O) < D_0(N\text{-}O) = 6.500 \pm 0.004$ eV.

In GIBMS experiments, SmO^+ was observed to form exothermically in reactions (4) and (6) in direct agreement with the SIFT-MS experiments. Modeling of the SmO^+ cross section for reaction (10) using Eq. (2) indicates a threshold, $E_0 = 5.49 \pm 0.12$ eV.

Parameters used in Eq. (2) for this and all other modelled reactions can be found in Table 4.3. Using Eq. (3) and D_0(C-O) = 11.109 ± 0.005 eV, this yields $D_0(Sm^+\text{-}O)$ = 5.62 ± 0.15 eV. This value is consistent with the results from reaction (6) and within experimental uncertainty of the value reported above.

Additionally, $D_0(Sm^+\text{-}O)$ was measured in CID reactions with Xe and O_2 used as the collision gas with thresholds of 5.67 ± 0.17 eV and 5.78 ± 0.09 eV, respectively, which in both cases are direct measures of the desired BDE. In this instance, the slow onset in the cross section for reaction (12) leads to the larger uncertainty. By contrast, the sharp rise in the threshold for the cross section of reaction (14) suggests that the value $D_0(Sm^+\text{-}O)$ = 5.78 ± 0.09 eV is more reliable. The agreement in the threshold energies for these two CID processes also provides support that reaction (14) rather than (15) is responsible for the Sm^+ product,

$$SmO^+ + O_2 \rightarrow Sm^+ + O_3 \qquad (15)$$

The threshold for reaction (15) is lower than that for (14) by $D_0(O_2\text{-}O)$ = 1.05 ± 0.02 eV,[44] which is inconsistent with the results from modeling with Eq. (2) as listed in Table 4.3. In some cases, the threshold measured in CID reactions of strongly bound molecules like SmO^+ is conservatively reported as an upper limit to the true BDE because of inefficiencies in the energy transfer needed to dissociate the reactant.[60-62] In the present case, however, the excellent agreement between BDEs derived from the CID values, from reaction (10), and the literature suggest that this is a good measure of the SmO^+ BDE.

The $D_0(Sm^+\text{-}O)$ values measured from reactions (10), 5.62 ± 0.15 eV, (13), 5.67 ± 0.16 eV, and (14), 5.78 ± 0.09 eV are within experimental uncertainty of each other. A

weighted average of all three values yields $D_0(Sm^+-O) = 5.72_5 \pm 0.07$ eV (one standard deviation). This value agrees with the literature values within experimental uncertainties and is in good agreement with theoretical work, $D_0(Sm^+-O) = 5.74$ eV.[24] Combined with IE(Sm) = 5.6437 eV, this BDE indicates that the chemi-ionization reaction (1) is exothermic by only 0.08 ± 0.07 eV, substantially less than originally thought. Combined with IE(SmO) = 5.7427 eV, the SmO^+ BDE indicates that $D_0(SmO) = 5.83 \pm 0.07$ eV, in good agreement with previously recommended experimental values of 5.88 ± 0.17 eV[18] and 5.76 ± 0.08 eV[22] and reasonable agreement with theoretical work, $D_0(Sm^+-O) = 5.92$ eV.[24]

4.4.2. Other Thermochemical Results

In the course of the present work, several other Sm^+ species were observed in the GIBMS studies in addition to SmO^+. With the exception of SmO_2^+, which was previously observed in laser ablation spectroscopic studies in Ar matrices by Wilson and Andrews,[63] these species have not been previously reported. They report a linear structure but no energetics associated with its formation. The formation of SmO_2^+ was observed here in reactions (5), (9), and (13). Reaction (5) is pressure dependent and is a subsequent reaction of SmO^+ formed in reaction with another O_2, i.e., reaction (13), to form SmO_2^+. The threshold measured using Eq. (2) for reaction (13) is $E_0 = 3.98 \pm 0.15$ eV. Using Eq. (3) with $D_0(O-O) = 5.117 \pm 0.001$ eV, this indicates that $D_0(OSm^+-O) = 1.14 \pm 0.15$ eV. When this value is combined with $D_0(Sm^+-O)$ derived above, $D_0(Sm^+-O_2) = 1.76 \pm 0.17$

eV can be determined as follows:

$$D_0(Sm^+ - O_2) = D_0(OSm^+ - O) + D_0(Sm^+ - O) - D_0(O - O) \quad (16)$$

This bond energy can be combined with $D_0(S\text{-}O_2) = 5.897 \pm 0.003$ eV[44] to determine an expected threshold for reaction (9) of $E_0 = 4.14 \pm 0.17$ eV. This is consistent with the apparent threshold for this reaction as observed in Figure 4.3; however, this cross section was not modelled using Eq. (2) because of the low signal intensity.

The BDEs of $SmSO^+$ and SmC^+ were also determined by modelling the cross sections for reactions (8) and (11), respectively, using Eq. (2). For reaction (8), $E_0 = 3.86 \pm 0.08$ eV indicating that $D_0(Sm^+\text{-}SO) = 1.80 \pm 0.08$ eV given $D_0(O\text{-}SO) = 5.661 \pm 0.014$ eV. For reaction (11), $E_0 = 8.95 \pm 0.07$ eV indicating that $D_0(Sm^+\text{-}C) = 2.16 \pm 0.07$ eV given $D_0(C\text{-}O) = 11.109 \pm 0.005$ eV.[44]

4.5. DISCUSSION

4.5.1. Chemi-ionization Reaction

At the time of the chemical release, reaction (1) was assumed to be exothermic by 0.33 ± 0.20 eV on the basis of $D_0(SmO) = 5.88 \pm 0.17$ eV evaluated by Pedley and Marshall[18] along with $IE(SmO) = 5.55 \pm 0.10$ eV reported by Rauh and Ackermann.[13] (The subsequent evaluation by Konings *et al.*[22] suggests a smaller exothermicity of 0.21 ± 0.08 eV). Both values are within experimental uncertainty of the value measured directly by Cockett *et al.*, 0.28 ± 0.07 eV;[25] however, these data may be unduly influenced by

excited states, as discussed above. The present PFI-ZEKE results show that the electron impact ionization energy of SmO is too low by ~0.2 eV and greatly improves the precision of this value. Combined with the neutral bond energies, IE(SmO) = 5.7427 ± 0.0006 eV indicates that the exothermicity of reaction (1) decreases by 0.19 eV to 0.14 ± 0.17 or 0.02 ± 0.08 eV depending on the adopted D_0(SmO). These values are independently verified by combining $D_0(Sm^+\text{-}O) = 5.72_5 \pm 0.07$ eV from the present GIBMS results with IE(Sm) = 5.6437 ± 0.0006 eV. Doing so yields an exothermicity of 0.08 ± 0.07 eV, within experimental uncertainty of any of the IE(SmO)–D_0(SmO) values and midway between the values derived from the two updated and evaluated recommendations for D_0(SmO). Conversely, combining our $D_0(Sm^+\text{-}O)$ and IE(SmO) values provides D_0(SmO) = 5.83 ± 0.07 eV, consistent with but more precise than any literature evaluation.

The revised thermochemistry for this reaction may play a vital part in the lower than expected electron density observed in the recent Sm release. (It should be noted that this release occurred in sunlight, where photoionization could yield significant quantities of Sm^+, which would be long-lived with respect to recombination. However, the present SIFT and GIBMS results indicate that such ions would rapidly convert to SmO^+ via the reaction with O_2, reaction (4).) Although the chemi-ionization reaction (1) remains exothermic, and thus the reverse dissociative recombination reaction endothermic, the exothermicity is far less than previously believed. At the altitude of the release, ~200 km, the electron energy distribution is reasonably described by a temperature of ~1000 K, Fig. 4.10. A significantly larger fraction of this electron

distribution has enough energy to overcome the updated 0.08 eV barrier to recombination (Fig. 4.10), potentially leading to an equilibrium preventing full ionization of the released samarium and leading to the observed low electron density. The equilibrium constant of reaction (1) may be roughly estimated from the exothermicity reported here and calculation of $\Delta_r S^\circ_{1000} = -66$ J mol^{-1}K^{-1} [64,65] to be $\sim 10^{-3}$ at 1000 K. Taking the forward chemi-ionization rate constant[4] to be 10^{-11} cm^{3}s^{-1} yields a reverse dissociative recombination rate constant of $\sim 10^{-8}$ cm^{3}s^{-1}. Employing a typical ambient O atom density at 200 km to be 10^{10} cm^{-3}, an ambient electron density of 10^5 cm^{-3} , and a density of released Sm of 10^7 cm^{-3}, a simple, zero-dimensional model suggests incomplete ionization of the Sm, with an equilibrium at about 60% ionization, the same order of magnitude as that observed. (Assuming an exothermicity for reaction (1) of 0.33 eV, or even 0.21 eV, would suggest complete ionization.) This estimation is crude, but sufficient to justify further study. Although dissociative recombination kinetics have been studied for a wide range of systems[66] and are almost universally rapid ($k > 10^{-7}$ cm^{3}s^{-1}), no measurement has been made for any near endothermic or thermoneutral reaction such as the reverse of reaction (1). Measurement of the dissociative recombination cross-section for SmO^+, or for any of the systems with similar energetics (e.g., the much lower mass TiO^+ may be more amenable to study in a magnetic ion storage ring), would be informative.

4.6. CONCLUSION

We have reevaluated the exothermicity of the title reaction, $Sm + O \rightarrow SmO^+ + e^-$. The bond strength of SmO^+ has been measured as $5.72_5 \pm 0.07$ eV, using a GIBMS apparatus. Combined with the firmly established ionization energy of Sm, this gives an exothermicity of reaction (1) of 0.08 ± 0.07 eV. Furthermore, we have remeasured the ionization energy of SmO using REMPI/PFI-ZEKE, finding a value of 5.7427 ± 0.0006 eV, higher than the previously reported value of 5.55 ± 0.1 eV. Combining this IE with literature values for the SmO bond strength gives exothermicities of either 0.14 ± 0.17 or 0.02 ± 0.08 eV for reaction (1), independent of and in agreement with the IE(Sm) - $D_0(SmO^+)$ value, lending great confidence to the determination. Adopting this value suggests $D_0(SmO) = 5.83 \pm 0.07$ eV.

The exothermicity of the chemi-ionization reaction is far smaller than had been believed when the reaction was exploited to produce a local region of artificially high electron density by releasing Sm at ~200 km from a sounding rocket. This may explain the unexpectedly low electron yield observed in that release experiment, a result of incomplete ionization caused by equilibrium between the chemi-ionization reaction and the reverse dissociative recombination reaction. A significant unknown remaining in that analysis is the dissociative recombination cross-section of SmO^+ or of any other system with similar energetics (i.e. slightly endothermic to dissociative recombination).

REFERENCES

(1) N. S. Shuman, D. E. Hunton, and A. A. Viggiano, "Ambient and Modified Atmospheric Ion Chemistry: From Top to bottom," Chem. Rev. (in press).

(2) R. G. Caton, T. R. Pederson, R. T. Paris, K. M. Groves, P. A. Bernhardt, and P. S. Cannon, in American Geophysical Union, Fall Meeting, 2013.

(3) K. M. Groves, R. G. Caton, T. R. Pederson, R. T. Paris, Y. Su, P. S. Cannon, N. K. Jackson-Booth, M. J. Angling, and J. M. Retterer, in American Geophysical Union, Fall Meeting, 2013.

(4) K. Schofield, *J. Phys. Chem.* **110**, 6938 (2006).

(5) H. H. Lo and W. L. Fite, *Chem. Phys. Lett.* **29**, 39 (1974).

(6) W. L. Fite, H. H. Lo, and P. Irving, *J. Chem. Phys.* **60**, 1236 (1974).

(7) P. Vasu, H. H. Lo, and W. L. Fite, *Chem. Phys. Lett.* **54**, 89 (1978).

(8) T. A. Patterson, M. W. Siegel, and W. L. Fite, *J. Chem. Phys.* **69**, 2163 (1978).

(9) J. C. Halle, H. H. Lo, and W. L. Fite, *J. Chem. Phys*. **73**, 5681 (1980).

(10) W. L. Fite, T. A. Patterson, and M. W. Siegeal, "Cross Sections for thermal reactions between Uranium Atoms and Atmospheric Species Appendix 1: Associative Ionization Reactions Studied at ExtraNuclear Inc. and the University of Pittsburg up to December 31, 1976," Air Force Geophysics Laboratory Technical Report AD-A-038806, 1977.

(11) T. Jayasekharan, M. A. N. Razvi, and G. L. Bhale, *J. Phys. B: At., Mol. Opt. Phys.* **33**, 3123 (2000).

(12) S. G. Lias and J. E. Bartmess, NIST Chemistry WebBook (National Institute of Standards and Technology, Gaithersburg, MD, 20899, 2000), http://webbook.nist.gov.

(13) R. J. Ackermann, E. G. Rauh, and R. J. Thorn, *J. Chem. Phys.* **65**, 1027 (1976).

(14) D. L. Hildenbrand, *Chem. Phys. Lett.* **48**, 340 (1977).

(15) L. L. Ames, P. N. Walsh, and D. White, *J. Phys. Chem.* **71**, 2707 (1967).

(16) L. Brewer and G. M. Rosenblatt, in Advances in High Temperature Chemistry, edited by L. Eyring (Academic, New York, 1969), p. 1.

(17) C. R. Dickson and R. N. Zare, *Chem. Phys.* **7**, 361 (1975).

(18) J. B. Pedley and E. M. Marshall, *J. Phys. Chem. Ref. Data* **12**, 967 (1983).

(19) M. S. Chandrasekharaiah and K. A. Gingerich, in *Handbook on the Physics and Chemistry of Rare Earths*, edited by K. A. Gschniedner and L. Eryring, Jr. (Elsevier, Amsterdam, 1989).

(20) J. K. Gibson, *J. Phys. Chem. A* **107**, 7891 (2003).

(21) S. G. Lias, J. E. Bartmess, J. F. Liebman, J. L. Holmes, R. D. Levin, and W. G. Mallard, *J. Phys. Chem. Ref. Data, Suppl.* **17**, 1 (1988).

(22) R. J. M. Konings, O. Benes, A. Kovacs, D. Manara, D. Sedmidubsky, L.Gorokhov, V.S.Iorish, V.Yungman, E.Shenyavskaya, and E.Osina, *J.Phys. Chem. Ref. Data* **43**(1), 013101 (2014).

(23) E. Murad and D. L. Hildenbrand, *J. Chem. Phys.* **73**, 4005 (1980).

(24) J. Paulovic, L. Gagliardi, J. M. Dyke, and K. Hirao, *J. Chem. Phys.* **120**, 9998 (2004).

(25) M. C. R. Cockett, L. Nyulaszi, T. Veszpremi, T. G. Wright, and J. M. Dyke, *J.*

Electron Spectrosc. Relat. Phenom. **57**, 373 (1991).

(26) J. E. Sansonetti and W. C. Martin, *J. Phys. Chem. Ref. Data* **34**, 1559 (2005).

(27) A. A. Viggiano, R. A. Morris, F. Dale, J. F. Paulson, K. Giles, D. Smith, and T. Su, *J. Chem. Phys.* **93**, 1149 (1990).

(28) J. J. Melko, S. G. Ard, N. S. Shuman, R. E. Pedder, C. R. Taormina, and A. A. Viggiano, "Coupling an Electrospray Source and a Solids Probe/Chemical Ionization Source to a Selected Ion Flow Tube Apparatus" (unpublished).

(29) S. K. Loh, D. A. Hales, L. Li, and P. B. Armentrout, *J. Chem. Phys.* **90**, 5466 (1989).

(30) R. H. Schultz and P. B. Armentrout, *Int. J. Mass Spectrom. Ion Processes* **107**, 29 (1991).

(31) C. L. Haynes and P. B. Armentrout, *Organometallics* **13**, 3480 (1994).

(32) D. E. Clemmer, Y.-M. Chen, F. A. Khan, and P. B. Armentrout, *J. Phys. Chem.* **98**, 6522 (1994).

(33) B. L. Kickel and P. B. Armentrout, *J. Am. Chem. Soc.* **117**, 764 (1995).

(34) B. L. Kickel and P. B. Armentrout, *J. Am. Chem. Soc.* **117**, 4057 (1995).

(35) M. R. Sievers, Y.-M. Chen, J. L. Elkind, and P. B. Armentrout, *J. Phys. Chem.* **100**, 54 (1996).

(36) D. Gerlich, *Adv. Chem. Phys.* **82**, 1 (1992).

(37) K. M. Ervin and P. B. Armentrout, *J. Chem. Phys.* **83**, 166 (1985).

(38) P. B. Armentrout, *Int. J. Mass Spectrom.* **200**, 219 (2000).

(39) N. R. Daly, *Rev. Sci. Instrum.* **31**, 264 (1960).

(40) W. J. Chesnavich and M. T. Bowers, *J. Phys. Chem.* **83**, 900 (1979).

(41) F. Muntean and P. B. Armentrout, *J. Chem. Phys.* **115**, 1213 (2001).

(42) N. Aristov and P. B. Armentrout, *J. Am. Chem. Soc.* **108**, 1806 (1986).

(43) P. B. Armentrout, in *Advances Gas Phase Ion Chemistry*, edited by N. Adams and L. M. Babcock (JAI Press, Greenwich, Connecticut, 1992), p. 83.

(44) R. D. Johnson III, NIST Computational Chemistry Comparison and Benchmark Database NIST Standard Reference Database Number 101 Release 16a, NIST, 2013.

(45) M. C. Heaven, B. J. Barker, and I. O. Antonov, *J. Phys. Chem. A* **118**, 10867 (2014).

(46) G. Bujin and C. Linton, *J. Mol. Spectrosc.* **137**, 114 (1989).

(47) G. Bujin and C. Linton, *J. Mol. Spectrosc.* **147**, 120 (1991).

(48) H. Salami and A. J. Ross, *J. Mol. Spectrosc.* **233**, 157 (2005).

(49) E. Murad, *Int. J. Mass Spectrom. Ion Processes* **58**, 159 (1984).

(50) G. K. Koyanagi and D. K. Bohme, *J. Phys. Chem. A* **105**, 8964 (2001).

(51) M. J. Y. Jarvis, V. Blagojevic, G. K. Koyanagi, and D. K. Bohme, *Phys. Chem. Chem. Phys.* **12**, 4852 (2010).

(52) J. J. Melko, S. G. Ard, J. A. Fournier, N. S. Shuman, J. Troe, and A. A. Viggiano, *J. Phys. Chem. A* **116**, 11500 (2012).

(53) J. J. Melko, S. G. Ard, J. A. Fournier, N. S. Shuman, J. Troe, and A. A. Viggiano, *J. Phys. Chem. A* **117**, 9108 (2013).

(54) V. Blagojevic, E. Flaim, M. J. Y. Jarvis, G. K. Koyanagi, and D. K. Bohme, *Int. J. Mass Spectrom.* **385,** 249-250 (2006).

(55) V. Blagojevic, M. J. Y. Jarvis, G. K. Koyanagi, and D. K. Bohme, *J. Phys. Chem. A* **117**, 3786 (2013).

(56) P. Cheng, G. K. Koyanagi, and D. K. Bohme, *J. Phys. Chem. A* **110**, 12832 (2006).

(57) R. M. Cox, J. Kim, and P. B. Armentrout, "A Guided Ion Beam Study of the Reactions $Sm^+ + CO_2/NO$" (unpublished).

(58) T. Su and W. J. Chesnavich, *J. Chem. Phys.* **76**, 5183 (1982).

(59) C. M. Western, *PGOPHER*, A Program for Simulating Rotational Structure, University of Bristol, 2007.

(60) E. R. Fisher, B. L. Kickel, and P. B. Armentrout, *J. Chem. Phys.* **97**, 4859 (1992).

(61) M. R. Sievers, Y.-M. Chen, and P. B. Armentrout, *J. Chem. Phys.* **105**, 6322 (1996).

(62) X.-G. Zhang and P. B. Armentrout, *J. Phys. Chem. A* **107**, 8915 (2003).

(63) S. P. Willson and L. Andrews, *J. Phys. Chem. A* **103**, 3171 (1999).

(64) M. W. Chase, Jr., C. A. Davies, J. R. Downey, Jr., D. J. Frurip, R. A. McDonald, and A. N. Syverud, *J. Phys. Chem. Ref. Data, Suppl.* **14**, 927 (1985).

(65) A. Kramida, Y. Ralchenko, and J. Reader, NIST Atomic Spectra Database (ver. 5.2), National Institute of Standards and Technology, Gaithersburg, MD, 2014, available online: http://physics.nist.gov/asd.

(66) M. Larsson and A. E. Orel, *Dissociative Recombination of Molecular Ions* (Cambridge University Press, Cambridge, 2008).

TABLE 4.1. Reaction Rate Constants, Efficiencies, and Temperature Dependence for Reactions of Sm^+ with N_2O, O_2, NO_2, CO_2, SO_2, and NO Measured Using the VT-SIFT Apparatus

$Sm^+ + LO \rightarrow SmO^+ + L$	D_0(L-O)[a]	k_{300}[b]	k/k_{col}[c]	Literature k/k_{col}	T dep.
LO = N_2O	1.667±0.001	1.3±0.3	0.18±0.05	0.19±0.06[d]	$T^{-0.4}$
NO_2	3.116±0.001	6.3±1.6	0.84±0.21	1.0±0.3[e]	$T^{-0.6}$
O_2	5.117±0.001	2.8±0.9	0.49±0.15 (1.0±0.2)	0.48±0.14[d]	$T^{-0.1}$
CO_2	5.453±0.002	NR		NR[f]	
SO_2	5.661±0.014	4.0±1.2	0.29±0.09 (0.22±0.04)		$T^{-0.6}$
NO	6.500±0.004	NR		NR[g]	

[a] BDEs (eV) calculated from thermochemical data found in Ref. 44.

[b] Rate at 300 K (in units of 10^{-10} cm^3s^{-1}). NR = no reaction observed

[c] Reaction efficiency where k_{col} is defined as the Su-Chesnavich semi-classical ion trajectory rate.[58] Values in parenthesis are measured using GIBMS.

[d] Ref. 50.

[e] Ref. 51.

[f] Ref. 56.

[g] Reported as a secondary reaction in Ref. 54. See also text and Refs. 52, 53, and 55.

TABLE 4.2. Apparent Termolecular Rate Constants for Reactions of SmO^+ with O_2, NO_2, N_2O, SO_2, and CO_2

Reaction	$k_{termolecular}(300K)$ ($\times 10^{-27}$ cm^6s^{-1})[a]
$SmO^+ + O_2 + He \rightarrow SmO(O_2)^+ + He$	Observed
$SmO^+ + CO_2 + He \rightarrow SmO(CO_2)^+ + He$	0.1
$SmO^+ + N_2O + He \rightarrow SmO(N_2O)^+ + He$	0.1
$SmO^+ + SO_2 + He \rightarrow SmO(SO_2)^+ + He$	1.2
$SmO^+ + NO_2 + He \rightarrow SmO(NO_2)^+ + He$	2.1

[a] See text for a discussion of uncertainty

TABLE 4.3. Fitting Parameters of Eq. (2) for the Indicated Reaction Cross Section

Reaction		σ_0	n	E_0(eV)
$Sm^+ + CO$	$\rightarrow SmO^+ + C$	0.5±0.2	2.3±0.2	5.49±0.15
	$\rightarrow SmC^+ + O$	1.1±0.1	1.7±0.2	8.95±0.07
$Sm^+ + SO_2$	$\rightarrow SmSO^+ + O$	1.3±0.2	1.8±0.2	3.86±0.08
$Sm^+ + Xe$	$\rightarrow Sm^+ + O + Xe$	0.1.±0.1	2.0±0.2	5.67±0.16
$Sm^+ + O_2$	$\rightarrow SmO_2^+ + O$	1.1±0.2	1.0±0.2	3.98±0.15
	$\rightarrow Sm^+ + O + O_2$	0.3±0.1	1.2±0.1	5.78±0.09

FIGURE 4.1.

Energy schematic of values employed for the determination of $\Delta_r H^o_0$ for reaction (1).

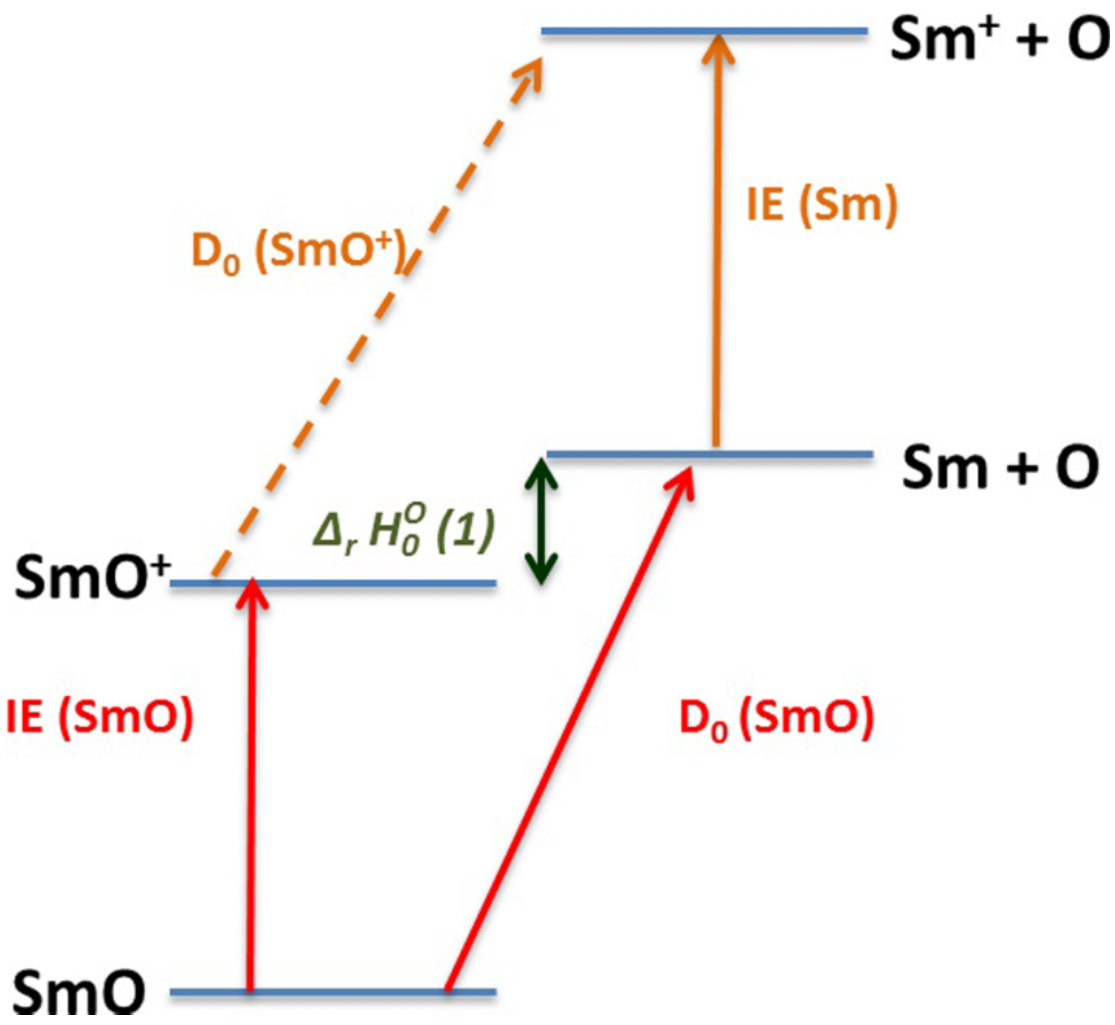

FIGURE 4.2.

Cross sections for the reaction between Sm^+ and O_2 as a function of energy in the center-of-mass (lower x-axis) and laboratory (upper x-axis) frames. The arrow indicates the bond energy of O_2. The line is the calculated semi-classical trajectory collision cross section.

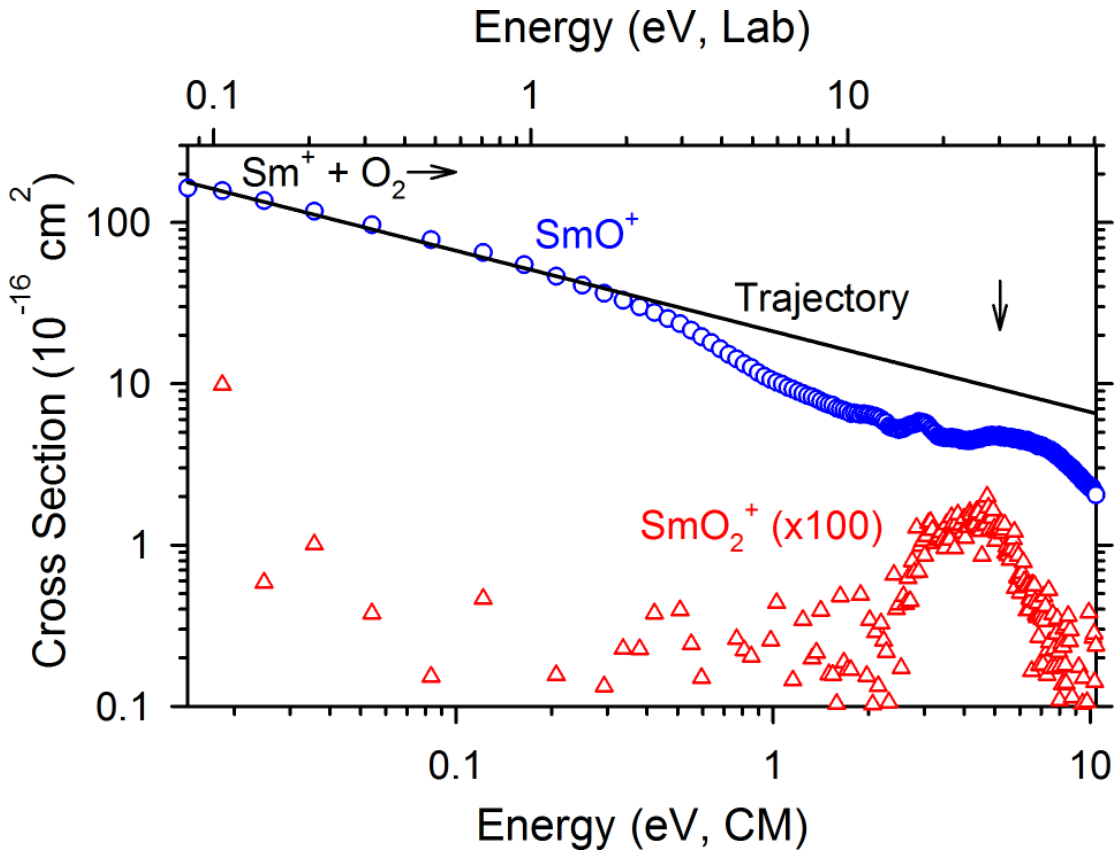

FIGURE 4.3.

Cross sections for the reaction between Sm^+ and SO_2 as a function of energy in the center-of-mass (lower x-axis) and laboratory (upper x-axis) frames. The arrow indicates the bond energy of OS-O. The line is the calculated semi-classical trajectory collision cross section.

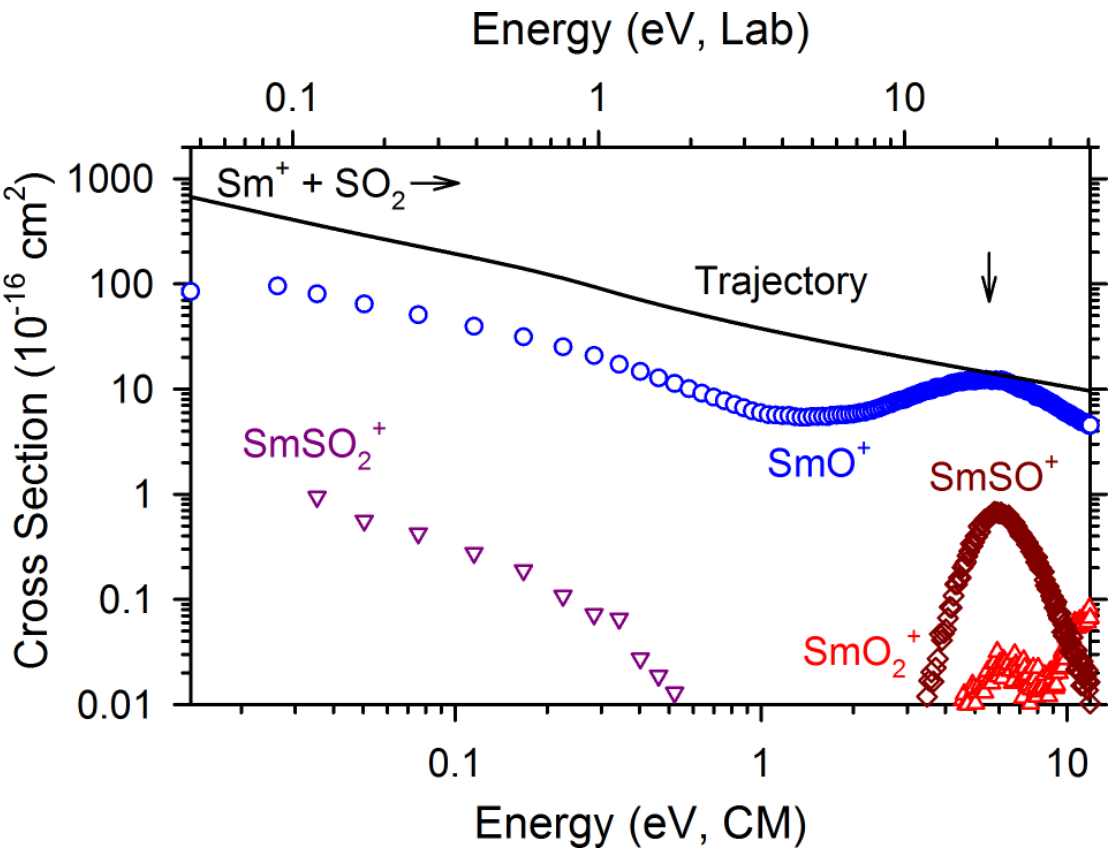

FIGURE 4.4.

Cross sections for the reaction between Sm^+ and CO as a function of energy in the center-of-mass (lower x-axis) and laboratory (upper x-axis) frames. The arrow indicates D_0(C-O). The dashed lines show the model cross section given by Eq. (2). Solid lines are convoluted over the experimental energy distributions.

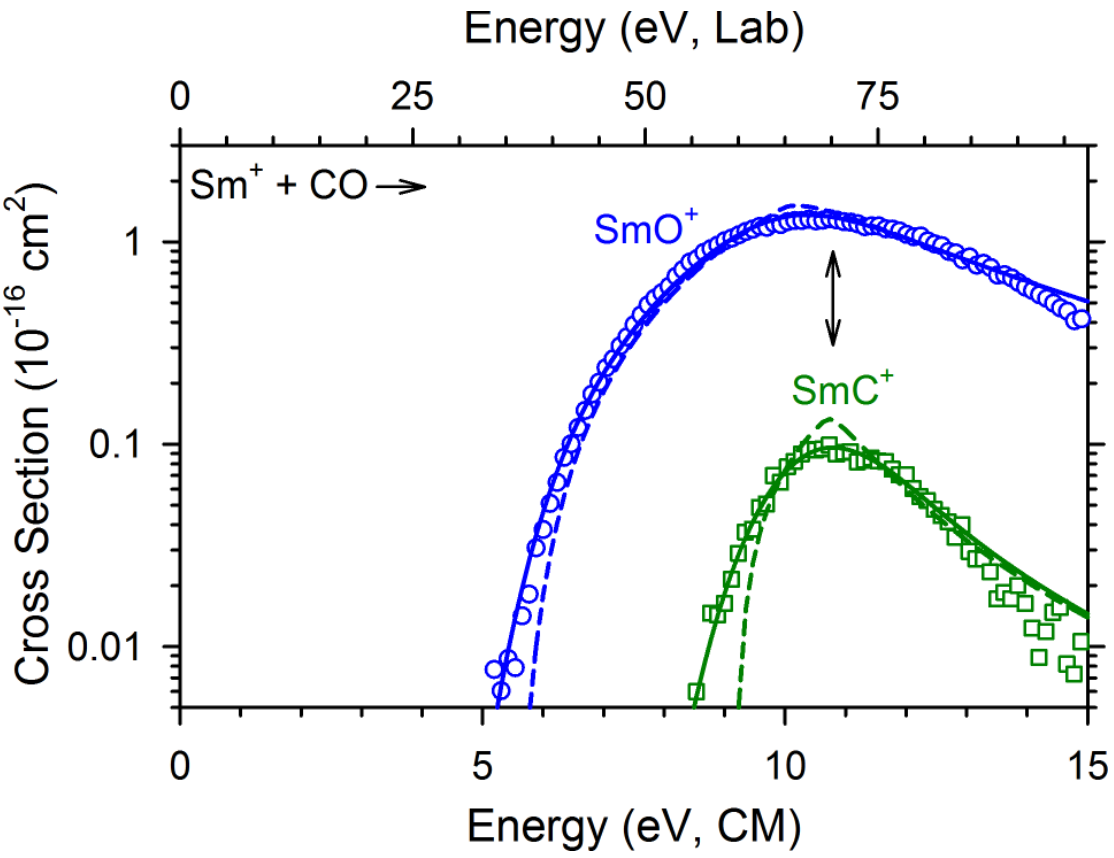

FIGURE 4.5.

Cross section for the collision-induced dissociation reaction between SmO^+ and Xe as a function of energy in the center-of-mass (lower x-axis) and laboratory (upper x-axis) frames. The dashed line represents the model cross section given by Eq. (2). The solid line is convoluted over the experimental energy distributions.

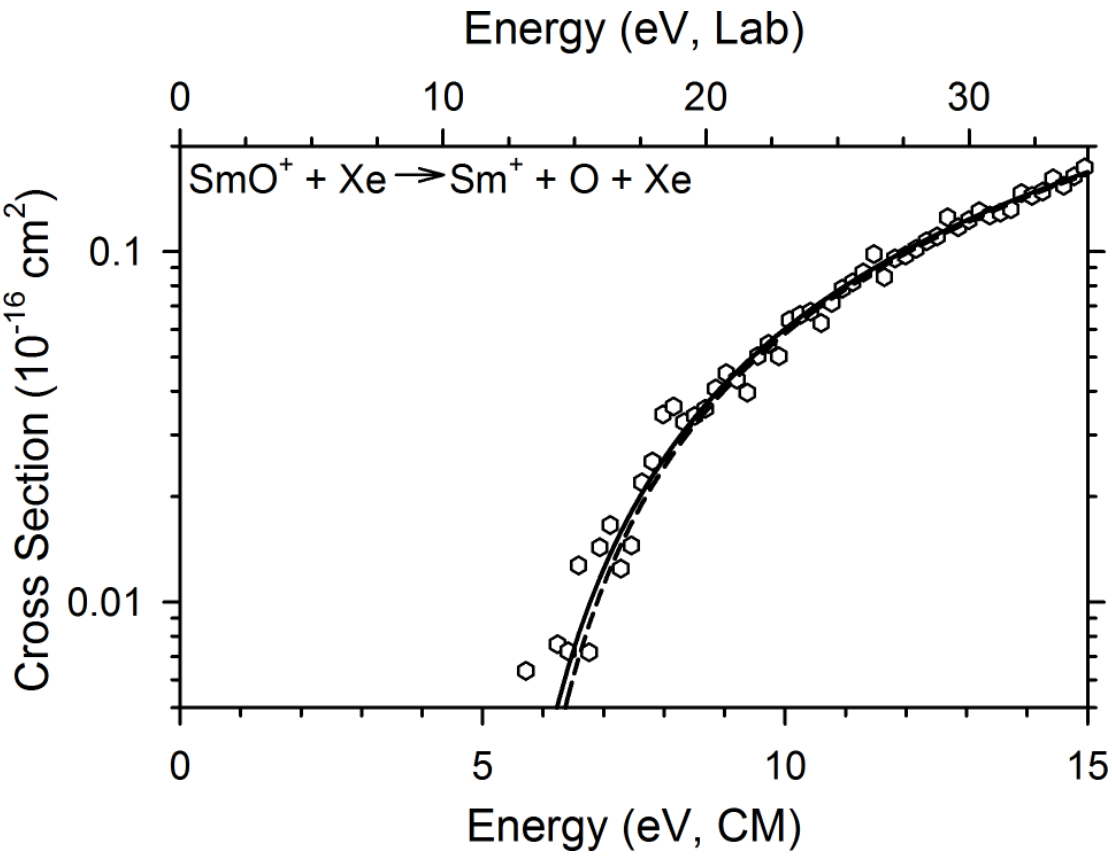

FIGURE 4.6.

Cross sections for the reaction between SmO^+ and O_2 as a function of energy in the center-of-mass (lower x-axis) and laboratory (upper x-axis) frames. The arrow indicates D_0(O-O). The dashed lines show the model cross section given by Eq. (2). Solid lines are convoluted over the experimental energy distributions.

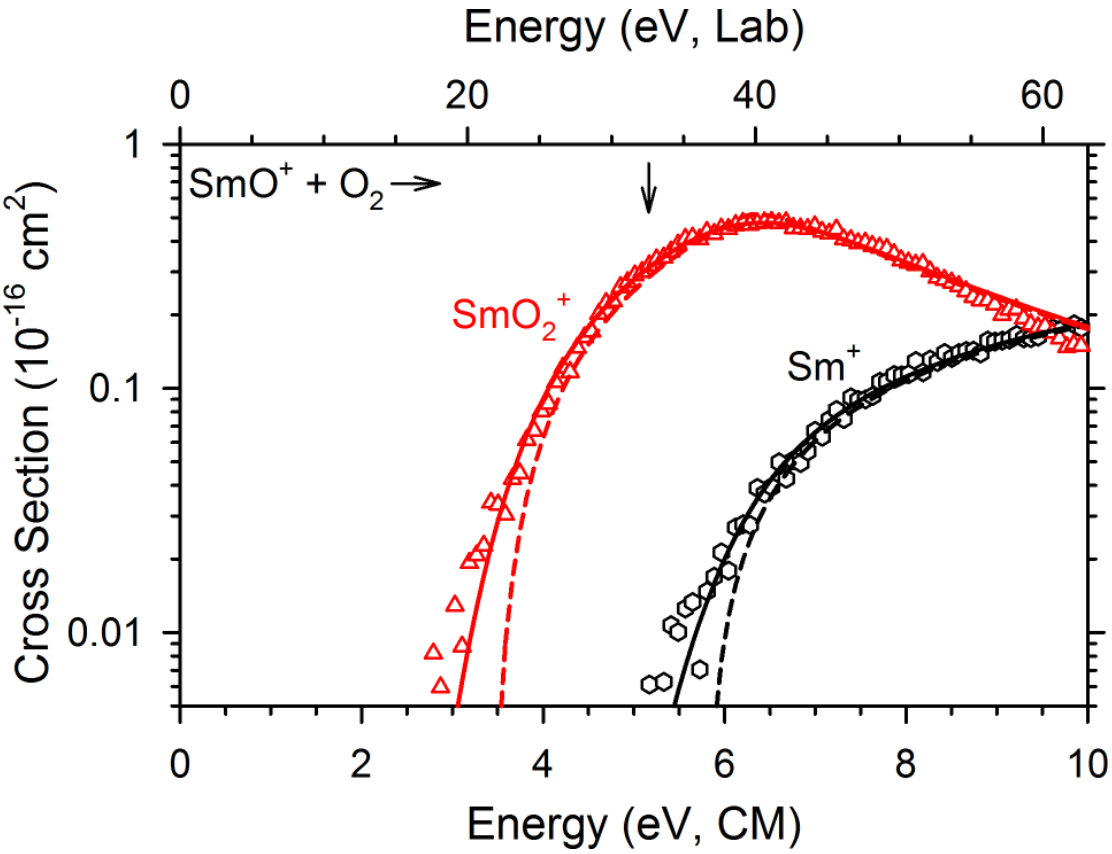

FIGURE 4.7.

Section of the SmO LIF spectrum showing the [16.6]1-X0^{-} origin band (upper trace).The downward-going trace is a simulation of the rotational contour using the two most abundant isotopologues (^{152}SmO and ^{154}SmO). The rotational temperature for the simulation was 10 K.

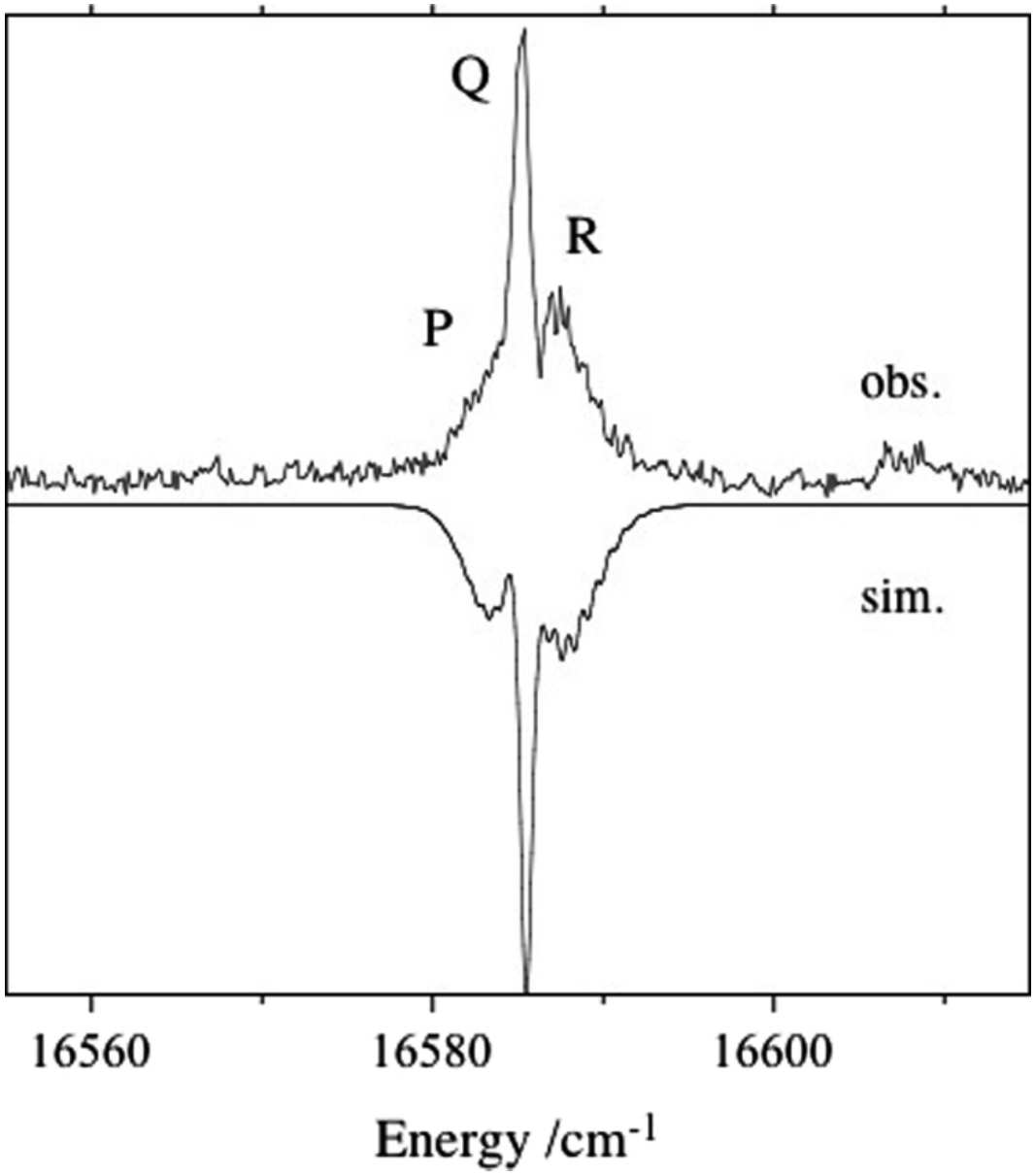

FIGURE 4.8.

Photoionization efficiency curve for ionization of SmO via the [16.6]1state. This trace was recorded with the first laser tuned to the Q-branch feature of the spectrum shown in Fig. 4.7. The abscissa is the energy sum of the two photons. The local electric field for this measurement was 250 V cm^{-1}.

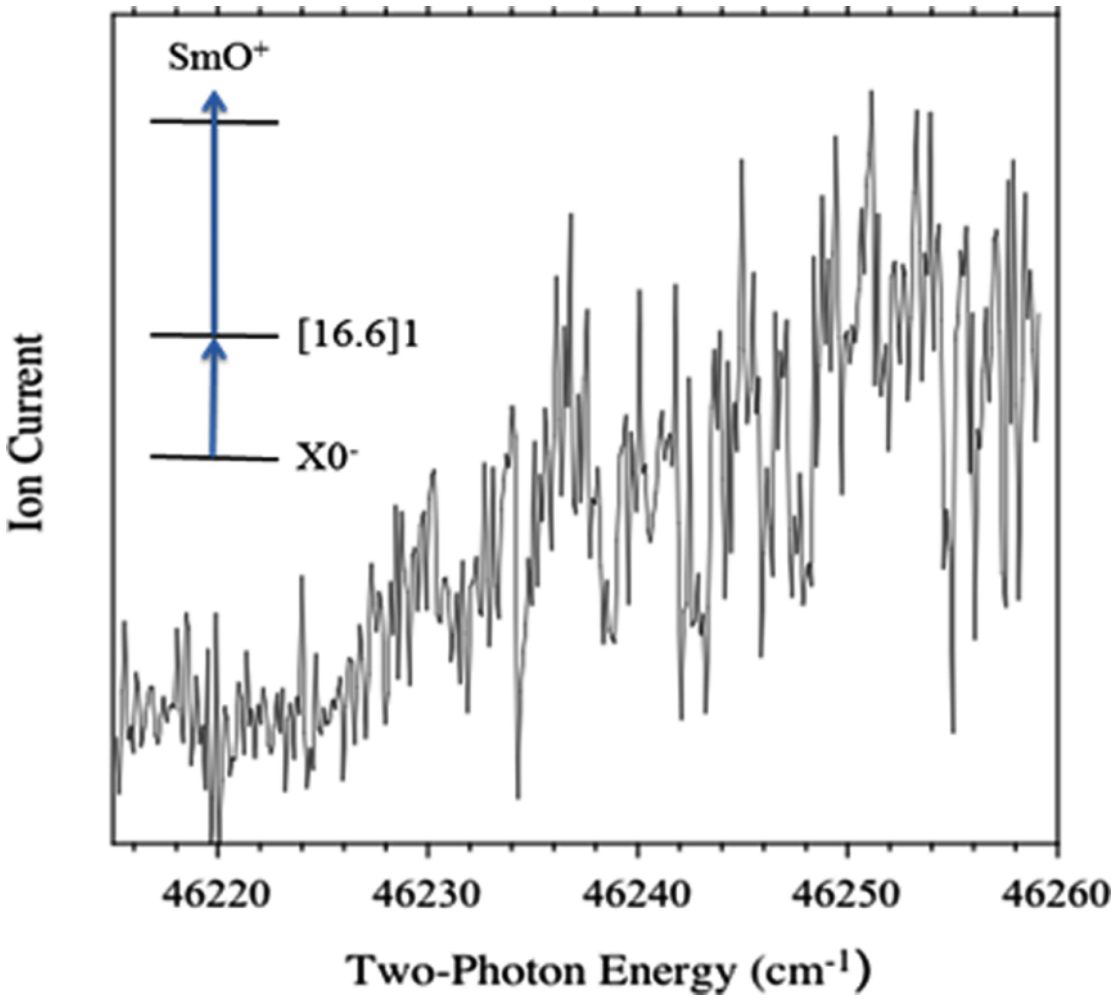

FIGURE 4.9.

A PFI-ZEKE spectrum for SmO recorded using first photon excitation of the Q-branch of the [16.6]1-$X0^-$ origin band. The vertical broken line indicates the blue-edge of the high-n Rydberg series that converges on the zero-point level of SmO^+.

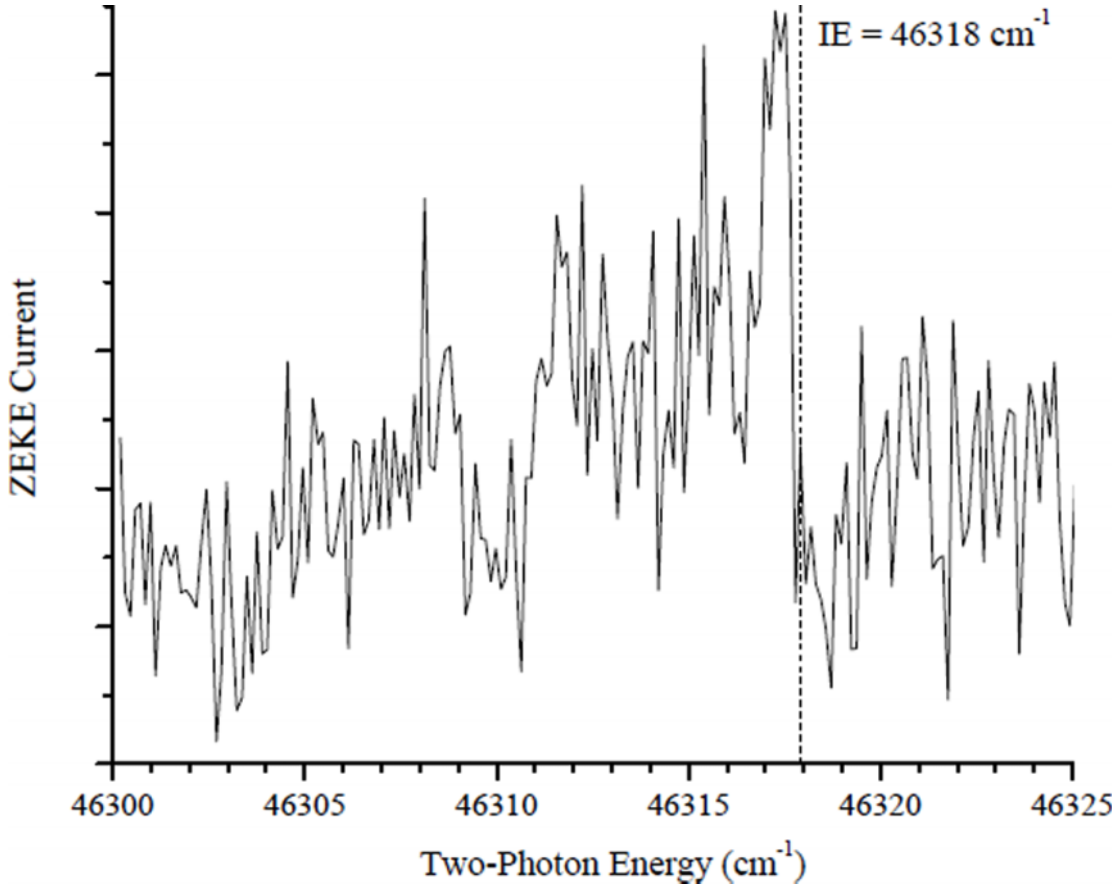

FIGURE 4.10.

Electron energy distribution for $T_{electron}$ =1000 K. The red shaded region highlights electrons energetic enough to overcome the barrier to the reverse of reaction (1) from previously reported thermochemistry. The blue shaded region highlights the electrons meeting this requirement with the newly derived value.

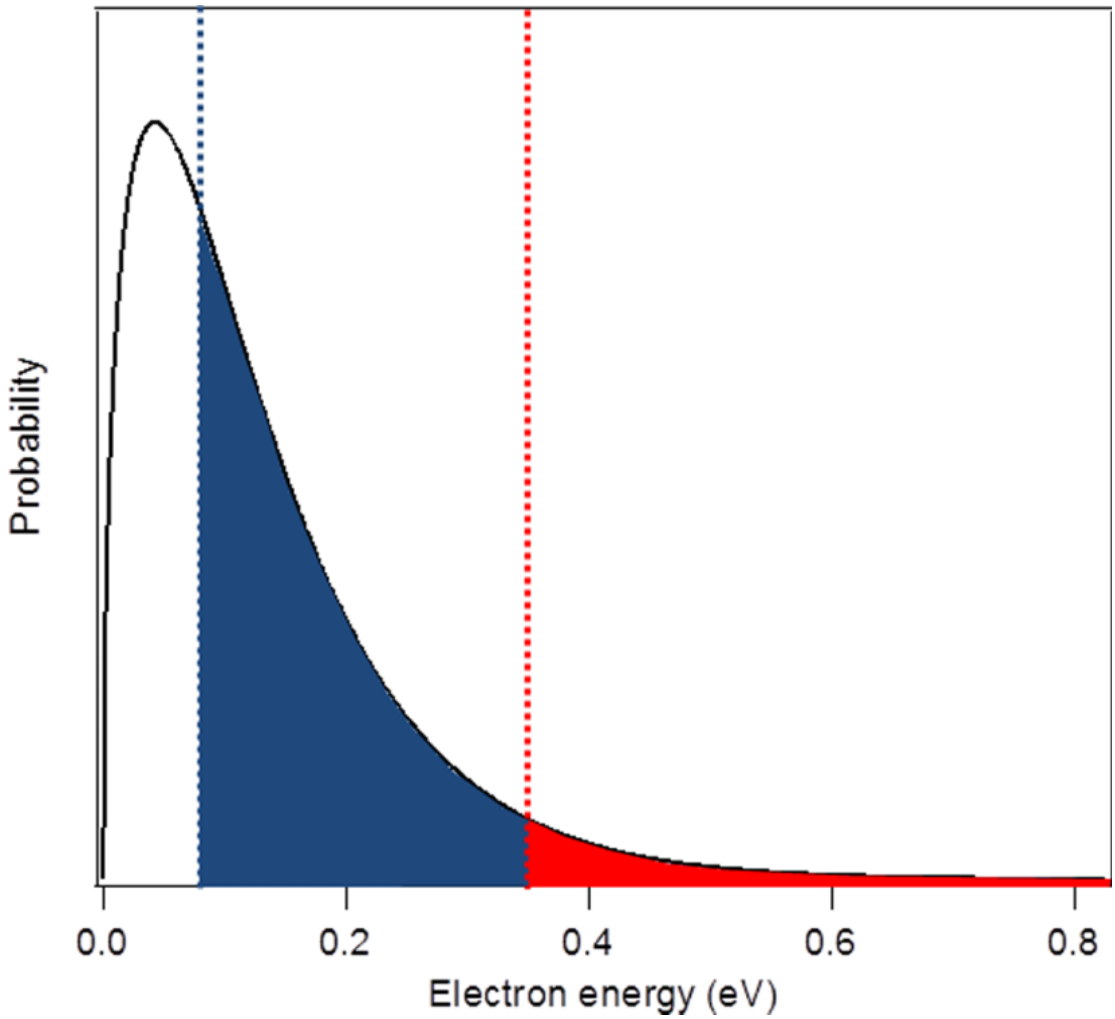

Chapter 5

Spectroscopic and Theoretical Studies of the Low-Lying States of BaO^+

5.1. INTRODUCTION

Theoretical calculations have been used to explore the systematic variations in the bonding of alkaline-earth monoxide cations (MO^+, M=Be, Mg, Ca, Sr, and Ba)[1-3]. The ground states may be formally assigned to the $M^{2+}O^-(2p^5)$ configuration, and the bonding becomes increasingly more ionic as the atomic number of the metal increases (and the ionization energies decrease). The lightest member of the series, BeO^+, has a significant covalent contribution to the bonding, while the bonding interactions of heaviest species are mostly ionic[1]. As a consequence, theoretical calculations predict a switch in the symmetry of the ground state that occurs between CaO^+ and SrO^+. This behavior can be understood by considering the interaction between a closed-shell M^{2+} cation and the O^- ($2p^5$) anion. Approach of the metal along the axis of a filled or half-filled O 2p orbital will produce a $^2\Pi$ or $^2\Sigma^+$ state, respectively. For the lighter metals it is favorable to approach the filled 2p orbital ($X^2\Pi$), but the electrostatic repulsion increases with the

atomic number, causing the switch to an $X^2\Sigma^+$ ground state for SrO^+ and BaO^+.

While these predictions seem entirely reasonable they have yet to be validated by experimental observations. Ionization and bond dissociation energies have been reported for the neutral MO species[4], but gas phase spectroscopic data for the cations are almost entirely lacking. Dyke *et al*.[2] reported gas-phase photoelectron spectra for SrO and BaO. For both molecules the spectra exhibited a single broad feature that could be used to estimate the adiabatic and vertical ionization energies. Dyke *et al*.[2] noted that the broadness of the bands was most probably due to overlapping vibrational progressions associated with the MO^+ $^2\Sigma^+$ and $^2\Pi$ electronic states. This assignment was supported by the predictions from relativistic Hartree-Fock Slater calculations.

Renewed interest in the spectroscopy of MO^+ species has been generated by the recognition that they are promising candidates for laser cooling and ion trapping experiments[5-10]. The intense atomic ion *sp* transitions facilitate cooling to ultra-cold temperatures. This is analogous to laser cooling of alkali metal atoms, but with the advantage that the cold ions can be easily manipulated using external fields. Reactions of ions that are trapped in a Coulomb crystal can then be used to produce translationally cold molecular ions, as has been demonstrated[5-10] for CaO^+, BaO^+, and $BaCl^+$. The task of characterizing the internal state distributions of these ions is currently hampered by the lack of spectroscopic data.

The primary objective of the present study was to obtain spectroscopic data for the two lowest energy electronic states of BaO^+. This has been accomplished using resonant two-photon ionization techniques. In addition, these measurements provide an

accurate value for the ionization energy (IE) of BaO. Previous studies[2,11-13] have reported values that range from 6.5 to 7.0 eV.

In parallel with the experimental effort we have used relativistic electronic structure calculations to predict the molecular constants of BaO^+. In the absence of experimental data, electronic structure calculations are being used to guide the design experiments where action spectroscopy techniques will be used to determine and manipulate internal state population distributions. It is therefore informative to use this study of BaO^+ as a means to assess the predictive quality of commonly used electronic structure methods, as applied to the cations of interest for cold molecule experiments.

5.2. EXPERIMENTAL

The apparatus used for these measurements has been described in previous publications[14]. BaO was generated by pulsed laser vaporization of a pure Ba target. The ablation plume was entrained in a carrier gas that consisted of 1% N_2O in He. Following the reactions that formed BaO in the ablation source, the gas mixture was subject to supersonic jet expansion via a 0.8 mm diameter orifice. As a preliminary to photoionization measurements, the production of BaO was optimized using laser induced fluorescence (LIF) detection. A pulsed tunable dye laser (Lambda Physik, Scan-Mate Pro, 0.15 cm^{-1} linewidth, 10 ns pulse duration) was used as the excitation source.

For photo-ionization measurements, the core of the supersonic expansion was sampled, via a conical skimmer, into a second vacuum chamber. This was equipped with

a Wiley-McClaren time-of-flight mass spectrometer and a separate set of microchannel plates for photoelectron detection. The Scan-Mate Pro dye laser was used for the first excitation step. Ionization was achieved using pulses from a second Nd/YAG pumped dye laser (Continuum ND6000, 0.1 cm^{-1} linewidth, 10 ns pulse duration). Frequency doubling of the output from the ND6000 was used to generate tunable UV light in the 274-295 nm range. Absolute wavenumber calibration of the Scan-Mate Pro laser was established by recording two-photon transitions of atomic Ba[15] using one-color, 2+1 photo-ionization. The fundamental output from the ND6000 dye laser was calibrated against the I_2 B-X spectrum[16].

Resonantly enhanced multi-photon ionization (REMPI) spectra were recorded by scanning the wavelength of the first laser, with the energy of the second photon set high enough to ionize the excited neutrals. Photo-ionization efficiency (PIE) curves were recorded with the first laser tuned to an established electronic transition of BaO, and the wavelength of the second laser was swept to locate the ionization threshold[14]. For both REMPI and PIE scans the mass spectrometer was used to monitor the signals resulting from the most abundant isotopologue ($^{138}BaO^+$). The threshold ionization energy and spectra for the BaO^+ ions were obtained by means of pulsed-field ionization zero kinetic energy (PFI-ZEKE) photoelectron spectroscopy. An ionizing field of 0.36 V/cm was applied 2 ms after the second laser pulse.

5.3. RESULTS

For two-color photoionization measurements it is often convenient to use a transition for the excitation step that is somewhat below half of the ionization energy, thereby avoiding contributions from one-color two-photon ionization. Given the previous determinations of the IE, we chose to use the $A^1\Sigma^+$-$X^1\Sigma^+$ v''-0 bands, with v'=5-8. These transitions have been examined in detail by Gottscho *et al*.[16,17] As an example of the present results, Fig. 5.1 shows a typical LIF spectrum for the 8-0 band, along with a simulation of the rotational structure. The later used only the band origin and literature values for the B rotational constants. The rotational temperature of this simulation was 20 K. Note that the structure of only one isotopologue (^{138}BaO) has been simulated. The Ba sample used contained a natural isotopic distribution, with leading contributions of 71.7% ^{138}Ba, 11.2% ^{137}Ba, 7.9% ^{136}Ba and 6.6%^{135}Ba. The peaks observed at energies above the prominent band head are the corresponding band heads of the lighter isotopologues.

Low-resolution PIE scans were used to obtain an initial estimate of the IE. These measurements, conducted using the A-X 5-0 band-head for the first excitation step, yielded an IE of 54960(50) cm^{-1}. However, the determination of the true threshold was complicated by the presence of one-color two-photon ionization signals produced by the second laser.

Most of the PFI-ZEKE spectra were recorded using the ^{138}BaO A-X 8-0 band head for the initial excitation. This feature is primarily composed of the overlapping R(3), R(4)

and R(5) lines. There are also contributions from the P-branch lines of the lighter isotopologues. The PFI-ZEKE spectrum, shown in Fig. 5.2, was surprisingly complex. Consequently, a two-dimensional approach was used to establish lower state rotational assignments. Measurements were performed by scanning the first laser over the 8-0 band, with the second laser set to excite a specific PFI-ZEKE resonance. Fig. 5.3a shows the spectrum obtained with the second laser tuned to the prominent PFI-ZEKE feature seen at 34352 cm^{-1} in Fig. 5.2. This trace consists of the two rotational lines that terminate on the J'=7 rotational level of A, $^1\Sigma^+$ v'=8. Fig. 5.3b shows the result of monitoring the PFI-ZEKE feature at 34344 cm^{-1}. In this instance, it is apparent that excitation of both the J'=3 and J'=9 intermediate levels contribute to the PFI-ZEKE resonance.

Another interesting facet of the PFI-ZEKE spectrum was revealed when initial excitation of an 8-0 P-branch line was used. For the laser linewidths used in these measurements the P(J) and R(J+8) lines were overlapped. Despite the low thermal population of the J+8 levels, the higher angular momentum states always produced PFI-ZEKE signals that were comparable in intensity to those from lower J levels that were accessed by P-line excitation. Overall, the two-dimensional maps indicated that probabilities for PFI-ZEKE transitions from A, v'=8 increased rapidly with increasing angular momentum.

Scans of the higher energy regions of the PFI-ZEKE spectrum were made to observe the vibrationally excited levels of the ground state ion, and the low-lying vibronic levels of the $A^2\Pi$ state. To obtain the best signal to noise ratios, initial excitation of the 8-0 band head was used. A low-resolution survey scan of the PFI-ZEKE spectrum

is shown in Fig. 5.4, where the ground state vibrational levels v^+= 0-4 are indicated, along with the v^+=0 levels of $A^2\Pi_{3/2}$ and $A^2\Pi_{1/2}$ states. The rotational structures observed for the excited vibrational levels of the ground state were noisier than the v^+=0 trace shown in Fig. 5.3a, but the patterns were similar. The rotational structures of the A state features were less well resolved than that of the X state v^+=0 band. An example is shown in Fig. 5.5. The red-shaded A state rotational contours were consistent with transitions from the rotational levels of the intermediate state (J=4, 5 and 6) to the lowest energy rotational levels of the A state. However, the congestion and poor signal to noise ratios of these features did not permit unambiguous rotational level assignments.

5.3.1. Electronic Structure Calculations

Relativistic electronic structure calculations were used to predict the low-lying states of BaO^+ and the ground state properties of BaO. All of the electronic structure calculations were carried out using the MOLPRO 2010.1 suite of programs[19].

The cation was examined using coupled cluster (CCSD(T)), multi-reference configuration (MRCI) and density functional theory (DFT) formalisms. In all cases, the Roos Atomic Natural Orbital (ANO) basis set was used for oxygen[20]. For Ba we examined both the all-electron Roos ANO basis set[21] and a 46 electron relativistic effective core potential (RECP)[22] with an ANO basis set for the valence electrons (ECP46MWB). To include scalar relativistic effects, the all-electron calculations used the second order Douglas-Kroll-Hess Hamiltonian. The MRCI calculations, which used

complete active space self-consistent field (CASSCF) results for reference wavefunctions, were carried out for the $X^2\Sigma^+$ ground state and the $A^2\Pi$ state. They included the Davidson correction[23] and spin-orbit coupling (MRCI+Q/SO). For the spin-orbit interaction, the matrix elements of the Breit-Pauli Hamiltonian were evaluated using the CASSCF wavefunctions. The diagonal elements of the Breit-Pauli matrix included the spin-free energies from the CASSCF/MRCI+Q calculations. The active space for the latter consisted of the O 2s and 2p orbitals, and the Ba 4d, 5s, 5p, and 6s orbitals (26 electrons in 14 orbitals).

Spin-free calculations for the $A^2\Pi$ state were carried out using the CCSD(T) and DFT/B3LYP formalisms. As Molpro uses the C_{2v} point group for heteronuclear diatomic molecules, the A state energies were obtained as the lowest energy solutions for the b_1 irreducible representation.

Point-wise potential energy curves were computed over the range of internuclear distances (R) from 1.9 to 2.7 Å, with a step size of 0.02 Å. Ro-vibronic eigenstates were calculated from these potentials by fitting the data near the equilibrium distance to Morse potentials (typically, data spanning 3000 cm^{-1} were used). In a few instances, the validity of this approximation was tested by comparing to numerical solutions for the point-wise potentials. The program Level 8.0[24] was used to obtain the eigenstates and expectation values. The differences between the molecular constants generated by the Morse approximation or Level 8.0 were below the accuracy expected of the electronic structure calculations (e.g., ω_e values that differed by less than 4 cm^{-1}).

Potential energy curves for the X and A states, generated by the MRCI+Q/SO

calculations, are shown in Fig. 5.6. In keeping with all of the calculations performed in this study, and the previous work of Dyke *et al*., the ground state was predicted to be $X^2\Sigma^+$. Molecular constants for this state, calculated using the above-mentioned series of electronic structure methods, are collected in Table 5.1. In addition, trial calculations were performed for the all-electron basis set using 4th order Douglas-Kroll-Hess Hamiltonian This enhancement did not have a significant influence on the results. MRCI+Q/SO calculations, performed with the ECP46_ANO basis set yielded potential energy curves of Fig. 5.6, but with a lower value for the spin-orbit interaction of the $A^2\Pi$ state. While the spin-orbit splitting of the all-electron calculation was 199 cm^{-1} (at the equilibrium distance) the ECP calculation yielded an interval of 119 cm^{-1}. As expected from the $Ba^{2+}O(2p^5)^-$ configuration, Ω=3/2 was predicted to be the lowest energy component of the A state (where Ω is the unsigned projection of the electronic angular momentum along the bond axis). Computed molecular constants for the A state are presented in Table 5.1.

Calculations for the $X^1\Sigma^+$ state of neutral BaO were carried out to provide a test of the computational methods employed, and for prediction of the IE. The results are collected in Table 5.2, along with experimental values for the molecular constants.

As noted in the Introduction, pure vibrational and A-X transitions of BaO^+ are of interest for manipulation of this ion under ultra-cold conditions. Consequently, we have used the results from the MRCI+Q/SO calculations to predict the vibrational and A-X transition moments. To facilitate these calculations, the predictions for the ground state dipole moment (μ_x) and the A-X transition moment ($\langle A|\mu|X\rangle$) were fitted to simple

quadratic functions of R. The resulting expressions were μ_x= -10.41+8.726R-0.283R^2 and $\langle A|\mu|X\rangle$=0.494-0.0356R-0.0595R^2 Debye. The transition energies and dipole moments are listed in Table 5.3, where the results for the A-X transition were those of the Ω=3/2 component, as the transition dipole moments for Ω=1/2 were closely similar. All of the data presented in Table 5.3 were calculated using Level 8.0[24].

5.3.2. Data Analysis

Knowledge of the rotational energy level structure of the intermediate state used in the PFI-ZEKE measurements was needed for analysis of the spectra shown in Figs. 5.3 and 5.4. Due to the perturbed nature of the BaO $A^1\Sigma^+$ state, the rotational constant for the v'=8 level is not generated reliably from the usual Dunham expansion coefficients. For analysis of the present data we have determined the effective rotational constant by fitting to the LIF band shown in Fig. 5.1. The BaO ground state constant was set to the literature value of B_0''=0.31192 cm^{-1}. Least squares fitting then yielded a band origin of 20609.3(1) and rotational constant of B_8'=0.2496(5) cm^{-1}. The latter is consistent with the deperturbed value of B_8'=0.2492 cm^{-1} reported as Fit 10 by Gottscho *et al*.[17] The small number of rotational lines seen in the spectrum, combined with the relatively low resolution, was such that the centrifugal distortion constant could not be determined. Furthermore, the perturbations for this upper state did not result in a discernable displacement of the lines from the algebraic form of the rigid rotor model.

The rotational structure of the X, v^+=0 PFI-ZEKE spectrum was analyzed using

the J' assignments derived from the two-dimensional spectroscopy measurements. As the electronic structure calculations clearly identify the ground state as being $^2\Sigma^+$, the rotational energy levels of this state were represented by the expression,

$$F(N^+) = B_0^+ N^+(N^+ + 1) \quad (1)$$

where N^+ is the integer quantum number for rotational angular momentum. Preliminary fits to the structure were carried out using the MRCI+Q/SO prediction of B_0^+=0.2674 cm^{-1}. This yielded the assignments shown in Fig 3. Optimization of the transition origin ($\nu^+_{X,0}$) and the rotational constant then yielded values of $\nu^+_{X,0}$=34335.3(20) and B_0^+=0.281(6) cm^{-1}. Note that the structure in the 34300-34320 cm^{-1} range was too congested for unambiguous assignment. The density of features suggests that there are significant contributions from the higher J' levels of the lighter isotopologues.

The transition origin for the ν^+=0 PFI-ZEKE band was reasonably well represented by the most intense central feature. The noisier spectra for the vibrationally excited levels of $X^2\Sigma^+$ were not of sufficient quality for estimation of the rotational constants. Consequently, the most intense central feature of each ν^+>0 band was used to define the band origin, with an estimated error of ±2 cm^{-1}. The band origins of the A state features were estimated using the intensity maxima of the rotational contours. Note that the lower energy spin-orbit component has been assigned as Ω=3/2, based on the theoretical predictions. Band origin data for both the X and A states are listed in Table 5.4. Vibrational constants for the X state were obtained by fitting to the expression

$$\nu^+_{el,v^+} = T^+_{el} + \omega^+_{el}\left(v^+ + \frac{1}{2}\right) - \omega_e x^+_e \left(v^+ + \frac{1}{2}\right)^2 \quad (2)$$

The vibrational anharmonicity for the A state was too small for determination using the

available data, and so the average vibrational interval was used to estimate the vibrational frequency. Constants for the X and A states are given in Table 5.5.

5.4. DISCUSSION

The IE obtained from the present measurements (6.8123(3) eV) is in good agreement with the values reported by Farber and Srivastava[13] (7(1) eV), Murad[11] (6.8(2) eV) and Koitabashi[12] (6.91 eV), and somewhat higher than the ionization onset (6.46(7) eV) measured by Dyke *et al*.[2] using photoelectron spectroscopy. The most intense region of the photoelectron spectrum corresponded to a vertical IE of 6.89(3) eV. In retrospect, it appears that this maximum reflected the adiabatic IE, and that the spectrum at lower energies was contributed by thermally excited BaO (the vapor was generated using a furnace that operated at 1900 K)[2].

The difference between the IE of BaO and that of atomic Ba (5.2117 eV)[4] indicates that the bond dissociation energy (D_0^0) decreases by 1.6006 eV on ionization. Previous determinations of D_0^0 for BaO[11,13,25], include a study that employed extrapolation of spectroscopic data to the dissociation limit[26]. The most recent studies yielded values in the range of 5.64(13)[27], 5.68(5)[25] and 5.75(15)[26] eV. Combined with the IE's for Ba and BaO, these data yield a bond dissociation energy for BaO^+ in the range of 4.04-4.15 eV, in agreement with the value of 4.1(2) eV recommended by Murad[11,28].

Previously published theoretical predictions of the IE for BaO are limited to the Hartee-Fock-Slater calculations of Dyke *et al*.[2], which yielded a value of 5.24 eV. The

higher-level electronic structure calculations reported here (cf. Table 5.2) gave somewhat better results, but the predictions were still approximately 0.3 eV below the measured value. The source of this discrepancy was not determined.

The vibronic energy level structure observed for BaO^+ clearly shows that the ion has an $X^2\Sigma^+$ ground state with a low-lying $A^2\Pi$ excited state. This is consistent with the model for the electronic structure of alkaline earth oxide ions described in the introduction. Our theoretical predictions for the ground state vibrational constants are in reasonably good agreement with the measured values, with DFT/B3LYP giving the closest approximation. However, the DFT and MRCI calculations underestimated the rotational constant, while the CCSD(T) method produced a constant that was too large.

Test calculations for the ground state of neutral BaO consistently underestimated the rotational constant, while the harmonic vibrational frequency was slightly overestimated by the *ab initio* methods. There were no obvious trends that could be used to gauge the relative merits of the various calculation methods applied to BaO^+.

For the $A^2\Pi$ state the closest agreement between the experimental and calculated properties was obtained for the all-electron MRCI+Q/SO method. The predicted vibrational frequency was within the experimental error range, and the spin-orbit interval of 185 cm^{-1} was reasonably close to the measured value of 213 cm^{-1}. The primary defect was that the excitation energy of the A state was approximately 560 cm^{-1} below the measured value. As this difference is comparable to the vibrational spacing, it was important to establish that there were no bands of the A state lying about 506 cm^{-1} below the feature assigned as the origin in Fig. 5.5. Multiple scans of this spectral region were

performed, but no additional bands were found.

The MRCI+Q/SO calculations performed using the ECP46MWB basis for Ba produced A state energies that were a little higher than those of the all-electron model, but still below the observed energies. This basis set yielded a lower vibrational frequency and a smaller spin-orbit interval of 117 cm^{-1}. Spin-free calculations for the A state were performed using the CCSD(T) and DFT/B3LYP methods. To facilitate comparison, an approximate spin-free energy was derived from the experimental data by assuming a symmetrical displacement of the Ω=3/2 and 1/2 components. This gives a spin-free energy of 1589 cm^{-1}. The CCSD(T) and DFT/B3LYP calculations yielded lower estimates of 1216 and 797 cm^{-1}, respectively.

Overall, the level of agreement between the all-electron MRCI+Q/SO calculations and the experimental data indicates that the transition moments given in Table 5.3 are of sufficient accuracy to be useful for the design of resonantly enhanced multi-photon dissociation schemes for BaO^+ characterization. The most promising transitions for the first excitation step are the A-X 1-0 and 2-0 bands. Data from the PFI-ZEKE measurements show that these bands can be excited using light at wavelengths near 5.03, 4.54, 4.01 and 3.69 μm. The present generation of high-level *ab initio* electronic structure methods are certainly good enough to narrow the search for such previously unobserved transitions, but definitive spectroscopic measurements are still required for the design of laser cooling and state manipulation experiments.

REFERENCES

(1) H. Partridge, S. R. Langhoff, and C. W. Bauschlicher, Jr., *J. Chem. Phys.* **84,** 4489 (1986).

(2) J. M. Dyke, M. Feher, B. W. J. Gravenor, and A. Morris, *J. Phys. Chem.* **91,** 4476 (1987).

(3) H. Khalil, F. Le Quere, C. Leonard, and V. Brites, *J. Phys. Chem. A* **117,** 11254 (2013).

(4) B. Roth, D. Offenberg, C. B. Zhang, and S. Schiller, *Phys. Rev. A* **78,** 042709/1 (2008).

(5) J. E. Goeders, C. R. Clark, G. Vittorini, K. Wright, C. R. Viteri, and K. R. Brown, *J. Phys. Chem. A* **117,** 9725 (2013).

(6) M. V. DePalatis and M. S. Chapman, *Phys. Rev. A At.*, **88,** 023403/1 (2013).

(7) K. Chen, S. J. Schowalter, S. Kotochigova, A. Petrov, W. G. Rellergert, S. T. Sullivan, and E. R. Hudson, *Phys. Rev. A* **83,** 030501/1 (2011).

(8) M. G. Kokish, V. Rajagopal, J. P. Marler, and B. C. Odom, *Rev. Sci. Instrum.* **85,** 086111/1 (2014).

(9) J. H. V. Nguyen, C. R. Viteri, E. G. Hohenstein, C. D. Sherrill, K. R. Brown, and B. Odom, *New J. Phys.* **13,** 063023/1 (2011).

(10) E. Murad, *J. Chem. Phys.* **75,** 4080 (1981).

(11) M. Koitabashi, *Jpn. J. Appl. Phys., Part 1* **33,** 5995 (1994).

(12) M. Farber and R. D. Srivastava, *High Temp. Sci.* **7,** 74 (1975).

(13) M. C. Heaven, B. J. Barker, and I. O. Antonov, *J. Phys. Chem. A*, Ahead of Print (2014).

(14) A. Kramida, Yu. Ralchenko, J. Reader, and NIST ASD Team (2014), *NIST Atomic Spectra Database, version 5.2,* NIST, Gaithersburg, MD (accessed 26 May 2015) available online at http://physics.nist.gov/asd.

(15) H. Salami and A. J. Ross, *J. Mol. Spectrosc.* **233,** 157 (2005).

(16) R. A. Gottscho, J. B. Koffend, and R. W. Field, *J. Mol. Spectrosc.* **82,** 310 (1980).

(17) R. A. Gottscho, P. S. Weiss, R. W. Field, and J. G. Pruett, *J. Mol. Spectrosc.* **82,** 283 (1980).

(18) H.-J. Werner, P. J. Knowles, R. Lindh, F. R. Manby, M. Schütz *et al*., *MOLPRO, version 2010.1, a package of ab initio programs,* 2010, see http://www.molpro.net.

(19) P. O. Widmark, P. Malmqvist, and B. O. Roos, *Theoretica Chimica Acta* **77,** 291 (1990).

(20) B. O. Roos, V. Veryazov, and P.-O. Widmark, *Theoretical Chemistry Accounts* **111,** 345 (2004).

(21) M. Kaupp, P. v. R. Schleyer, H. Stoll, and H. Preuss, *J. Chem. Phys.* **94,** 1360 (1991).

(22) E. R. Davidson and D. W. Silver, *Chem. Phys. Lett.* **53,** 403 (1977).

(23) LeRoy, R. J. *LEVEL 8.0: A Computer Program for Solving the Radial Schrödinger Equation for Bound and Quasibound Levels*, University of Waterloo Chemical Physics Research Report CP-663 (2007); see

http://leroy.uwaterloo.ca/programs/.

(24) M. W. Chase, Jr., C. A. Davies, J. R. Downey, Jr., D. J. Frurip, R. A. McDonald, and A. N. Syverud, *J. Phys. Chem. Ref. Data, Suppl.* **14,** 1 (1985).

(25) R. W. Field, *J. Chem. Phys.* **60,** 2400 (1974).

(26) M. Dulick, E. Murad, and R. F. Barrow, *J. Chem. Phys.* **85,** 385 (1986).

(27) E. Murad, *J. Chem. Phys.* **77,** 2057 (1982).

(28) H. Li, C. Focsa, B. Pinchemel, R. J. Le Roy, and P. F. Bernath, *J. Chem. Phys.* **113,** 3026 (2000).

TABLE 5.1. Calculated Spectroscopic Constants[a] for BaO^+

	T_e	ω_e^+	$\omega_e x_e^+$	B_e^+	α_e^+	R_e^+ / Å
			$X^2\Sigma^+$			
MRCI+Q/SO (I)[b]	0.0	555.6	1.55	0.2674	0.0013	2.097
MRCI+Q/SO (II)[c]	0.0	537.4	2.20	0.2591	0.0014	2.130
CCSD(T)	0.0	559.7	2.04	0.3059	0.0015	1.961
DFT/B3LYP	0.0	542.8	1.71	0.2648	0.0012	2.107
			$A^2\Pi$			
MRCI+Q/SO (I)[b] $\Omega = 3/2$	937.1	505.6	1.81	0.2350	0.0012	2.237
MRCI+Q/SO (I)[b] $\Omega = 1/2$	1121.8	506.0	1.80	0.2346	0.0012	2.239
MRCI+Q/SO (II)[c] $\Omega = 3/2$	1142.7	470.1	3.71	0.2273	0.0022	2.274
MRCI+Q/SO (II)[c] $\Omega = 1/2$	1259.9	466.2	2.40	0.2267	0.0014	2.278
CCSD(T)[b,d]	1215.9	514.6	1.92	0.2351	0.0012	2.237
DFT/B3LYP[c,d]	796.7	508.2	1.79	0.2330	0.0011	2.247

[a] Constants are in cm^{-1} units unless otherwise indicated

[b] Roos all-electron ANO basis sets for Ba and O

[c] Roos basis for O with the ECP46MWB basis set for Ba

[d] Spin-free calculation

TABLE 5.2. Calculated Spectroscopic Constants[a] for BaO

	ω_e	$\omega_e x_e$	B_e	α_e	R_e / Å	IE / eV
MRCI+Q	696.0	2.90	0.2979	0.0016	1.987	6.555
CCSD(T)	676.7	2.30	0.2980	0.0014	1.987	6.546
DFT/B3LYP	656.7	2.22	0.2955	0.0014	1.995	6.472
Expt.[b]	669.76	2.028	0.3126	0.0014	1.9397	6.8198

[a] Constants are in cm^{-1} units unless otherwise indicated

[b] Experimental values for the constants are from Ref. 28, with the exception of the IE, which is from the present study. For comparison with theory, the IE value given here is the energy difference between the minima of the potential energy curves.

TABLE 5.3. Transition Dipole Moments and Franck-Condon Factors for BaO^+ Energies are in cm^{-1}, transition moments in Debye (D), and the squared transition moments in D^2 units.

X, $v''=0$				
v'	ΔE	$\langle X,v'\|\mu\|X,0\rangle$	$\|\langle X,v'\|\mu\|X,0\rangle\|^2$	
1	552.7	3.47×10^{-01}	1.20×10^{-01}	
2	1103.6	-1.45×10^{-02}	2.09×10^{-04}	
3	1650.5	1.17×10^{-03}	1.37×10^{-06}	
4	2189.0	-1.81×10^{-04}	3.29×10^{-08}	
5	2726.5	-6.77×10^{-06}	4.58×10^{-11}	
A-X, $v''=0$				
v'	ΔE	$\langle A,v'\|\mu\|X,0\rangle$	$\|\langle A,v'\|\mu\|X,0\rangle\|^2$	FCF
0	910.8	4.56×10^{-02}	2.08×10^{-03}	1.12×10^{-01}
1	1411.2	-6.73×10^{-02}	4.53×10^{-03}	2.15×10^{-01}
2	1908.5	7.37×10^{-02}	5.43×10^{-03}	2.31×10^{-01}
3	2403.2	-6.88×10^{-02}	4.74×10^{-03}	1.83×10^{-01}
4	2895.4	5.82×10^{-02}	3.38×10^{-03}	1.20×10^{-01}
5	3385.0	-4.58×10^{-02}	2.10×10^{-03}	6.93×10^{-02}
6	3871.6	3.44×10^{-02}	1.18×10^{-03}	3.64×10^{-02}
7	4356.1	-2.48×10^{-02}	6.14×10^{-04}	1.78×10^{-02}
8	3838.0	1.73×10^{-02}	2.99×10^{-04}	8.21×10^{-03}
9	5317.4	-1.18×10^{-02}	1.39×10^{-04}	3.62×10^{-03}
10	5795.0	7.90×10^{-03}	6.24×10^{-05}	1.55×10^{-03}

TABLE 5.4. Band Origins and Vibrational Intervals for the Low Energy Vibronic States of BaO^+

$X^2\Sigma^+$	v^+	E[a]	ΔE[b]	
	0	54 944.6		
	1	55 488.2	543.6	
	2	56 031.9	543.8	
	3	56 562.9	531.0	
	4	57 097.9	535.0	
	5	57 628.5	530.6	
$A^2\Pi_{3/2}$	v^+	E[a]	ΔE[b]	$\Delta E(SO)$[c]
	0	56 426.4		213.7
	1	56 932.4	506.0	215.4
	2	57 438.2	505.8	213.3
$A^2\Pi_{1/2}$	v^+	E[a]	ΔE[b]	
	0	56 640.1		
	1	57 147.8	507.7	
	2	57 651.6	503.8	

[a] All energies are given in cm^{-1}, relative to BaO $X^1\Sigma^+$, v=0, J=0. The errors are ± 2 cm^{-1}.

b Intervals between successive vibrational levels.

c Intervals between spin-orbit states.

TABLE 5.5. Molecular Constants for BaO^+

All units are in cm^{-1}.

State	T_0	ω_e (cm^{-1})	$\omega_e x_e$ (cm^{-1})
$X^2\Sigma^+$	0	547.3(24)	1.8(4)
$A^2\Pi_{3/2}$	1482(2)	506(4)	…
$A^2\Pi_{1/2}$	1696(2)	506(4)	…

FIGURE 5.1.

Laser induced fluorescence spectrum of the BaO $A^1\Sigma^+ - X^1\Sigma^+$ 8–0 band. The downward-going trace is a simulation for the ^{138}BaO isotopologue with a rotational temperature of 20 K. The R-branch bandhead for ^{138}BaO is the dominant peak centered at 20 610.5 cm^{-1} . The simulation did not include the lighter isotopologues, but the positions of the R-bandheads for ^{137}BaO, ^{136}BaO, and ^{135}BaO are indicated on the observed spectrum.

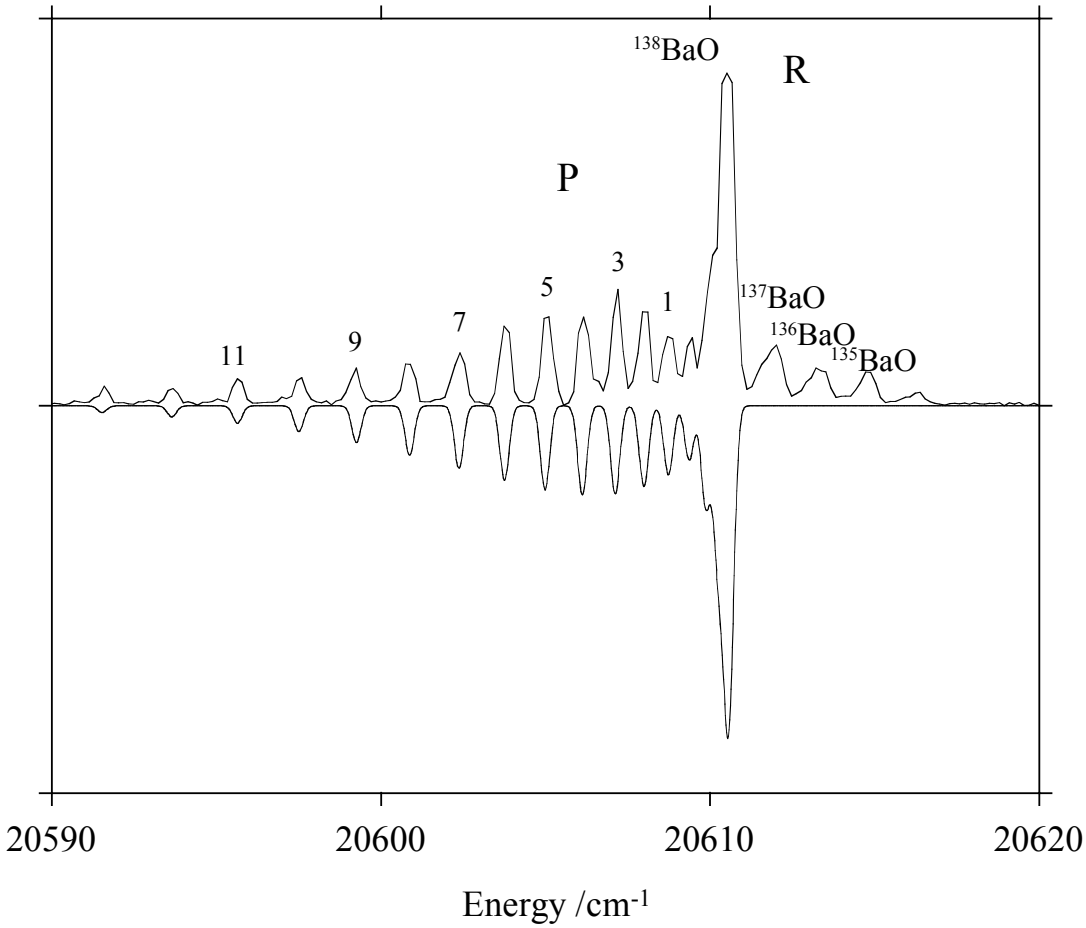

FIGURE 5.2.

A PFI-ZEKE scan of the BaO^+ $X^2\Sigma^+$, $v^+=0$ level. This trace was recorded with the first laser tuned to the ^{138}BaO A–X, 8–0 bandhead. The energy scale is that of the second photon. Peaks are labeled as N^+–J′. See text for details.

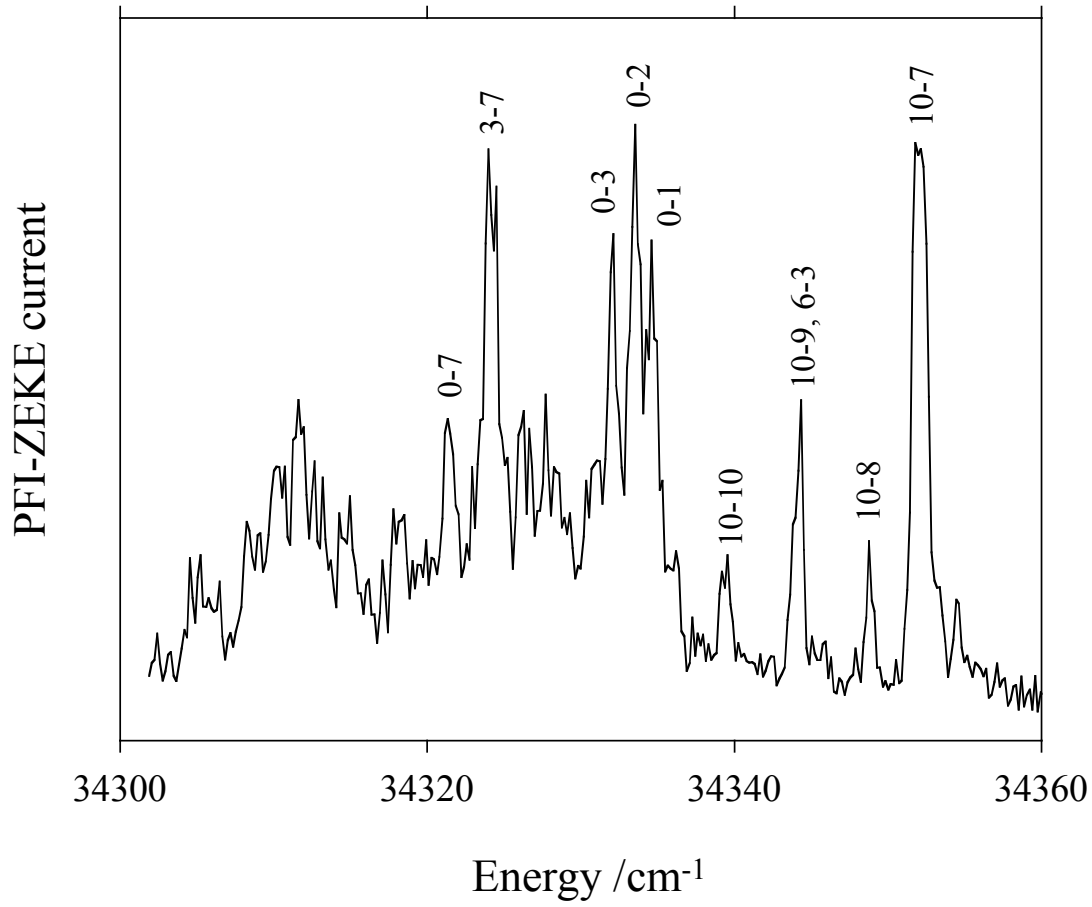

FIGURE 5.3.

Action spectra recorded by scanning the energy of the first photon while monitoring the PFI-ZEKE signal with the second laser tuned to a resonant feature. Trace *a* was recorded with the second laser tuned to the feature labeled 10–7 (34 352 cm^{-1}) in Fig. 5.2. Trace *b* was recorded with the second laser tuned to the feature labeled 10–9, 6–3 (34 344 cm^{-1}) in Fig. 5.2.

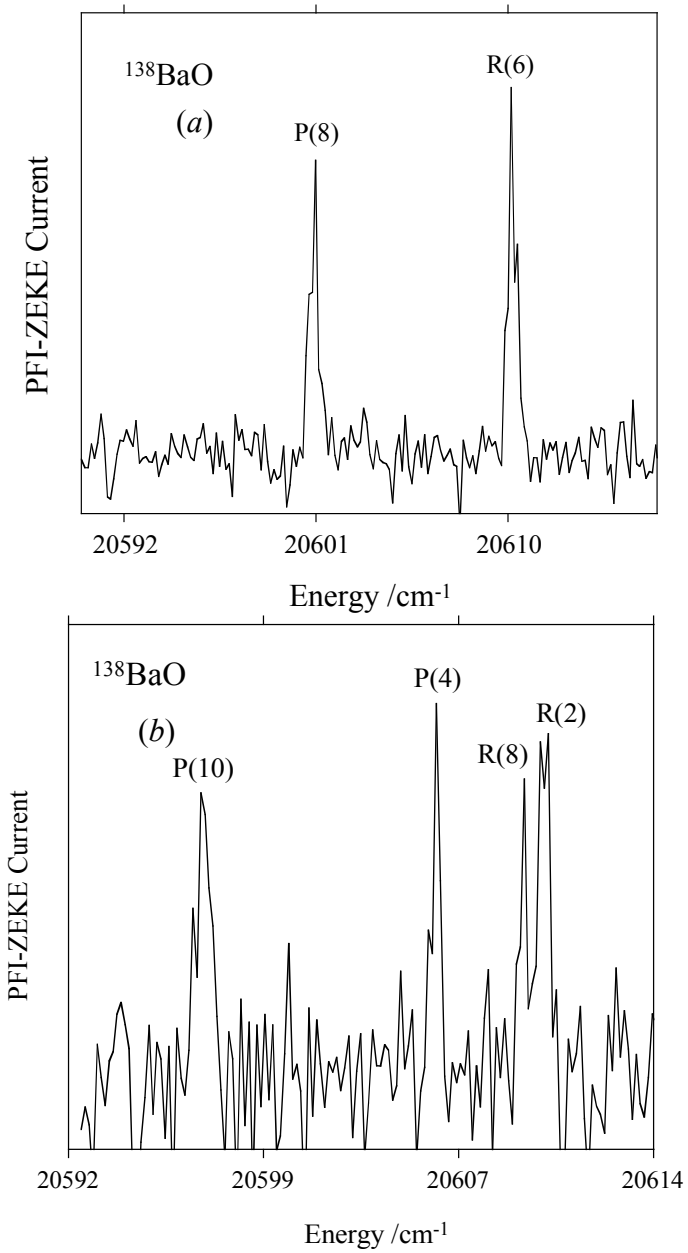

FIGURE 5.4.

PFI-ZEKE survey scan showing the low energy vibronic states of BaO^+. The energy scale is relative to the BaO^+ ground state zero-point ($v^+=0$, $N^+=0$). The atomic line marked with an asterisk is due to the presence of impurity Fe.

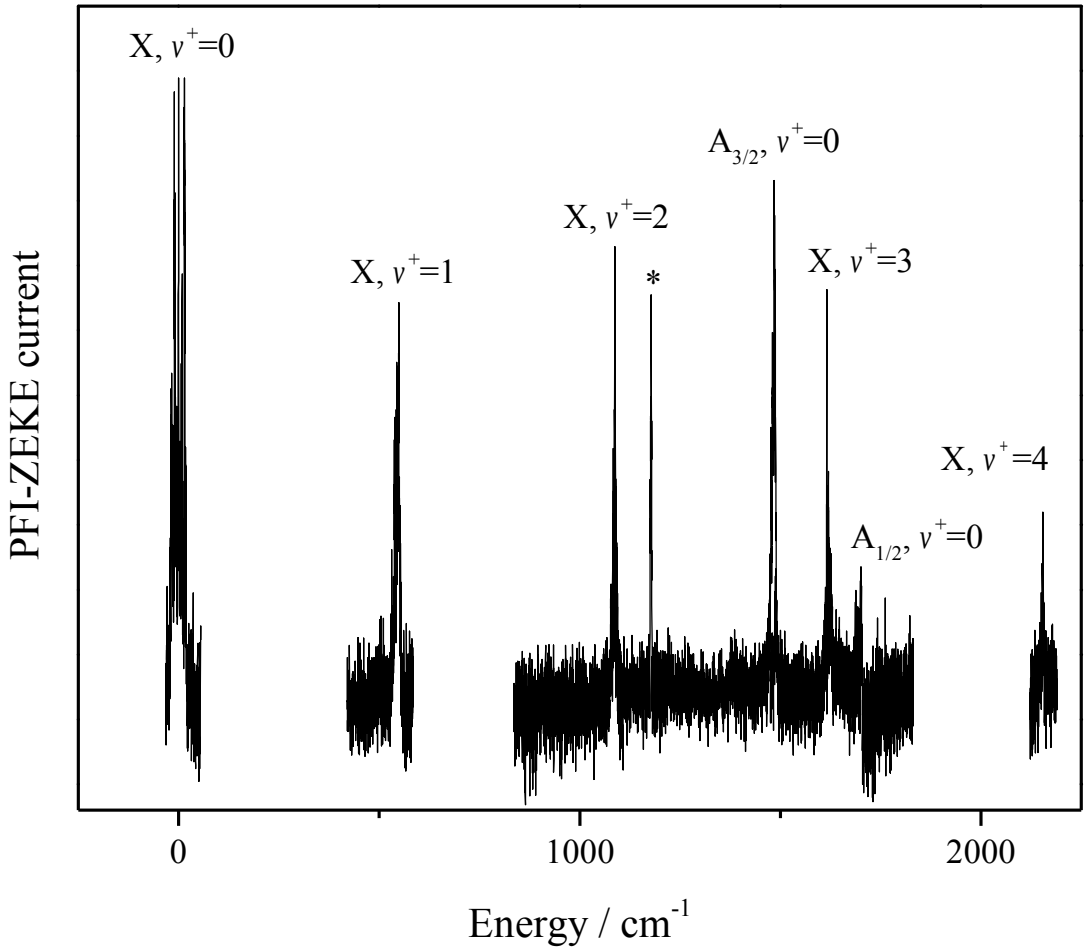

FIGURE 5.5.

PFI-ZEKE spectrum showing the rotational contour of the $A^2\Pi_{3/2}$, $v^+=0$ feature.

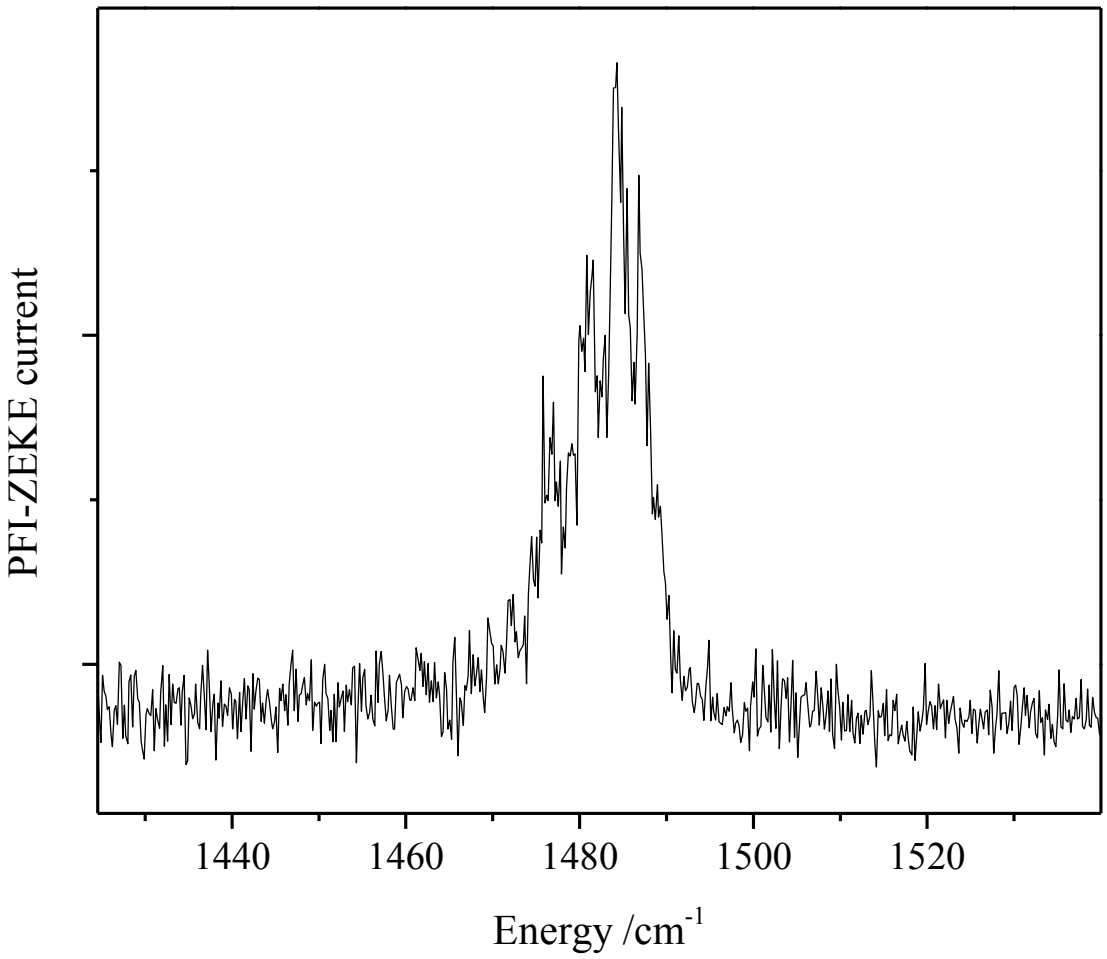

FIGURE 5.6.

Potential energy curves for the $X^2\Sigma^+$ and $A^2\Pi$ states of BaO^+. These curves were calculated using the MRCI+Q/SO method with the all-electron basis sets. The upward and downward pointing triangles are for the $A^2\Pi$ state Ω=1/2 and Ω=3/2 spin-orbit states.

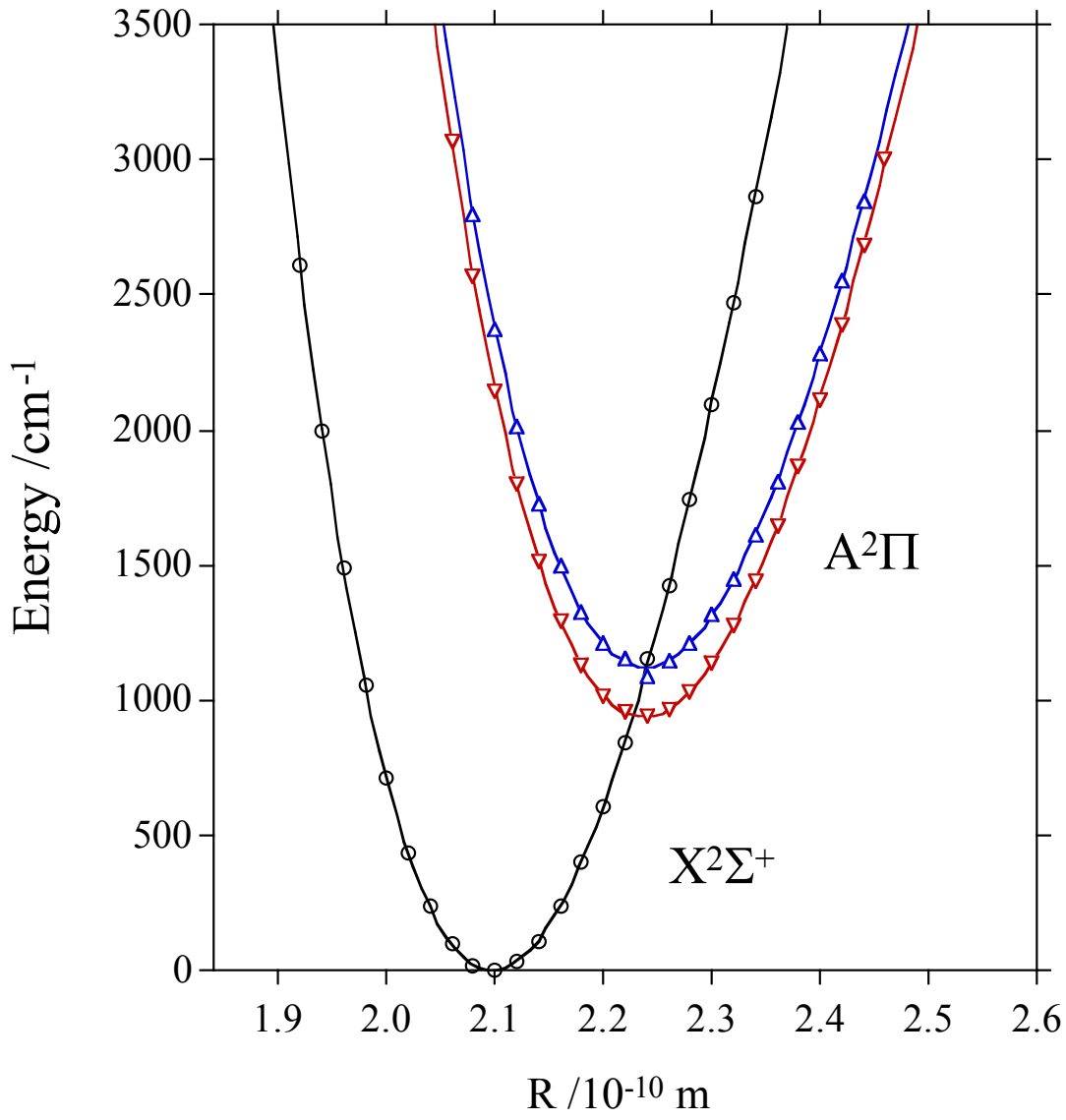

Chapter 6

Characterization of the $BaCl^+$ ($X^1\Sigma^+$) Cation by Photoelectron Spectroscopy

6.1. INTRODUCTION

Diatomic cations of the form MX^+, where M is an alkaline earth metal and X is a halogen, are of interest for studies of molecular physics and chemistry at low temperatures[1-6]. The advantage of using ions is that they can be readily trapped using external fields. The M^+ ions are well suited for laser cooling as they have transitions that are analogous to those of the alkali metals. Coulomb crystals of M^+ are readily formed in rf traps. Reactions of these atomic ions yield diatomic products that are sympathetically cooled to low translational temperatures by the surrounding atomic ions. In addition to using laser ablation as an ion source, the molecular ions BaF^+, $BaCl^+$ and BaO^+ have been generated by the reactions of laser cooled Ba^+ with SF_6, CH_3Cl, and O_2, respectively.[3,7] As discussed by Hudson,[4] the long-range repulsive forces between M^+/MX^+ pairs mediate translational cooling, but they are not effective in cooling the internal degrees of freedom. The short-range interactions between an MX^+ ion and a laser cooled neutral atom will be

far more effective in achieving ro-vibrational relaxation. This brings to light another advantage of the MX^+ species. They are closed-shell ions that can interact non-reactively with a range of neutral atoms. As an example, Hudson and co-workers have demonstrated vibrational cooling of $BaCl^+$ induced by interactions with laser-cooled Ca atoms.[1,2] This is a milestone achievement, but the study also highlights one of the current problems encountered in working with the diatomic ions of interest. There are almost no gas phase spectroscopic data for these species, and this information is essential for the characterization of internal state population distributions. To obtain the vibrational state distributions for $BaCl^+$, Hudson and co-workers[1,2] analyzed the band contours for the free-bound $^1\Pi$-$X^1\Sigma^+$ transition, which was detected by monitoring the rate of Ba^+ ion production. Ab initio electronic structure calculations were used to guide the interpretation of the photodissociation spectrum.

In the present study we have used pulsed-field ionization, zero-kinetic energy photoelectron (PFI-ZEKE) spectroscopy to observe the low-energy ($v^+ = 0$-3) of $BaCl^+$. These measurements validate the potential energy curve used to analyze the photofragmentation data of Chen et. al.[2], and provide an accurate ionization energy (IE) for BaCl. The results are also used to assess the predictive capabilities of various electronic structure calculations.

6.2. EXPERIMENTAL

The apparatus used for these measurements has been described previously[8]. BaCl was produced in the gas phase by pulsed laser vaporization of Ba in the presence of a He/Cl_2 gas mixture (0.1% Cl_2). The gas mixture was subject to supersonic expansion, in order to cool the reaction products. The reagents used consisted of natural abundance isotopic mixtures for both Ba and Cl. Isotope shifts were below the resolution of these measurements. Two-color photoionization was used to examine the low energy states of $BaCl^+$. This was accomplished using two independently tunable pulsed dye lasers (with linewidths of 0.15 and 0.3 cm^{-1}, FWHM). The first laser pulse was tuned to excite the unresolved Q-branch feature of the BaCl, $C^2\Pi_{3/2}$-$X^2\Sigma^+$, 0-0 band at 19453.0 cm^{-1}.[9] Laser induced fluorescence spectroscopy of the C-X transition was used to optimize the tuning of the first laser. Once this resonance had been established, the second laser was tuned over the wavelength range where the sum of the photon energies would span the ionization threshold. Previous studies indicated an IE of 40,000±400 cm^{-1} (see (10) and references therein). A time-of-flight mass spectrometer was used to monitor the flux of $^{138}Ba^{35}Cl^+$ ions, thereby producing a photoionization efficiency spectrum. This scan yielded a preliminary IE of 40,540±15 cm^{-1}. The IE was further refined by recording the PFI-ZEKE spectrum. For these measurements the dye lasers were used to excite BaCl to long-lived, high-n Rydberg states that lie just below the ionization threshold. This was done under field-free conditions. After a delay of 2 μs a pulsed field of 0.36 V/cm was applied to ionize the excited BaCl, and convey the electrons to a microchannel plate

detector. The absolute wavenumber calibration of the second dye laser was established by recording resonantly enhanced one-color, three-photon (1+2) ionization of U. The U atomic line positions were obtained from the NIST atomic spectra database.[11]

6.3. RESULTS AND DISCUSSION

PFI-ZEKE measurements were used to observe the $v^+ = 0 – 3$ vibrational levels of the $BaCl^+$ ground state. Fig. 6.1 shows a composite scan over these features. The PFI-ZEKE scans did not yield resolvable rotational structure. Consequently, we have used the maximum intensity points to determine the band positions, with an estimated relative uncertainty of ±1 cm^{-1}. The band energies, relative to BaCl $X^2\Sigma^+$, v=0, are listed in Table 6.1. Due to the fact that the rotational structure was not resolved, we estimate that the absolute uncertainty for the IE is ±5 cm^{-1}. Fitting the Morse vibrational energy expression,

$$G(v^+) = \omega_e\left(v^+ + \frac{1}{2}\right) - \omega_e x_e\left(v^+ + \frac{1}{2}\right)^2 \qquad (1)$$

to the band energies yielded vibrational constants of ω_e=342(2) cm^{-1} and $\omega_e x_e$=1.6(4) cm^{-1}.

Electronic structure calculations were used to predict the ground state molecular constants of BaCl and $BaCl^+$, and the IE of BaCl. These calculations were performed using the Molcas 7.8 suite of programs.[12] The triple zeta ANO-RCC-VTZP basis sets

were used for both Ba and Cl. Scalar relativistic effects were included by using the second order corrections of the Douglas-Kroll-Hess Hamiltonian. Single point energies, spaced by 0.02 Å, were calculated over the internuclear distance range from 2.3 to 3.5 Å. Vibrational constants and the equilibrium bond lengths were obtained by fitting the lower energy points ($E<5000$ cm^{-1}, relative to the potential minimum) to a Morse potential. The results from B3LYP density functional theory, CASPT2 and CCSD(T) calculations are compared with the experimental results in Table 6.2. This table also includes the results of the CASPT2 calculations reported by Chen *et al*.[2] in their study of $BaCl^+$ photodissociation. All of the methods examined gave reasonable predictions for both BaCl and $BaCl^+$ (note that Table 6.2 presents the adiabatic IE values from the calculations). Note that all of the calculations slightly underestimate the harmonic vibrational frequencies. The good agreement between the CASPT2 calculations of Chen *et al*.[2] and the experimental data provide additional evidence in support of their interpretation of the $BaCl^+$ free-bound spectrum.

The present theoretical results the IE are also respectable, indicating that the calculations correctly reproduce the increase in the bond energy that accompanies ionization. The reason for this increase in the bond energy, contraction of the bond length, and increase in the vibrational frequency is easily understood by examination of the highest occupied molecular orbitals (HOMO) of BaCl and $BaCl^+$. The singly occupied HOMO of BaCl is shown on the right hand side of Fig. 6.2. This orbital is a metal centered 6s/6p hybrid that is polarized away from the negatively charged Cl. It is somewhat anti-bonding in character. The HOMO for $BaCl^+$ is composed primarily of the

Cl 3pπ orbitals (3px is shown in Fig. 6.2). Hence, ionization of BaCl removes the 6s electron and reduces the electrostatic repulsion. This well defined ionic character also explains why the ground state properties of both BaCl and $BaCl^+$ are readily predicted using single-reference electronic structure methods.

Lastly, it is of interest to compare the vibrational constant for $BaCl^+(X)$ with the constants for the more highly excited states of BaCl. The E, F, and G states (all $^2\Sigma^+$), with term energies of 27064.8, 29493.6 and 32511.4 cm^{-1}, have harmonic vibrational frequencies of 311.5, 331.8 and 331.3 cm^{-1}.[13] This trend suggests that the vibrational constants are converging toward the value for the ion as the energy increases, as would be expected for a series of Rydberg states.

REFERENCES

(1) W.G. Rellergert, S.T. Sullivan, S.J. Schowalter, S. Kotochigova, K. Chen, E.R. Hudson, *Nature (London, U. K.),* **495,** 490-494 (2013).

(2) K. Chen, S.J. Schowalter, S. Kotochigova, A. Petrov, W.G. Rellergert, S.T. Sullivan,

E.R. Hudson, *Phys. Rev. A At., Mol., Opt. Phys.,* **83,** 030501/030501-030501/030504 (2011).

(3) M.V. DePalatis, M.S. Chapman, *Phys. Rev. A At., Mol., Opt. Phys.,* **88,** 023403/023401-023403/023407 (2013).

(4) E.R. Hudson, *Phys. Rev. A At., Mol., Opt. Phys.,* **79,** 032716/032711-032716/032719 (2009).

(5) P. Puri, S.J. Schowalter, S. Kotochigova, A. Petrov, E.R. Hudson, *J. Chem. Phys.,* **141,** 014309/014301-014309/014305 (2014).

(6) J.H.V. Nguyen, C.R. Viteri, E.G. Hohenstein, C.D. Sherrill, K.R. Brown, B. Odom, *New J. Phys.,* **13,** 063023/063021-063023/063028 (2011).

(7) J.E. Goeders, C.R. Clark, G. Vittorini, K. Wright, C.R. Viteri, K.R. Brown, *J. Phys.Chem. A,* **117,** 9725-9731 (2013).

(8) M.C. Heaven, B.J. Barker, I.O. Antonov, *J. Phys. Chem. A,* **118,** 10867-10881 (2014).

(9) P. Pages, A. Pereira, P. Royen, *Phys. Scr.,* **31,** 281-285 (1985).

(10) L.A. Kaledin, M.C. Heaven, R.W. Field, *J. Mol. Spectrosc.,* **193,** 285-292 (1999).

(11) Kramida, A., Ralchenko, Yu., Reader, J., and NIST ASD Team (2014). *NIST Atomic Spectra Database (ver. 5.2)*, (Online). Available: http://physics.nist.gov/asd (accessed 2015, July 10). NIST, Gaithersburg, MD.

(12) F. Aquilante, L. De Vico, N. Ferre, G. Ghigo, P.-a. Malmqvist, P. Neograd y, T.B. Pedersen, M. Pitonak, M. Reiher, B.O. Roos, L. Serrano-Andres, M. Urban, V. Veryazov, R. Lindh, *J. Comp. Chem.*, **31,** 224-247 (2010).

(13) K. P. Huber, G. Herzberg, *Molecular Spectra and Molecular Structure, 4: Constants of Diatomic Molecules*, 1979.

(14) P. Pages, A. Pereira, P. Royen, *Phys. Scr.,* **31,** 281-285 (1985).

TABLE 6.1. Band Energies and Vibrational Invervals for $BaCl^+ X^1\Sigma^+$

v^+	E (cm^{-1}) [a]	ΔE (cm^{-1})
0	40459.2	
1	40888.3	339.1
2	41222.3	334.0
3	41555.0	332.7

[a] The band energies are relative to $BaCl\ X^2\Sigma^+$, $v = 0$.

TABLE 6.2. Calculated and Measured Spectroscopic Constants for BaCl and $BaCl^+$

Method	ω_e (cm^{-1})	$\omega_e x_e$ (cm^{-1})	R_e (Å)	IE (cm^{-1})
$^{138}Ba^{35}Cl^+$ $X^1\Sigma^+$				
CASPT2[a]	325.3	1.56	2.57	
CASPT2	332.3	0.79	2.61	
CCSD(T)	327.9	0.82	2.61	
B3LYP/DFT	323.7	0.81	2.62	
Expt.[b]	342(2)	1.6(4)	–	
$^{138}Ba^{35}Cl$ $X^2\Sigma^+$				
CASPT2	273.3	0.90	2.72	40170
CCSD(T)	271.4	0.87	2.72	40436
B3LYP/DFT	268.5	0.89	2.72	42021
Expt.[c]	279.9	0.90	2.68	40549[b]

[a] Chen *et al.*[2]

[b] This work

[c] Pages *et al.*[9] The R_e value was calculated from the equilibrium rotational constant, $B_e = 0.0839673$ cm^{-1}.

FIGURE 6.1.

PFI–ZEKE spectra showing the vibrational levels of $BaCl^+(X^1\Sigma^+)$. The energy scale is relative to $BaCl(X^2\Sigma^+)$ v''=0. Note that the vertical scale for the v^+=3 band has been expanded by a factor of five.

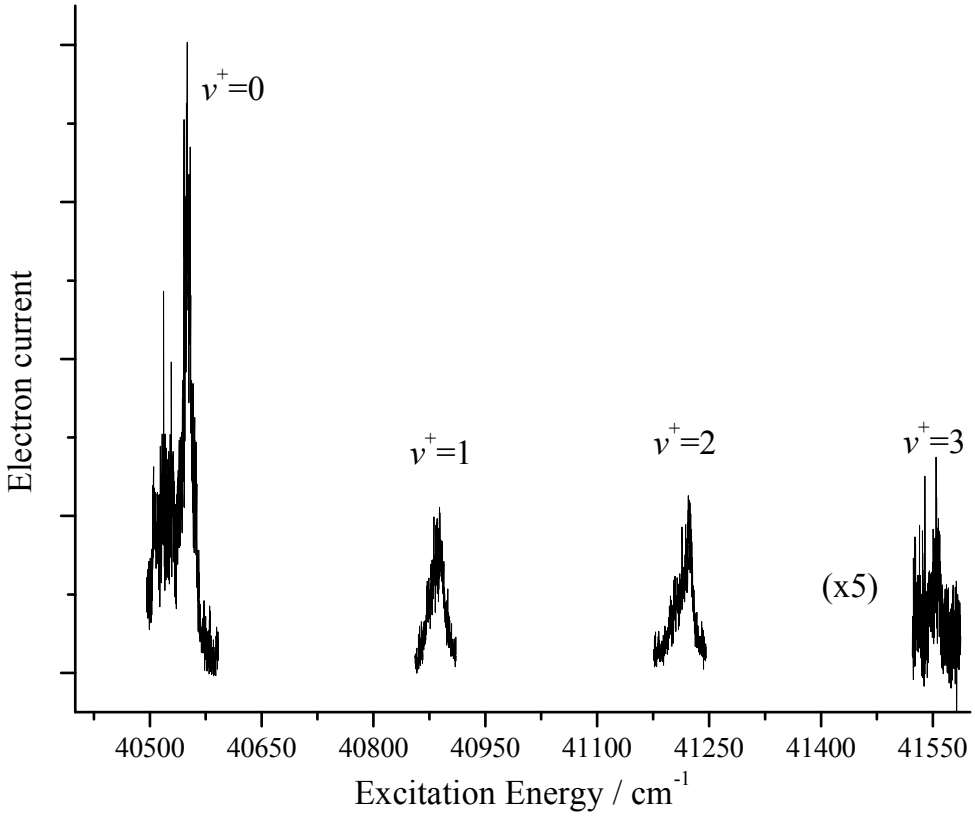

FIGURE 6.2.

The highest energy occupied molecular orbitals for BaCl (left) and $BaCl^+$ (right). These plots were generated using an isovalue of 0.02.

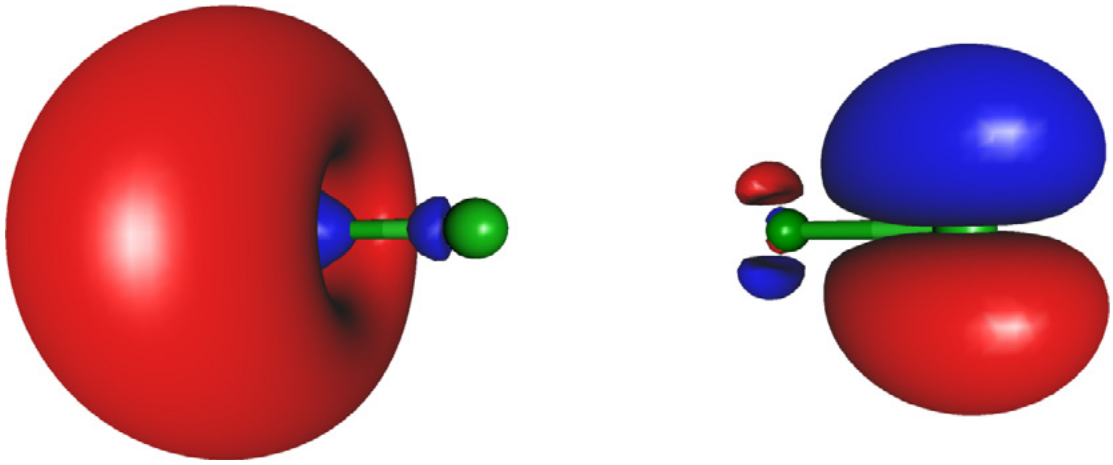

BaCl $BaCl^+$